

การศึกษาความบกพร่องในไทเทเนียมไดออกไซด์และซิงค์ออกไซด์  
โดยวิธีเฟสตัด์พรีนซิเพิล

นางสาวสุทัสนา ณ พัทลุง

วิทยานิพนธ์นี้เป็นส่วนหนึ่งของการศึกษาตามหลักสูตรปริญญาวิทยาศาสตรดุษฎีบัณฑิต  
สาขาวิชาฟิสิกส์  
มหาวิทยาลัยเทคโนโลยีสุรนารี  
ปีการศึกษา 2554

**FIRST-PRINCIPLES STUDY OF DEFECTS  
IN TiO<sub>2</sub> AND ZnO**

**Sutassana Na Phattalung**

**A Thesis Submitted in Partial Fulfillment of the Requirements for the**

**Degree of Doctor of Philosophy in Physics**

**Suranaree University of Technology**

**Academic Year 2011**

# FIRST-PRINCIPLES STUDY OF DEFECTS IN TiO<sub>2</sub> AND ZnO

Suranaree University of Technology has approved this thesis submitted in partial fulfillment of the requirements for the Degree of Doctor of Philosophy.

Thesis Examining Committee

---

(Asst. Prof. Dr. Chinorat Kobdaj)

Chairperson

---

(Prof. Dr. Sukit Limpijumnong)

Member (Thesis Advisor)

---

(Assoc. Prof. Dr. Vittaya Amornkitbamrung)

Member

---

(Prof. Dr. Kritsana Sagarik)

Member

---

(Asst. Prof. Dr. Rattikorn Yimnirun)

Member

---

(Dr. Saroj Rujirawat)

Member

---

(Dr. Michael F. Smith)

Member

---

(Prof. Dr. Sukit Limpijumnong) (Assoc. Prof. Dr. Prapun Manyum)

Vice Rector for Academic Affairs Dean of Institute of Science

สุทัศน์า ณ พัทลุง : การศึกษาความบกพร่องในไทเทเนียมไดออกไซด์ และซิงค์ออกไซด์  
โดยวิธีเฟสต์พริન્ซิเพิล (FIRST-PRINCIPLES STUDY OF DEFECTS IN TiO<sub>2</sub> AND  
ZnO) อาจารย์ที่ปรึกษา : ศาสตราจารย์ ดร. ชูกิจ ลิมปิจำนงค์, 124 หน้า.

ความบกพร่องมูลฐาน ความบกพร่องจากสารเจือ และความบกพร่องชนิดซับซ้อนที่เกิด  
จากความบกพร่องอื่นประกอบกัน มีบทบาทสำคัญต่อคุณสมบัติต่างๆ ในสารกึ่งตัวนำ เช่น สภาพ  
การนำไฟฟ้า เป็นต้น ในวิทยานิพนธ์นี้ได้ทำการศึกษาเชิงทฤษฎีโดยอาศัยการคำนวณแบบเฟสต์  
พริન્ซิเพิล ในการศึกษาความบกพร่องแบบจุด ทั้งที่เป็นความบกพร่องเดี่ยวและชนิดซับซ้อน ได้  
ศึกษาพลังงานการก่อเกิด และสมบัติของโครงสร้างอิเล็กทรอนิกส์ของความบกพร่องเหล่านั้น  
นอกจากนั้น ยังได้คำนวณลักษณะเฉพาะของการดูดกลืนแสงย่านรังสีเอกซ์ของความบกพร่องจาก  
สารเจือ ที่สามารถใช้ระบุโครงสร้างโดยรอบของความบกพร่องนั้นได้เมื่อทำการเปรียบเทียบกับผล  
ที่ได้จากการทดลอง ผลการศึกษาที่สำคัญสามารถสรุปได้ดังนี้ (1) ซัลเฟอร์ในไทเทเนียมได  
ออกไซด์: จากการศึกษาสมบัติทางพลังงานพบว่า อะตอมซัลเฟอร์ที่เกินในช่องว่างผลึก เป็นความ  
บกพร่องชนิดที่น่าจะเกิดในผลึกไทเทเนียมไดออกไซด์ ทั้งภายใต้เงื่อนไขการเติมซัลเฟอร์ในภาวะ  
ที่มีไทเทเนียมอยู่มาก และที่มีออกซิเจนอยู่มาก ซึ่งผลสอดคล้องกับผลการวิจัยสารเจือซัลเฟอร์ใน  
ไทเทเนียมไดออกไซด์ในอดีตของกลุ่ม (2) สารเจือร่วมในไทเทเนียมไดออกไซด์: ในบรรดาความ  
บกพร่องแบบซับซ้อนต่างๆ ที่อยู่ในรูปของคู่ระหว่าง การแทนที่ไอออนบวก และการแทนที่ไอออน  
ลบที่ได้ทำการศึกษา พบว่า คู่ระหว่างวาเนเดียมแทนที่ไทเทเนียมกับไนโตรเจนแทนที่ออกซิเจน  
เป็นตัวเลือกที่ดีที่สุด สำหรับประยุกต์ใช้เป็นตัวกระทำปฏิกิริยาต่อต้านแบคทีเรีย เนื่องจากความ  
บกพร่องนี้มีพลังงานที่มีเสถียรภาพ และน่าจะมีสมบัติในการเร่งปฏิกิริยาด้วยแสงประสิทธิภาพสูง  
(3) ฟลูออรีนในซิงค์ออกไซด์: ได้ศึกษาการดูดกลืนรังสีเอกซ์ของฟลูออรีนในซิงค์ออกไซด์เพื่อระบุ  
โครงสร้างโดยรอบของอะตอมฟลูออรีนในการทดลอง จากการเปรียบเทียบโครงสร้างการดูดกลืน  
แสงในย่านรังสีเอกซ์ชนิดใกล้ชิดขอบที่ได้จากการคำนวณ และจากการทดลอง ทำให้วิเคราะห์ได้ว่า  
สารตัวอย่างที่วัดนั้น ประกอบด้วยทั้งฟลูออรีนแทนที่ออกซิเจนในซิงค์ออกไซด์และสารซิงค์ได  
ฟลูออไรด์

สาขาวิชาฟิสิกส์

ปีการศึกษา 2554

ลายมือชื่อนักศึกษา \_\_\_\_\_

ลายมือชื่ออาจารย์ที่ปรึกษา \_\_\_\_\_

SUTASSANA NA PHATTALUNG : FIRST-PRINCIPLES STUDY OF  
DEFECTS IN TiO<sub>2</sub> AND ZnO. THESIS ADVISOR :  
PROF. SUKIT LIMPIJUMNONG, Ph.D. 124 PP.

FIRST-PRINCIPLES CALCULATIONS/ DEFECTS/ TITANIUM DIOXIDE/  
X-RAY ABSORPTION SPECTROSCOPY

Native defects, impurities, and their complexes play important roles in semi-conductors, affecting their properties such as conductivity. In this thesis, point defects and their complexes are theoretically studied using first-principles calculations. The formation energies and electronic properties of defects were studied. Moreover, the x-ray absorption signatures of impurity defects that are the indicative of the defect local structures are calculated for comparison with the measurements. The important findings can be summarized as follows. (1) Sulfur in TiO<sub>2</sub>: based on energetic properties, sulfur interstitial is predicted to be observed in TiO<sub>2</sub> under both Ti-rich and O-rich growth conditions. This result confirms our group's previous study. (2) Codopants in TiO<sub>2</sub>: Among various impurity complex defects in the form of cation-substitution and anion-substitution pairs studied, the vanadium - nitrogen pair (V<sub>Ti</sub>-N<sub>O</sub>) is proposed to be the best candidate to be applied for antibacterial agent. This is due to its energetic stability and its potential to give high photocatalytic activity. (3) Fluorine in ZnO: The x-ray absorption spectroscopy of fluorine in ZnO has been investigated in order to identify fluorine local structure observed in experiment. By comparing the calculated and measured x-ray absorption near edge structure (XANES), we analyzed that the sample contains both fluorine substitution for oxygen in ZnO and bulk ZnF<sub>2</sub>.

School of Physics

Student's Signature \_\_\_\_\_

Academic Year 2011

Advisor's Signature \_\_\_\_\_

## ACKNOWLEDGEMENTS

First of all, I would like to express appreciation to my thesis advisor, Prof. Dr. Sukit Limpijumnong, for his great advice, kindness, support, and fruitful instructions throughout the eight years of my M.S. and Ph.D. degree. I would like to thank Prof. Dr. Jaejun Yu for his kindness in accepting me to join his group at the Seoul National University for a year as an associate researcher. During the visit, I had an opportunity to work on part of this thesis as well as to gain additional knowledge about strongly correlated materials. I would like to thank Kim Heungsik, Kim Jiyeon, Lee Yeahlee, and all group members for their friendships during my visit. I thank the Synchrotron Light Research Institute, Thailand, for the computational resources and the office space. I am grateful to Development and Promotion of Science and technology Talents project (DPST) for the scholarship. I also appreciate Dr. Michael F. Smith for his fruitful discussions and kind supports. Importantly, without supports and warm advices from the faculty members of the School of Physics, Suranaree University of Technology, my study would not be completed. I also thank all of the members in our research group: Dr. Sirichok Jungthawan, Dr. Kanoknan Sarasamak, Dr. Jiraroj T.-Theinprasert, Dr. Adisak Boonchun, and Dr. Pakpoom Reunchan for their kind helps and friendships. Finally, without kind support from my dad, mom, grand parents, Dr. Suttinart Noothongkaew, and Dr. Worasak Sukkabot, I may not be able to accomplish the degree.

# CONTENTS

	Page
ABSTRACT IN THAI . . . . .	I
ABSTRACT IN ENGLISH . . . . .	II
ACKNOWLEDGEMENTS . . . . .	III
CONTENTS . . . . .	IV
LIST OF TABLES . . . . .	VII
LIST OF FIGURES . . . . .	VIII
LIST OF ABBREVIATIONS . . . . .	XII
<b>CHAPTER</b>	
<b>I INTRODUCTION . . . . .</b>	<b>1</b>
<b>II THEORETICAL APPROACHES . . . . .</b>	<b>5</b>
2.1 <i>Ab initio</i> Method . . . . .	5
2.1.1 Born-Oppenheimer Approximation . . . . .	6
2.1.2 Density Functional Theory . . . . .	6
2.1.3 Exchange-Correlation Energy . . . . .	11
2.1.4 Hybrid Functionals . . . . .	16
2.1.5 Plane Waves . . . . .	17
2.1.6 Pseudopotentials Method . . . . .	18
2.1.7 Brillouin Zone, k-points, and the Monkhorst-Pack Method . . . . .	22
2.1.8 Force Acting on Ions . . . . .	23
2.2 The VASP Codes . . . . .	24

## CONTENTS (Continued)

	Page
<b>III CALCULATION METHODS FOR DEFECTS IN SEMICONDUCTORS . . . . .</b>	<b>26</b>
3.1 Defect Concentration . . . . .	26
3.2 Defect Formation Energy . . . . .	27
3.3 Chemical Potential . . . . .	28
3.4 Defect Transition Level . . . . .	30
3.5 Defect Complex Binding Energy . . . . .	31
<b>IV SULFUR IMPURITIES IN ANATASE-TiO<sub>2</sub> . . . . .</b>	<b>33</b>
4.1 Introduction . . . . .	33
4.2 Computational Method and the Calculation Parameters . . . . .	34
4.3 Results and Discussions . . . . .	39
4.3.1 Formation Energies and Charge States . . . . .	39
4.3.2 Structure and Stability of the Sulfur Defects . . . . .	40
4.4 Conclusions . . . . .	54
<b>V CODOPING IN ANATASE-TiO<sub>2</sub> . . . . .</b>	<b>56</b>
5.1 Introduction . . . . .	56
5.2 Computational Method for Defects Calculations . . . . .	58
5.3 Results and Discussions . . . . .	60
5.3.1 Redox Potentials of Major Reactions on Semiconductor- solution Interface . . . . .	61
5.3.2 Monodoping in TiO <sub>2</sub> . . . . .	63
5.3.3 Passivated Codoping in TiO <sub>2</sub> . . . . .	69
5.4 Conclusions . . . . .	80

## CONTENTS (Continued)

	<b>Page</b>
<b>VI FLUORINE IMPURITIES IN ZnO . . . . .</b>	<b>82</b>
6.1 Introduction . . . . .	82
6.2 Computational Method . . . . .	85
6.2.1 Crystal Structure and Formation Energy . . . . .	85
6.2.2 X-ray Absorption Spectroscopy . . . . .	86
6.3 Results and Discussions . . . . .	87
6.3.1 Formation Energy of Fluorine in ZnO . . . . .	87
6.3.2 XANES of Fluorine in ZnO . . . . .	89
6.4 Conclusions . . . . .	92
<b>VII CONCLUSION AND FUTURE WORK . . . . .</b>	<b>94</b>
REFERENCES . . . . .	96
APPENDICES	
APPENDIX A PUBLICATIONS AND PRESENTATIONS . . . . .	111
A.1 List of Publications . . . . .	111
A.2 List of Presentations (oral) . . . . .	111
A.3 List of Presentations (poster) . . . . .	112
APPENDIX B PUBLICATION PAPER . . . . .	114
B.1 Manuscript Published in Applied Physics Letters	115
B.2 Manuscript Published in Current Applied Physics	118
CURRICULUM VITAE . . . . .	124

# LIST OF TABLES

<b>Table</b>		<b>Page</b>
4.1	Formation energy of S defects in anatase-TiO <sub>2</sub> and its corresponding transition levels $\varepsilon(q_1/q_2)$ with O-rich conditions is $\mu_S = -3.00$ eV. . . . .	35
4.2	Formation energy of S defects in anatase-TiO <sub>2</sub> and its corresponding transition levels $\varepsilon(q_1/q_2)$ with O-rich conditions is $\mu_{S[\text{orth}]} = -4.52$ eV. . . . .	35
4.3	Relaxation around S substitutes titanium (S <sub>Ti</sub> ) in anatase-TiO <sub>2</sub> . . .	47
4.4	Relaxation around S substitutes oxygen (S <sub>O</sub> ) in anatase-TiO <sub>2</sub> . . . .	50
5.1	The calculated $\Delta E_v$ , $\Delta E_c$ , $\Delta E_g$ , and binding energy ( $E^b$ ) for anatase-TiO <sub>2</sub> doped with N-codopants. . . . .	72
5.2	The calculated $\Delta E_v$ , $\Delta E_c$ , and $\Delta E_g$ for anatase-TiO <sub>2</sub> doped with V-codopants. . . . .	74
5.3	The calculated $\Delta E_v$ , $\Delta E_c$ , $\Delta E_g$ , and formation energy ( $E^f$ ) for anatase-TiO <sub>2</sub> doped with N <sub>O</sub> , V <sub>Ti</sub> , and (V <sub>Ti</sub> -N <sub>O</sub> ). . . . .	76

# LIST OF FIGURES

Figure	Page
2.1	All-electron potential and pseudopotential as well as their corresponding wavefunctions. . . . . 20
4.1	Calculated domain for equilibrium growth of TiO <sub>2</sub> :S as a function of $\mu_{\text{Ti}}$ (or $\mu_{\text{O}}$ ) and $\mu_{\text{S}}$ . . . . . 39
4.2	Atomic structures of Bulk, (SO) <sub>O</sub> , S <sub>i</sub> <sup>4+</sup> , S <sub>Ti</sub> <sup>0</sup> , S <sub>Ti</sub> <sup>2+</sup> , S <sub>O</sub> <sup>0</sup> and S <sub>O</sub> <sup>2+</sup> . . . . 40
4.3	Formation energies of S impurities as a function of the Fermi level, where chemical potential of sulfur is precipitated from SO <sub>3</sub> and TiS <sub>2</sub> under Ti-rich (left panel) and O-rich conditions (right panel), respectively. . . . . 42
4.4	Formation energies of S impurities as a function of the Fermi level, where chemical potential of sulfur is $\alpha$ -sulfur (orthorhombic), both under the Ti-rich (left panel) and O-rich conditions (right panel). . 43
4.5	Site decomposed electron density of states (DOS). For each atom center, the local partial DOS in a sphere radius $R$ (Ti: $R = 1.48 \text{ \AA}$ , O: $R = 0.74 \text{ \AA}$ and S: $R = 1.164 \text{ \AA}$ ) is calculated. . . . . 44
4.6	Site decomposed electron density of states (DOS) of defect (SO) <sub>O</sub> compared atomic orbital S plus 3 NN Ti and 2 NN O, $s$ , $p$ , and $d$ orbital. . . . . 45
4.7	Site decomposed electron density of states (DOS) of defect S <sub>i</sub> <sup>4+</sup> compared atomic orbital S plus and 4 NN O, $s$ , $p$ , and $d$ orbital. . . 46
4.8	Charge density of defect states of S <sub>i</sub> . . . . . 48

## LIST OF FIGURES (Continued)

Figure		Page
4.9	Site decomposed electron density of states (DOS). . . . .	49
4.10	Site decomposed electron density of states (DOS) of defect $S_{Ti}^0$ compared atomic orbital S plus and 6 NN O, <i>s</i> , <i>p</i> , and <i>d</i> orbital. . . . .	50
4.11	Site decomposed electron density of states (DOS) of defect $S_{Ti}^{2+}$ compared atomic orbital S plus and 6 NN O, <i>s</i> , <i>p</i> , and <i>d</i> orbital. . . . .	51
4.12	Charge density of a defect state of $S_{Ti}$ . . . . .	51
4.13	Site decomposed electron density of states (DOS). . . . .	52
4.14	Site decomposed electron density of states (DOS) of defect $S_O^0$ compared atomic orbital S plus 3 NN Ti, <i>s</i> , <i>p</i> , and <i>d</i> orbital. . . . .	53
4.15	Site decomposed electron density of states (DOS) of defect $S_O^{2+}$ compared atomic orbital S plus 3 NN Ti and 2 NN O, <i>s</i> , <i>p</i> , and <i>d</i> orbital. . . . .	53
4.16	Charge density of defect states of $S_O^0$ and $S_O^{2+}$ . . . . .	54
5.1	Potentials for redox processes occurring at anatase-TiO <sub>2</sub> surface at pH = 7. . . . .	62
5.2	Site decomposed electron density of states (DOS) of total and atom-projected DOS of bulk TiO <sub>2</sub> . For each atom center, the local partial DOS in a sphere radius <i>R</i> (Ti: <i>R</i> =1.48 Å and O: <i>R</i> =0.74 Å) is calculated. . . . .	64

## LIST OF FIGURES (Continued)

Figure		Page
5.3	Site decomposed electron density of states (DOS) for monodoped TiO <sub>2</sub> (anions) where (a) C <sub>O</sub> , (b) N <sub>O</sub> , and (c) F <sub>O</sub> in TiO <sub>2</sub> (magenta), compared with undoped TiO <sub>2</sub> (black). The shaded area refers the PDOS for impurity atoms. . . . .	66
5.4	Site decomposed electron density of states (DOS) for monodoped TiO <sub>2</sub> by group-VI elements (cations). . . . .	67
5.5	Site decomposed electron density of states (DOS) for monodoped TiO <sub>2</sub> by group-V elements (cations). . . . .	68
5.6	Site decomposed electron density of states (DOS) for monodoped TiO <sub>2</sub> by group-III elements (cations). . . . .	69
5.7	Site decomposed electron density of states (DOS) for Co <sub>Ti</sub> compared with undoped TiO <sub>2</sub> (black). . . . .	70
5.8	Atomic structure of codopants in TiO <sub>2</sub> by cation-cation, cation-anion, and anion-anion. . . . .	71
5.9	Site decomposed electron density of states (DOS) of N-codopants. . . . .	73
5.10	Site decomposed electron density of states (DOS) of V-codopants. . . . .	74
5.11	Site decomposed electron density of states (DOS) of Nb-codopants. . . . .	76
5.12	Site decomposed electron density of states (DOS) of V <sub>Ti</sub> , N <sub>O</sub> , (V <sub>Ti</sub> -N <sub>O</sub> ) in TiO <sub>2</sub> , compared with undoped TiO <sub>2</sub> . . . . .	77
5.13	Site decomposed electron density of states (DOS) by HSE06 of V <sub>Ti</sub> , N <sub>O</sub> , and (V <sub>Ti</sub> -N <sub>O</sub> ) in TiO <sub>2</sub> , compared with undoped TiO <sub>2</sub> . . . . .	78

## LIST OF FIGURES (Continued)

Figure		Page
5.14	Formation energies and binding energies of $V_{\text{Ti}}$ , $N_{\text{O}}$ , $(V_{\text{Ti}}-N_{\text{O}})$ codopants, and its isolated form in $\text{TiO}_2$ as a function of the Fermi level, under the Ti-rich and O-rich conditions, respectively. . . . .	79
6.1	X-ray absorption spectrum for FeO. . . . .	84
6.2	The calculated formation energies of native defects and F impurities in wurtzite ZnO as a function of Fermi level calculated under Zn-rich and O-rich conditions, respectively. . . . .	90
6.3	The local structure of F atoms in $F_{\text{O}}^+$ , $(F_{\text{i(oct)}}-F_{\text{O}})^0$ , $(F_{\text{Zn}}-F_{\text{O}})^{2-}$ , and $\text{ZnF}_2$ in wurtzite ZnO. . . . .	91
6.4	Comparison between the measured F $K$ -edge XANES spectra (taken from SNU) and the calculated F $K$ -edge XANES spectra obtained from FEFF. . . . .	92
6.5	The measured (taken from SNU) and the simulated F $K$ -edge XANES spectra of combination of $F_{\text{O}}$ and $\text{ZnF}_2$ with various ratios in ZnO. . . . .	93

## LIST OF ABBREVIATIONS

BZ	Brillouin Zone
CBM	Conduction Band Minimum
DFT	Density Functional Theory
EXAFS	Extended X-ray Absorption Fine Structure
FMS	Full-Multiple Scattering
GGA	Generalized Gradient Approximation
KS	Kohn-Sham
LAPW	Linearized Augmented Plane-Waves
LDA	Local Density Approximation
MS	Multiple Scattering
NN	Nearest Neighbor
PAW	Projector Augmented-Wave Method
PW	Plane Wave
QMC	Quantum Monte Carlo
SCF	Self-Consistent Field
USPP	Ultra Soft Pseudo Potential
VASP	Vienna <i>ab initio</i> Simulation Package
VBM	Valence Band Maximum
XANES	X-ray Absorption Near Edge Structure
XAS	X-ray Absorption Spectroscopy
XC	Exchange-Correlation

# CHAPTER I

## INTRODUCTION

Semiconductors are abundantly used in new generation electronic and optoelectronic devices because their electrical and optical properties can be precisely controlled. This is in contrast to metals and insulators, the conductivity of which cannot be easily modified. The traditional way to modify electronic properties is to introduce electrical carriers through dopants. For many purposes, one would like to introduce dopants that do not seriously disrupt the crystal's periodicity. In this way, the material's electronic structure is maintained, except for the provision of the carrier. However, in many cases, impurities and defects cause localized states to appear in the band gap. These states can greatly affect the properties of semiconductors. The effects can be undesirable or, in certain cases, can enhance functionality of the material. Either way, it is important to understand how these defect states can be predicted and controlled.

Point defects in semiconductors including native defects (such as vacancies, interstitials, and antisites) and impurities (interstitials and substitutionals) have been investigated widely because they play important roles in semiconductor properties. To fabricate high quality materials, it is necessary to suppress unintentional (often, electrically active) defects, both native defects and impurities, while maintaining the desired defects. The formation energies of defects in different growth conditions can greatly help in guiding experimentalists to choose the suitable conditions to form the desired defect. Because some defects can bind to other defects forming defect complexes, it is important to identify and explore potential defect

complexes as well.

Because the electronic properties of semiconductors are sensitive to the detailed defect structures, the precise local structure of each defect must be known before its likely effect on electrical properties can be identified. To do this, first-principles approaches capable of determining the fully-optimized local structure must be employed. First-principles calculations based on density functional theory (DFT) are powerful and this approach is extensively used for studying electrons in materials. In the calculations, many-electron problems are reduced into a single particle problem. The complicated electron-electron interactions in many-body problems are replaced by the interactions between each electron and the electron density of the system through the so-called the exchange- and correlation function (XC). By solving the Schrödinger-like single-electron equations called Kohn-Sham (KS) equations (Hohenberg and Kohn, 1964; Kohn and Sham, 1965; Hedin and Lundquist, 1971), the ground state properties of the many-electron system can be obtained. Various XC functions and the ways to solve the KS equations (Ceperley and Alder, 1980; Perdew and Zunger, 1981) have been introduced. The most commonly used XC functions are the local density approximations (LDA) (Hohenberg and Kohn, 1964; Kohn and Sham, 1965; Hedin and Lundquist, 1971) and the generalized gradient approximations (GGA) (Perdew and Wang, 1986; Perdew et al., 1996). However, it is well known that both LDA and GGA are not suitable for strongly correlated materials, such as transition metals and rare-earth elements that have well-localized  $d$ - and  $f$ -states. This leads to a severe underestimation of the calculated band gap. An orbital-dependent correction so-called LDA+ $U$  method (Anisimov et al., 1991; Liechtenstein et al., 1995) that compensates for the insufficient description of strong electronic correlations in localized  $d$ - or  $f$ -shells, is introduced. The correction has been shown to significantly improve

the results in some semiconductors such as ZnO. However, the approach introduces unrealistic shifts on the targeted bands ( $d$ - or  $f$ -state) and causes further problems in the description of the overall band structure. Recently, the hybrid functional (Heyd et al., 2006) was introduced to overcome the band gap error. In this approach, the exchange potentials are created by mixing LDA or GGA (local or semi-local) exchange potentials with Hartree-Fock (non-local) exchange potentials, while the correlation potentials are still described by LDA or GGA. The calculated band gaps, obtained from the hybrid functional calculation, are generally in good agreement with experimental band gaps. However, it requires much more computational resources than traditional LDA or GGA. Each type of XC function has its own advantages when applied for specific systems. Regarding the ion-electron interaction, many computational techniques, including what we employed here, replace the real atomic potentials with pseudopotentials, leading to much smoother electron wave functions. The smooth wave functions can be easily expanded using a small number of plane waves without losing too much accuracy; greatly reducing computational demand.

To identify impurity defects in crystals, X-ray absorption spectroscopy (XAS) measurement combining with first-principles calculations is known to be a powerful technique. The first-principles calculations play an especially important role in studies of the near edge region of the XAS, called X-ray absorption near edge spectroscopy (XANES), because the local structure cannot be easily interpreted from the data alone. Because each (impurity) element has its specific core-level energy, different elements can be selectively probed by selecting the appropriate energy range of the incident X-ray. The absorption spectrum reflects the excitations of the core electrons to empty states above the Fermi energy. Because the density of these empty states depends strongly on the local structure

around the absorbing atom, the XAS spectrum contains information about the local structure.

In this thesis, XAS measurements will be analyzed with the benefit of complementary first-principles calculations in order to identify the local structure surrounding defects in technologically-important semiconductors. It is organized as follows. Chapter II briefly describes the density functional theory and some other theoretical methods. Chapter III gives a more specific explanation about the calculation methods used for studying defects and pairs in semiconductors. Chapter IV is dedicated to sulfur defects in  $\text{TiO}_2$ . Based on energetic results, sulfur interstitial is predicted to be favored in both Ti-rich and O-rich growth conditions. Chapter V focuses on the defect pairs in  $\text{TiO}_2$ . Potential cation substitution and anion substitution pairs are investigated in order to narrow the band gap of  $\text{TiO}_2$  to reach high photocatalytic activity for using as antibacterial agent. In chapter VI, the local structure of fluorine in  $\text{ZnO}$  is investigated by a combination of X-ray absorption spectroscopy and first-principles study. The samples are predicted to contain fluorine substitution for oxygen and bulk  $\text{ZnF}_2$ . Chapter VII gives conclusions and discusses directions for future study.

# CHAPTER II

## THEORETICAL APPROACHES

Theoretical schemes to calculate ground-state properties of electrons in materials have been greatly improved in recent years and several new approximations have been developed. In this thesis, density functional theory (DFT) with local density approximation (LDA), LDA+ $U$ , or a hybrid functional have been used. In this chapter, some of the theoretical approaches and notation used in this thesis will be briefly described.

### 2.1 *Ab initio* Method

*Ab initio* or first- principles methods are those that do not need experimental parameters as inputs. In *ab initio* computational studies of materials, the only required starting parameters are those that reflect a fundamental knowledge of the atomic elements in the system, i.e. the number and identity of atomic nuclei and the number of electrons in the system. The computations involve various approximations used to solve the time-independent Schrödinger equation

$$\hat{H}\Psi(\mathbf{R}, \mathbf{r}) = E\Psi(\mathbf{R}, \mathbf{r}), \quad (2.1)$$

where  $\Psi$  is an electron wave function,  $E$  is an eigenvalue of energy,  $\mathbf{R}$  and  $\mathbf{r}$  represent the positions of the nuclei and electrons, respectively. The Hamiltonian,

containing kinetic and potential terms, can be written as

$$\hat{H} = \hat{T}_n(\mathbf{R}) + \hat{T}_e(\mathbf{r}) + \hat{V}_{nn}(\mathbf{R}) + \hat{V}_{ee}(\mathbf{r}) + \hat{V}_{ne}(\mathbf{R}, \mathbf{r}). \quad (2.2)$$

This Hamiltonian is very complicated and constitutes a many-body problem, rendering it unsolvable. However, by applying a number of approximations one can reduce the problem to a solvable one.

### 2.1.1 Born-Oppenheimer Approximation

The Schrödinger equation of a material can be first simplified by separating electron motions from nuclear motions. Since the electron mass is much smaller than that of the nuclei, it can be assumed that the nuclei remain stationary during the time scale of electronic motion. It is, therefore, reasonable to separate the electronic motion from the nuclear motion. This assumption is known as the adiabatic approximation of Born and Oppenheimer or the Born-Oppenheimer approximation (Born and Oppenheimer, 1927). Even with the Born-Oppenheimer approximation assumed, the Schrödinger equation is still enormously complicated. In order to further reduce the problem, a number of approximations were proposed. Density functional theory (DFT) is one of the ways to simplify the problem. In DFT, an electron interacts with other electrons through the electron density which has three degrees of freedom, instead of the electron wave functions which has  $3N$  degrees of freedom.

### 2.1.2 Density Functional Theory

The hypothesis that inspires the development of DFT was introduced independently by Thomas (1927) and Fermi (1928) at almost the same time. It

assumed that the kinetic energy can be written as a functional of the density of electrons  $n(\mathbf{r})$ . The kinetic energy functional is given by

$$T_{TF}[n] = \frac{3}{10}(3\pi^2)^{2/3} \int d\mathbf{r} n^{5/3}(\mathbf{r}). \quad (2.3)$$

This equation is the origin of the local density approximation (LDA). Accordingly, the Thomas-Fermi energy can be written as

$$E_{TF}[n] = T_{TF}[n] - Z \int d\mathbf{r} \frac{n(\mathbf{r})}{|\mathbf{R} - \mathbf{r}|} + \frac{1}{2} \int d\mathbf{r} d\mathbf{r}' \frac{n(\mathbf{r})n(\mathbf{r}')}{|\mathbf{r} - \mathbf{r}'|}, \quad (2.4)$$

where  $Z$  is the nuclear charge.

Subsequently, since its introduction, DFT has been extensively used for quantum mechanically study of electrons in materials.

### 2.1.2.1 Hohenberg-Kohn Theorems

In 1964, Hohenberg and Kohn, henceforth, HK, (Hohenberg and Kohn, 1964) investigated an electron gas in a time-independent external potential based on the foundation of the Thomas-Fermi theory. According to the idea they proposed, all ground state properties, such as the total energy of inhomogeneous interacting electrons, can be described by minimizing the total energy as a functional of electron density,  $n(\mathbf{r})$ , i.e. by minimizing:

$$E[n] = T[n] + \int d\mathbf{r} n(\mathbf{r}) V_{ext}(\mathbf{r}) + \int d\mathbf{r} n(\mathbf{r}) \int d\mathbf{r}' \frac{n(\mathbf{r}')}{|\mathbf{r} - \mathbf{r}'|} + E_{xc}[n], \quad (2.5)$$

where  $V_{ext}(\mathbf{r})$  is the external potential acting on the electrons. The third term on the right hand side describes the Coulomb interaction energy between electrons

and is called Hartree energy. The term is a function of charge distribution  $n(\mathbf{r})$ . The last term  $E_{xc}$  which is the exchange-correlation energy will be discussed in more detail in Sec. 2.1.3.

HK developed two important theorems (Hohenberg and Kohn, 1964; Kohn, 1999).

I). The ground-state density  $n(\mathbf{r})$  of a bound system of interacting electrons in some external potential  $V_{ext}(\mathbf{r})$  determines this potential uniquely.

II). A universal functional for the energy  $E[n]$  can be defined in terms of the density. The exact ground state is the global minimum value of this functional.

The total ground state energy is obtained from the variation principle by minimizing the energy with respect to the electron wavefunction. It can be written as

$$E_0 = E[n_0] = \langle \Psi[n_0] | \hat{T} + \hat{V} + \hat{W} | \Psi[n_0] \rangle \leq \langle \Psi[n] | \hat{T} + \hat{V} + \hat{W} | \Psi[n] \rangle = E[n]. \quad (2.6)$$

For  $n \neq n_0$ ,

$$E_0 = \min_{n \in N} E[n] = \min_{n \in N} \left[ \int d\mathbf{r} n(\mathbf{r}) V_{ext}[\mathbf{r}] + F_{HK}[n] \right], \quad (2.7)$$

where  $\hat{T}$  is the electron kinetic energy operator,  $\hat{V}$  is the electron-electron interaction operator,  $\hat{W}$  is the electron-ion interaction operator, and  $F_{HK}[n]$  is the universal functional which is valid for any number of particles under any external potential.

These theorems give a way to find the ground state electron density and energy. Note that, based on these theorems, the problem of finding the ground state energy and density is reduced to a simpler three-dimension variational

principle problem. However, an explicit expression of the ground state energy functional  $E_0[n]$  is unknown as will be described next.

### 2.1.2.2 Kohn-Sham Equation

Kohn and Sham (1965) proposed a way to determine the kinetic energy more accurately than the Thomas-Fermi approach through an exchange-correlation energy functional ( $E_{XC}$ ). The functional  $E_{XC}$  describes the quantum interaction between electrons. This simplified the overall task to finding a good approximation to the energy functional. According to Kohn and Sham, the energy functional can be written as

$$E[n] = T_0[n] + \int d\mathbf{r} n(\mathbf{r}) \left\{ V_{ext}(\mathbf{r}) + \frac{1}{2}\Phi(\mathbf{r}) \right\} + E_{xc}[n], \quad (2.8)$$

where  $T_0$  is non-interacting kinetic energy (not equal to the true kinetic energy of the interacting system),  $\Phi$  is the classical Coulomb potential for electrons, and  $E_{xc}$  is the exchange-correlation energy.  $E_{XC}$  is the functional which includes everything that is unknown, i.e., the non-classical effects of self-interaction correction, exchange and correlation as well as a portion belonging to many-body interaction in the kinetic energy.

This allows one to solve the problem of minimizing the ground state energy functional using a set of Schrödinger-like single-electron equations known as Kohn-Sham equations. This is a simpler way to obtain approximate values of the ground state energy and electron density of a many-electron system. In practice, this can be done by computing the ground state energy of a set of independent electrons in an effective potential, where the sum of the single-electron ground state energies is assumed to be the actual ground state total energy. The self-consistent Kohn-

Sham equations can be written as

$$\left[ -\frac{\hbar^2 \nabla^2}{2m} + V_{eff}(\mathbf{r}) \right] \varphi_i(\mathbf{r}) = \varepsilon_i \varphi_i(\mathbf{r}), \quad (2.9)$$

and

$$n(\mathbf{r}) = \sum_{i=1}^N |\varphi_i(\mathbf{r})|^2, \quad (2.10)$$

where  $V_{eff}(\mathbf{r})$  represents an effective single-electron potential which is a functional of electron density. It can be written as

$$V_{eff}(\mathbf{r}) = V_{ext}(\mathbf{r}) + \int d\mathbf{r}' \frac{n(\mathbf{r}')}{|\mathbf{r} - \mathbf{r}'|} + V_{xc}(\mathbf{r}), \quad (2.11)$$

where the exchange-correlation potential,  $V_{xc}(\mathbf{r})$ , is determined by the derivative of the exchange-correlation energy,  $E_{xc}[n(\mathbf{r})]$ , as follows

$$V_{xc}(\mathbf{r}) = \frac{\delta E_{xc}[n(\mathbf{r})]}{\delta n(\mathbf{r})}. \quad (2.12)$$

By solving Eqn. (2.9), the solution of the *many-body* ground state is reduced to the solution of the ground state density distribution given by a *single – particle* Schrödinger equation. The effective potential in Eqn. (2.11) includes all interaction effects: the Hartree potential (the Coulomb potential based on the charge distribution assuming electrons are immobile), the exchange potential (the potential due to electrons with the same spin as described by Pauli exclusion principle), and the correlation potential (the potential due to the effect of a given electron on the overall charge distribution).

In principle, Kohn-Sham's approach is exact. The approximation only arises after an explicit form of the unknown functional for the  $E_{xc}$  and the cor-

responding potential,  $V_{xc}$ , are assumed. Finding better approximations to these two terms are the goal of modern density functional theory (Koch and Holthausen, 2001).

### 2.1.3 Exchange-Correlation Energy

The exchange-correlation energy ( $E_{xc}$ ) is the energy difference between the kinetic energy of the interacting- and noninteracting-electron systems. The term also contains all non-classical electron interactions, i.e., the Pauli exchange which forbids two electrons the same spin at the same position and electron correlation.

From Eqn. (2.2) the electron-electron interaction is a two-body operator. Its expectation value is given by

$$\langle \Psi | \hat{V}_{ee} | \Psi \rangle = \frac{1}{2} \int \int d\mathbf{r}' d\mathbf{r} \frac{P(\mathbf{r}, \mathbf{r}')}{|\mathbf{r} - \mathbf{r}'|}, \quad (2.13)$$

where  $\Psi$  is the normalized-antisymmetric ground state electron wavefunction. The pair-density,  $P(\mathbf{r}, \mathbf{r}')$ , is the probability of simultaneously finding an electron at the point  $\mathbf{r}$  within volume element  $d\mathbf{r}$ , and another electron at  $\mathbf{r}'$  in volume element  $d\mathbf{r}'$ . It is given by

$$P(\mathbf{r}, \mathbf{r}') = n(\mathbf{r})n(\mathbf{r}') + n(\mathbf{r})n_{xc}(\mathbf{r}, \mathbf{r}'), \quad (2.14)$$

where the first term on the right hand side is the classical term. By substituting just the first term into Eqn. (2.13), the classical Coulomb repulsion or Hartree energy can be realized. The second term includes the exchange-correlation hole density,  $n_{xc}(\mathbf{r}, \mathbf{r}')$ , surrounding each electron located at position  $\mathbf{r}$ . This term arises from the fact that all electrons (1) obey Fermi statistics that kept them apart quantum-mechanically according to the Pauli-exclusion principle and (2) interact

through other non-classical Coulomb interactions. By adding these exchange and correlation terms, each electron creates a depletion, or hole, of electron density around itself.

The exchange correlation energy can be written as

$$E_{xc}[n(\mathbf{r})] = \frac{1}{2} \int d\mathbf{r} n(\mathbf{r}) \int d\mathbf{r}' \frac{n_{xc}(\mathbf{r}, \mathbf{r}')}{|\mathbf{r} - \mathbf{r}'|}. \quad (2.15)$$

The electron many-body problem would be solved if  $n_{xc}(\mathbf{r}, \mathbf{r}')$  is known exactly in the analytic form.

The exchange correlation energy can also be written in the following general form as

$$E_{xc}[n(\mathbf{r})] = \int d\mathbf{r} \varepsilon_{xc}[n(\mathbf{r})] n(\mathbf{r}), \quad (2.16)$$

where  $\varepsilon_{xc}[n(\mathbf{r})]$  is the exchange-correlation energy per particle (or energy density). This functional can be characterized by the way in which the density surrounding each electron is sampled in order to construct  $\varepsilon_{xc}[n(\mathbf{r})]$ . Next, the most widely used approximations of the exchange and correlation energy will be described.

### 2.1.3.1 Local Density Approximation

The local density approximation (LDA) is the simplest and the most often-employed approximation to calculate the exchange-correlation energy. It was proposed by Hohenberg and Kohn in their original DFT paper (Hohenberg and Kohn, 1964). In the LDA, the true exchange-correlation energy of a system is approximated by the exchange-correlation energy associated with a homogeneous electron gas of the same density. The homogeneous electron gas is the only system that the form of the exchange-correlation energy is exactly known. As a result, the

exchange-correlation term under LDA depends only on the local density. The non-spin polarized LDA exchange energy can be written as

$$E_{xc}^{LDA}[n(\mathbf{r})] = \int d\mathbf{r} \varepsilon_{xc}^{LDA}[n(\mathbf{r})]n(\mathbf{r}), \quad (2.17)$$

where  $\varepsilon_{xc}^{LDA}[n(\mathbf{r})]$  is the exchange-correlation energy per particle of a uniform electron gas of density  $n(\mathbf{r})$ . LDA works rather well for the cases where the electronic density is a smooth function in space, allowing any region in space to be locally as approximated by a homogeneous electron gas of density  $n(\mathbf{r})$ .

The exchange-correlation energy ( $\varepsilon_{xc}$ ) is actually a sum between an exchange energy ( $\varepsilon_x$ ) and a correlation energy ( $\varepsilon_c$ ). The exchange part (for the homogeneous electron gas), in atomic unit, is analytically derived by Dirac (1930) to be

$$\varepsilon_{xc}^{LDA}(n) = -\frac{3}{4} \left( \frac{9}{4\pi_2} \right)^{\frac{1}{3}} \frac{1}{r_s}, \quad (2.18)$$

where  $r_s$  is the radius of a sphere containing a total charge of one electron and given by  $\frac{4\pi}{3}r_s^3 = n(\mathbf{r})^{-1}$ . The correlation part is more complicated and was first approximated by Wigner (1938) to be

$$\varepsilon_c^{LDA}(n) = -\frac{0.44}{r_s + 7.8}. \quad (2.19)$$

Subsequently, perturbation theory (Barth and Hedin, 1972) and Quantum Monte Carlo (QMC) calculations for electron liquid (Ceperley and Alder, 1980) were used to improve the approximation of  $\varepsilon_c^{LDA}(n)$ . Later on, expressions for  $\varepsilon_c^{LDA}(n)$  that were widely-used were obtained via parameterizations (Vosko et al., 1980; Perdew and Zunger, 1981; Perdew and Wang, 1993).

In principle, LDA should work well only for the systems with slowly varying electron density. However, it works rather well even for the systems where electron density is rapidly varying such as the cases of atoms and molecules.

The most serious disadvantage of LDA is that each electron also interacts with itself, the so-called self-interaction. This is because the potential seen by a certain electron includes the potential produced by the electron itself. This is believed to be the main reason why the LDA severely underestimates the band gap of many systems (Perdew and Levy, 1983; Sham and Schluter, 1983; Perdew, 1985).

Typically, LDA *ab-initio* lattice parameters are underestimated, whereas cohesive energies, elastic moduli, and phonon frequencies are normally overestimated.

### 2.1.3.2 Generalized Gradient Approximation

The generalized gradient approximation (GGA) (Perdew and Wang, 1986; Perdew et al., 1996) was introduced in the hope of improving the exchange-correlation term for the systems with inhomogeneous electron densities. GGA allows the functional to depend not only on the local electron density but also on its local gradient value (Ortiz and Ballone, 1991). The non-spin polarized GGA exchange-correlation energy functional can be written as (Kohn, 1999)

$$E_{xc}^{GGA}[n(\mathbf{r})] = \int d\mathbf{r} f[n(\mathbf{r}), |\nabla n(\mathbf{r})|] n(\mathbf{r}), \quad (2.20)$$

where  $f[n(\mathbf{r}), |\nabla n(\mathbf{r})|]$  is a function of both the electron density and the gradient of the density. Various choices of the function  $f[n(\mathbf{r}), |\nabla n(\mathbf{r})|]$  were developed, leading to different variants of functionals under the common name of GGA. The

GGA functional which is popularly used in solid state physics is PBE, denoting the functional introduced by Perdew et al. (1996).

The benefit of this additional term in periodic systems is controversial. It is unclear whether the additional computational resource in comparison to LDA really leads to improved results (Filippi et al., 1994; Khein et al., 1995; Lee and Martin, 1997).

### 2.1.3.3 LDA+ $U$

Transition-metal and rare-earth element contain very localized  $d$ - or  $f$ -electrons. As a result, the systems containing them are not well described by LDA or GGA. To improve LDA approximation, an orbital-dependent correction term that accounts for strong electronic correlations in localized  $d$ - or  $f$ -shells is added to the LDA potential (Anisimov et al., 1991; Liechtenstein et al., 1995). This approach separates electron states into two groups: the localized electronic states with strong mutual Coulomb repulsions modeled by a Hubbard-like  $U$  term, and the delocalized electronic states described by the orbital-independent one-electron potential.

The LDA+ $U$  method can partially improve the band gap error, mainly by shifting the VBM (Nieminen, 2009). However, the intrinsic error in the position of the CBM due to the self-interaction, which is generally accounted for a large part of band gap underestimation, remains.

A number of methods to determine the Hubbard parameter,  $U$ , were introduced. One of them is by finding the  $U$  that gives either the correct (experimental) band gap or correct (experimental) location of the  $d$  (or  $f$ ) state which in many cases leads to unphysically huge value of  $U$  (Lany and Zunger, 2008). Another more theoretically sound way to calculate  $U$  is based on first-principle calculations

proposed by Janotti et al. (2006). First, the atomic correlation energy,  $U^{\text{at}}$ , is defined from the energy difference between the addition and the removal of an electron from the atomic  $d$ -subshell written by

$$U^{\text{at}} = [E_{\text{tot}}(d^{n+1}) - E_{\text{tot}}(d^n)] - [E_{\text{tot}}(d^n) - E_{\text{tot}}(d^{n+1})], \quad (2.21)$$

where  $E_{\text{tot}}(d^n)$  is the total energy of an isolated atom with  $n$  electrons occupying the  $d$  sub-shell.  $n = 9$  is normally used as reference because most of atomic  $d$  sub-shell in metal species in semiconductors are completely occupied.

Because the atomic Coulomb correlation interaction is screened by the optical dielectric constant,  $\varepsilon^\infty$ , when these atoms are in a solid, the Hubbard-like Coulomb interaction is given by

$$U = \frac{U^{\text{at}}}{\varepsilon^\infty}. \quad (2.22)$$

#### 2.1.4 Hybrid Functionals

Because the non-local nature of the exchange functional is not well described by either LDA or GGA, the hybrid functionals were introduced in hope to overcoming band-gap error problems. In this approach, the exchange potential is created by mixing the local (LDA) [or semi-local (GGA)] exchange potentials and the non-local Hartree-Fock exchange potential, while the correlation potential remains described by either LDA (or GGA). One of the most popular hybrid functionals is called B3LYP (Becke, 1993b). B3LYP employed Becke's three-parameter exchange functional (B3) and Lee, Yang, and Parr (LYP) correlations. The use of B3LYP is well known for its improved description of molecular systems (Paier et al., 2007) and widely used for non-periodic systems.

Recently, the use of hybrid functionals for periodic systems including the study of defects in within a periodic solid became possible when Heyd, Scuse-ria, and Ernzerhof (HSE) introduced a screening length in the exchange poten-tial (Heyd et al., 2006). For HSE, the exchange potential is separated into the short- and long-range parts. In the short-range part, the mixture between the GGA exchange potential of Perdew, Burke, and Ernzerhof (PBE) (Perdew et al., 1996) and non-local Hartree-Fock exchange potential in the ratio of 75/25 is used. The long-range exchange potential and correlation are described by just the PBE functional. The HSE functional has been reported to greatly improve the values of band gap in many materials (Marsman et al., 2008; Paier et al., 2006) . Note, however, that due to the use of the Hartree-Fock potential, the hybrid functional calculations require much more (at least an order of magnitude more) computa-tional resources than calculations using just the local-potentials.

### 2.1.5 Plane Waves

Plane waves (PWs) are mathematical functions that are uncomplicated and are suitable to use as a basis set for describing electronic wavefunctions of periodic systems. The major advantage of the plane wave basis set, compared to an atomic orbital basis set, is that plane waves do not vary with ionic posi-tions (Marx and Hutter, 2000). As a result, the Hellmann-Feynman theorem can be used straightforwardly without the so-called Pulay terms. Other advantages include good descriptions of delocalized states, orthogonality, and simple control of convergence (energy cutoff). Moreover, PWs by themselves are solutions to the zero-potential Schrödinger equations. Bloch's theorem stated that, for a periodic system, each electronic wavefunction can be written as a product of a periodic function or Bloch function,  $u_{n,\mathbf{k}}(\mathbf{r})$ , and a plane wave envelope,  $e^{i\mathbf{k}\cdot\mathbf{r}}$ . It can be

written as (Payne et al., 1992)

$$\Psi_{n,\mathbf{k}}(\mathbf{r}) = e^{i\mathbf{k}\cdot\mathbf{r}} u_{n,\mathbf{k}}(\mathbf{r}), \quad (2.23)$$

where

$$u_{n,\mathbf{k}}(\mathbf{R} + \mathbf{r}) = u_{n,\mathbf{k}}(\mathbf{r}). \quad (2.24)$$

The size of the PW basis set is defined in terms of given reciprocal vector within the first Brillouin zone  $\mathbf{k}$  and reciprocal lattice vector  $\mathbf{G}$ ,

$$|\mathbf{k} + \mathbf{G}\rangle = \frac{1}{V} e^{i(\mathbf{k}+\mathbf{G})\cdot\mathbf{r}}, \quad \frac{\hbar^2}{2m} |\mathbf{k} + \mathbf{G}|^2 \leq E_{cut}, \quad (2.25)$$

where  $V$  is the volume of crystal and  $E_{cut}$  is the energy cutoff.

Although, PWs have various advantages, they also have disadvantages. A PW basis set is not suitable for describing the localized nature of the fast-oscillating wavefunctions near a nucleus. To avoid this problem, a replacement of atomic potentials with smoother potentials, called pseudopotentials, is made.

### 2.1.6 Pseudopotentials Method

Although the PW basis set has many advantages, it cannot describe core states unless very well unless an extremely high energy cutoff is used. However, it is computationally impractical to represent the strong-oscillation wavefunctions in the core region with a PW basis set with a very high energy cutoff (Heine, 1970). It is known that the fully occupied inner shells are strongly bound to the nucleus and inert. Therefore, it is possible to replace the nuclear potential and the chemically inert core electrons with an effective smooth potential called pseudopotential. In

other words, it is a good approximation to treat the combination of the core electrons and nucleus as a hypothetical external potential, or pseudopotential, acting on the valence electrons. The pseudopotential can be separated into two regions (Stibor, 2001):

I). The *core-region* defined as the interior of a sphere with cut-off radius  $R_c$ , is the region where, in reality, the core electrons are tightly situated. Neighboring atoms do not noticeably influence these core electrons. The actual electron wavefunctions in this region are rapidly oscillating while the actual potential is strongly attractive. Both the potential and the electron wavefunctions in this region are difficult to describe using a plane wave basis set.

II). The *interatomic-region* is the home of valence electrons which are responsible for the interatomic binding. The valence electrons wavefunctions and potential in this region oscillate slowly and can describe well by a PWs basis set.

Philips and Kleinman (1959) introduced a way to construct a smooth valence-wavefunction,  $\tilde{\psi}_v$ , which is orthogonalized to the core states,  $\psi_c$ , written by

$$|\tilde{\psi}_v\rangle = |\psi_v\rangle + \sum_c \alpha_{cv} |\psi_c\rangle, \quad (2.26)$$

where  $\alpha_{cv} = \langle \psi_c | \tilde{\psi}_v \rangle \neq 0$ . The reformulation of this pseudo-wavefunction with modified Schrödinger equation gives a pseudo-Hamiltonian that can be written as

$$\tilde{H}_{ps} = \hat{H} + \sum_c (\varepsilon_v - \varepsilon_c) |\psi_c\rangle \langle \psi_c|, \quad (2.27)$$

where  $\hat{H} = \hat{T} + \hat{V}$ ,  $\hat{V} = (Z_c/r)\hat{I}$  represents the bare potential of the nuclei where  $\hat{I}$  is the identity operator. This pseudo-Hamiltonian has similar eigenvalues to those of the original one. However, its wavefunction is smoother and nodeless. Its

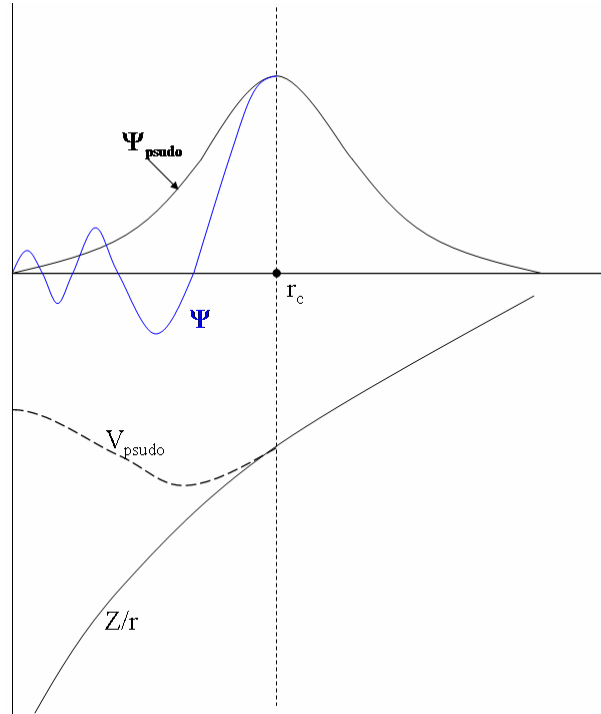


**Figure 2.1** All-electron potential and pseudopotential as well as their corresponding wavefunctions.

associated potential, namely pseudopotential, can be written as

$$\hat{V}_{\text{PS}} = \frac{Z_c}{r} \hat{I} + \sum_c (\varepsilon_v - \varepsilon_c) |\psi_c\rangle \langle \psi_c|, \quad (2.28)$$

or in a more general form

$$\hat{V}_{\text{PS}}(\mathbf{r}) = \sum_{l=0}^{\infty} \sum_{m=-l}^l v_{\text{PS}}^l(\mathbf{r}) |lm\rangle \langle lm| = \sum_{l=0}^{\infty} v_{\text{PS}}^l(\mathbf{r}) \hat{P}_l, \quad (2.29)$$

where  $v_{\text{PS}}^l(\mathbf{r})$  represents the pseudopotential associated with an angular component  $l$  and  $\hat{P} = \sum_{m=-l}^l |lm\rangle \langle lm|$  is a projection operator of the  $l^{\text{th}}$  angular momentum.

The valence electron wavefunctions that are solutions to the pseudopotential have their nodal structure removed, making them suitable to be described

using a PW basis set. Fig. 2.1 shows a comparison between the pseudopotential and the actual atomic potential. This replacement of the potential in the core region strongly affects only the electron wavefunctions within the core region; leaving the wavefunction in the interatomic-region intact.

In summary, the pseudopotential with a PW basis set has three major advantages: (1) a PW basis set does not depend on atomic positions, (2) the completeness of the basis set is controlled by a single parameter, the planewave cutoff energy, and (3) the kinetic energy matrix is already diagonal in Fourier space, whereas the potential energy matrix is diagonal in real space. The transformation between the two spaces can be done by various Fourier transform schemes.

### 2.1.6.1 Projector Augmented-Wave Method (PAW)

PAW method was first introduced by Blöchl (1994) in order to improve the pseudopotential approach. It combines the concepts of ultrasoft pseudopotential and linearized augmented plane-waves (LAPW) method. All-electron properties are retained by decomposing the all-electron wavefunctions in terms of a smooth pseudo-wavefunction outside the core region and a rapidly-varying contribution localized within the core region. The relationship between all-electron and pseudo-wavefunctions is written as

$$|\psi_{\text{AE}}^n\rangle = |\psi_{\text{PS}}^n\rangle + \sum_{I=1}^P \sum_{l,m} \sum_i (|\phi_{\text{AE}}^{iI lm}\rangle - |\phi_{\text{PS}}^{iI lm}\rangle) \langle \tilde{p}_{\text{PS}}^{iI lm} | \psi_{\text{PS}}^n\rangle, \quad (2.30)$$

where  $\phi_{\text{AE}}^{iI lm}$  is all-electron partial wavefunctions centering on atom  $I$ .  $\phi_{\text{PS}}^{iI lm}$  is the pseudo-atomic partial wavefunctions matching the all-electron ones outside a cutoff radius.  $\tilde{p}_{\text{PS}}^{iI lm}$  represents a projector function with the defining relation

$\langle \tilde{p}_i^{ilm} | \psi_{\text{PS}}^n \rangle = \delta_{ij}$ . The sums from Eqn. (2.30) run over all the atomic sites  $I$ , angular momentum  $(l, m)$ , and the projector function index  $i$ . The calculated electronic density can be divided into three parts: a soft pseudo-charge density from  $\psi_{\text{PS}}^n$  and two localized charge densities relating to  $\phi_{\text{AE}}^{ilm}$  and  $\phi_{\text{PS}}^{ilm}$ . PAW method freezes the core orbitals and allows only the valence wavefunctions to be varied in the same way as the pseudopotential method. As a result, it has the efficiency of the pseudopotential plane-wave method without losing the core states. This makes it one of the most powerful and widely used methods.

### 2.1.7 Brillouin Zone, k-points, and the Monkhorst-Pack Method

In the study of arbitrary material systems, it is difficult to describe an electron that interacts with the huge number of ions that produce the external potential. However, for crystalline materials, the problem can be vastly simplified by taking advantage of the periodicity of the ionic potential. Based on Bloch theorem (Bloch, 1928; Kittel, 1996), the total electronic energy per (real space) unit cell of an infinite crystal can be calculated by integrating the energies of all occupied eigenstates within the first BZ. Other properties such as electron density can also be calculated by integrating over the first BZ as well. In practice, the integration over the BZ can be replaced by a summation. For example, to evaluate the integral over the  $i^{\text{th}}$  band inside the BZ of a function  $f_i(\mathbf{k})$ , one can approximate it by a summation

$$\frac{1}{\Omega_{\text{BZ}}} \int_{\text{BZ}} d\mathbf{k} f_i(\mathbf{k}) \Rightarrow \bar{f}_i = \frac{1}{N_k} \sum_{\mathbf{k}} f_i(\mathbf{k}), \quad (2.31)$$

where  $\Omega_{\text{BZ}}$  is the volume of the first BZ and  $N_k$  is the number of  $k$ -point.

To do this, one needs to solve the Kohn-Sham equations for every  $k$ -point inside the first BZ that are used in the integral. In reality, the integral of the eigenenergies converges as a function of  $k$ -points rather quickly. Therefore, only a limited sampling set of  $k$ -points is actually needed. Monkhorst and Pack (Monkhorst and Pack, 1976) introduced a special way to choose the set of sampling  $k$ -points within the first BZ that works well and have been widely used given as follow

$$\vec{k}_{n_1, n_2, n_3} = \sum_1^3 \frac{2n_i - N_i - 1}{2N_i} \vec{G}_i, \quad (2.32)$$

where  $N_i$  is the number of  $k$ -points in each direction and  $n_i = 1, 2, 3, \dots, N_i$ .

### 2.1.8 Force Acting on Ions

Forces on ions can be divided based on their sources: (1) the force from the ion-ion interaction and (2) the force from the ion-electron interaction.

The force from ion-ion interaction can be written as

$$F_I^{ion-ion} = -\frac{\partial}{\partial \mathbf{R}_I} U^{ion-ion} = \frac{1}{2} \sum_{J \neq I} \frac{Z_I Z_J e^2}{|\mathbf{R}_I - \mathbf{R}_J|} (\mathbf{R}_I - \mathbf{R}_J). \quad (2.33)$$

The force from ion-electron interaction can be calculated according to Hellmann-Feynman theorem (Feynman, 1939; Hellmann, 1937). The theorem states that the derivative of the energy with respect to any parameter is equal to the expectation value of the derivation of the Hamiltonian operator. A force on an atom  $I$  at position  $\mathbf{R}_I$  is, therefore, given by

$$F_I^{ion-el} = -\left\langle \psi_0 \left| \frac{\partial H}{\partial \mathbf{R}_I} \right| \psi_0 \right\rangle, \quad (2.34)$$

where  $H$  is the Hamiltonian of the system and  $|\psi_0\rangle$  is the normalized ground state

wavefunction.

From both forces, the total force can be written as

$$\begin{aligned}
 F_I &= F_I^{ion-ion} + F_I^{ion-el} \\
 &= \frac{1}{2} \sum_{J \neq I} \frac{Z_I Z_J e^2}{|\mathbf{R}_I - \mathbf{R}_J|} (\mathbf{R}_I - \mathbf{R}_J) - \left\langle \psi \left| \frac{\partial H}{\partial \mathbf{R}_i} \right| \psi \right\rangle \\
 &= \frac{1}{2} \sum_{J \neq I} \frac{Z_I Z_J e^2}{|\mathbf{R}_I - \mathbf{R}_J|} (\mathbf{R}_I - \mathbf{R}_J) - \int d\mathbf{r} n(\mathbf{r}) \frac{\partial V_{ext}(\mathbf{r})}{\partial \mathbf{R}_I}, \quad (2.35)
 \end{aligned}$$

where  $\mathbf{R}_I$  is the position of the  $I^{th}$  nucleus. The final line shows that the force can actually be calculated from just the electron density and those terms in the Hamiltonian that depend explicitly on the atomic positions  $R$ , namely  $V_{ext}$ .

## 2.2 The VASP Codes

The Vienna Ab Initio Simulation Package (VASP) (Kresse and Furthmüller, 1996a; Kresse and Furthmüller, 1996b) is a pseudopotential-based package that utilizes DFT and periodic boundary conditions. It uses a plane wave basis set to describe electron wavefunctions. In this thesis, a special type of pseudopotential called ultrasoft pseudopotentials (Kresse and Hafner, 1994; Vanderbilt, 1990) which allows a low energy cutoff for PWs basis set is used. The Ceperley and Alder method (Ceperley and Alder, 1980) with the correlation described by the Perdew and Zunger (Perdew and Zunger, 1981) in the exchange-correlation energy calculations is employed. There are also many types of exchange-correlation energy implemented in the codes such as LDA and various versions of GGA. (The most recent version of VASP also has the non-local hybrid functional exchange-correlation implemented.) The  $k$ -point sampling is based on the Monkhorst-Pack approach (Monkhorst and Pack, 1976). The lattice parameters and atomic posi-

tions are allowed to relax using a conjugate gradient scheme. The Methfessel and Paxton method (Methfessel and Paxton, 1989) is applied to treat partial band occupancy of electrons.



# CHAPTER III

## CALCULATION METHODS FOR DEFECTS

### IN SEMICONDUCTORS

In this chapter, a brief methodology for studying defects in semiconductors is given. First-principles calculations allow one to study various material systems in an unbiased way. This includes the study of behaviors and properties of defects in semiconductors. Based on first-principles calculations, one can explore a variety of properties of defects in a crystal, for e.g., the defect formation energy (see section 3.2), the electrical and (visible) optical properties, the infrared absorption signatures, the x-ray absorption signatures of impurities (see Chapter IV), and others. Next we will describe the most fundamental property that determines the existence of a particular defect, i.e., the equilibrium defect concentration.

#### 3.1 Defect Concentration

The thermodynamic equilibrium concentration of a defect is given by Van de Walle and Neugebauer (2004)

$$c = N_{\text{sites}} \exp\left(-\frac{E^f}{kT}\right), \quad (3.1)$$

where  $E^f$  is the defect formation energy,  $N_{\text{sites}}$  is the number of allowed sites that a defect can be incorporated on,  $k$  is the Boltzmann constant, and  $T$  is the temperature. Note that the concentration determined from Eqn. (3.1) is only valid under the thermodynamic equilibrium conditions. In actual growth and heat treatment

processes, the conditions are often far away from the thermodynamic equilibrium conditions and many defects can be incorporated in a high concentration even though they would be forbidden under equilibrium conditions. However, Eqn. (3.1) is still very useful to evaluate the tendency of the existence of defects. The defect with high formation energy will occur in a low concentration.

### 3.2 Defect Formation Energy

As described in the previous section, the formation energy plays a key role in determining the existence of a defect. Note that, in order to study a system with defects (or, for that matter, the structure of a pure system), the atomic structure needs to be optimized in order to reach the lowest energy configuration. In the supercell approach, the formation energy of an impurity  $D$  in charge state  $q$  is defined as (Zhang and Northrup, 1991)

$$E^f = E_{\text{tot}}[D^q] - E_{\text{tot}}[\text{Bulk}] + \sum_x \Delta n_x \mu_x + q(E_F + E_v) \quad (3.2)$$

where  $E_{\text{tot}}[D^q]$  is the total energy of the supercell containing the defect  $D$  in charge state  $q$ .  $E_{\text{tot}}[\text{Bulk}]$  is the total energy of the same supercell without any defect.  $\Delta n_X$  is the number of species  $X$ , being removed from ( $\Delta n_x < 0$ ) or added to ( $\Delta n_x > 0$ ) a defect-free supercell to form the defect supercell. The energy of atoms in species  $X$  is referenced to their respective reservoir with chemical potential,  $\mu_x$ . The chemical potential represents the energy that a particle has in its external reservoir, which affects the net energy change when it is incorporated into the material, and is discussed in next section.  $E_F$  is the Fermi level referenced with respect to the valence band maximum (VBM) of the bulk system, i.e.,  $E_F = 0$  at VBM.  $E_v$  is the VBM of the bulk crystal.

From Eqn. (3.2) we can see that the formation energy depends on both the elemental chemical potentials and electron potential (Fermi energy). As a result, the formation energy is often plotted as a function of chemical potential or as a function of Fermi energy. The former case is useful for evaluating the best growth conditions to incorporate specific defects while the latter case is useful for investigating the behaviors of defects and impurities when the carrier concentrations change.

Actually, the energy used in Eqn. (3.1) should be the Gibbs free energy. Using the formation energy from Eqn. (3.2) in Eqn. (3.1) implies that the contributions from vibrational entropy are ignored. In most cases of defects in semiconductors, these entropy contributions from the first term and second term in Eqn. (3.2) are largely cancelled out and the difference is generally small enough not to affect qualitative conclusions. This is especially true when the defect does not significantly disturb the bulk vibrational behaviors.

### 3.3 Chemical Potential

The allowed chemical potential of a particular element depends on experimental growth conditions. For example, for  $\text{TiO}_2$ , the growth conditions can be Ti-rich, O-rich or anything in between. These growth conditions can be expressed through the values of Ti and O chemical potentials. So, if there is an abundance of oxygen in the growth environment then the chemical potential of O will be high and this, according to Eqn. (3.2), tends to favor the incorporation of O into the sample. The allowed ranges of the Ti and O chemical potentials are first limited by the elemental phase precipitations. For Ti, the upper limit of  $\mu_{\text{Ti}}$ , called Ti-rich condition, is given by  $\mu_{\text{Ti}}^{\text{max}} = \mu_{\text{Ti}}[\text{Bulk}]$ , where  $\mu_{\text{Ti}}[\text{Bulk}]$  is the energy (per atom) of metal Ti. Exceeding this chemical potential limit will cause the metal Ti phase

to form in actual growth. In a similar manner, the O-rich condition, which is the upper limit of  $\mu_{\text{O}}$  is given by  $\mu_{\text{O}}^{\text{max}} = \mu_{\text{O}[\text{O}_2]}$ , which is the energy of half  $\text{O}_2$  molecule. Again, if  $\mu_{\text{O}}$  rises above this limit its natural phase ( $\text{O}_2$ ) will start to precipitate inhibiting the formation of  $\text{TiO}_2$ .

In addition to the upper limits mentioned above, smooth equilibrium growth of  $\text{TiO}_2$  also requires that

$$\mu_{\text{Ti}} + 2\mu_{\text{O}} = E_{\text{tot}} [\text{TiO}_2] \quad (3.3)$$

where  $E_{\text{tot}} [\text{TiO}_2]$  is the total energy of a three-atom unit of bulk  $\text{TiO}_2$ . Eqn. (3.3) shows that  $\mu_{\text{O}}$  and  $\mu_{\text{Ti}}$  are not totally independent. Under Ti-rich conditions, the targeted  $\mu_{\text{O}}$  for equilibrium growth is

$$\mu_{\text{O}}^{\text{min}} = (E_{\text{tot}} [\text{TiO}_2] - \mu_{\text{Ti}[\text{Bulk}]}) / 2. \quad (3.4)$$

Under Ti-rich condition, if one sets  $\mu_{\text{O}}$  below this value then the sample will start to vaporize while setting it above this value will cause rapid unequilibrium growth. Similarly, the O-rich growth conditions set the lower limit on  $\mu_{\text{Ti}}$

$$\mu_{\text{Ti}}^{\text{min}} = E_{\text{tot}} [\text{TiO}_2] - 2\mu_{\text{O}[\text{O}_2]}. \quad (3.5)$$

Any given equilibrium growth condition can be described using the chemical potential values  $\mu_{\text{Ti}}$  or  $\mu_{\text{O}}$ .  $\mu_{\text{Ti}}$  can be any value between  $\mu_{\text{Ti}}^{\text{min}}$  and  $\mu_{\text{Ti}}^{\text{max}}$ . The value of  $\mu_{\text{O}}$  can be calculated from the value of  $\mu_{\text{Ti}}$  using Eqn. (3.3). To relate the calculated formation energy with experimental measurements which often give the heat of formation of material. The heat of formation of  $\text{TiO}_2$  can be found using

the relationship

$$E_{\text{tot}} [\text{TiO}_2] = \mu_{\text{Ti}[\text{Bulk}]} + \mu_{\text{O}[\text{O}_2]} + \Delta H_f [\text{TiO}_2], \quad (3.6)$$

where  $\Delta H_f [\text{TiO}_2]$  is the heat of formation, which is negative for a stable compound.

More strict limitations on the chemical potentials may be further imposed by considering other possible compound phases containing both Ti and O. This is discussed in more detail in Chapter IV.

### 3.4 Defect Transition Level

Point defects in a semiconductor can introduce levels in the band gap. Depending on the defect, the level can be a deep level or a shallow level near the band edges. Electrons (or holes) can be excited to and from these levels. There are several experimental techniques that can be used to detect these levels. To study deep levels, deep-level transient spectroscopy (DLTS) and photoluminescence (PL) experiments (Troxell and Watkins, 1980) are generally used. For shallow levels, temperature-dependence Hall measurements (Chand et al., 1984) and admittance spectroscopy (cite) can be used. First-principles calculations can provide defect levels based on a given defect structure for comparison with experimental measurements.

When an experimentalist reports the transition levels (associated with a particular defect), there are two kinds; a thermodynamic transition level and an optical transition level. The thermodynamic transition level ( $\varepsilon_{q_1/q_2}$ ) is the electron energy position where defects in charge states  $q_1$  and  $q_2$  have equal formation energy. When calculating the formation energies both defects in charge states  $q_1$

and  $q_2$  are fully relaxed to their equilibrium configuration. Using DLTS experiments and temperature-dependence Hall measurements, one can observe this type of level. The optical transition level is defined in a similar way as the thermodynamic transition level, except that the final state  $q_2$  does not have time to relax from the  $q_1$  state configuration. This type of level is measured using optical excitation techniques such as photoluminescence (PL) experiments. In this work, the attention is focused on the thermodynamic transition levels. Based on Eqn. (3.2),  $\epsilon(q_1/q_2)$  can be calculated from

$$\epsilon(q_1/q_2) = \frac{E^f(D^{q_1}; E_F = 0) - E^f(D^{q_2}; E_F = 0)}{q_2 - q_1}, \quad (3.7)$$

where  $E^f(D^q; E_F = 0)$  is the formation energy of a defect  $D$  in charge state  $q$  when the electron's Fermi level is at the valence band maximum ( $E_F=0$ ). If the Fermi level of the system is lower than  $\epsilon(q_1/q_2)$ , charge state  $q_1$  is stable. On the other hand, if the Fermi level of the system is higher than  $\epsilon(q_1/q_2)$ , charge state  $q_2$  is more stable. For the cases where  $\epsilon(q_1/q_2)$  lies close to the band edges such that the defect can be thermally ionized at room temperature, the level is called a shallow level.

### 3.5 Defect Complex Binding Energy

Two or more defects can bind to each other forming a defect complex. The simplest case is a defect complex  $AB$  consisting of two constituents, defect  $A$  and defect  $B$ . The chemical reaction to form the defect complex is expressed as (Van de Walle and Neugebauer, 2004)



where  $E_b$  is the binding energy which is the energy released from the reaction. It can be calculated from formation energies following the equation

$$E_b = E^f(A) + E^f(B) - E^f(AB). \quad (3.9)$$

Positive binding energy implies that defect  $A$  and  $B$  prefer to bind with each other as a pair. However, one should be careful that having positive binding energy alone does not guarantee that the defect complex will form. The actual formation process of a defect complex also depends on other parameters such as the absolute formation energies of each of the isolated defects and the complex, as well as the temperature, charge balance, and diffusivity of the defects. The formation energy of the defect complex,  $E^f(AB)$ , should be much lower than both of the isolated defects  $E^f(A)$  and  $E^f(B)$  in order to achieve a substantial concentration of the defect complex (in comparison with the amount of constituent defects). However, if the formation energy of a defect complex is comparable to those of the constituent defects, the concentration of the defect complex can be smaller due to its much smaller configurational entropy (assuming diluted limits).

# CHAPTER IV

## SULFUR IMPURITIES IN ANATASE-TiO<sub>2</sub>

### 4.1 Introduction

TiO<sub>2</sub> is a photocatalyst which is used in various applications, especially for air and water purifications (Hoffmann, 1995; Diebold, 2003; Hashimoto et al., 2005). Although, it has several advantages over other materials, such as better oxidizing power and chemical stability, it has major drawback. Its large band gap (3.0-3.2 eV) does not permit efficient absorption of visible light. To narrow the band gap of the TiO<sub>2</sub> without compromising its photocatalytic properties is a clear goal. When TiO<sub>2</sub> is doped with some elements, such as C, N, and F, good photocatalytic properties are observed (Hattori et al., 1998; Asahi et al., 2001; Khan et al., 2002; Di Valentin et al., 2004; Wang and Lewis, 2005). Sulfur-doped TiO<sub>2</sub> has been found to both enhancing and inhibiting the photocatalysis reactions. S-doped TiO<sub>2</sub>, prepared by oxidative annealing of TiS<sub>2</sub> has been found to have a lower band gap than that of pure-TiO<sub>2</sub>, giving a higher photocatalytic activity under the visible light (Umebayashi et al., 2002; Umebayashi et al., 2003). However, S impurities in some experiments can inhibit the photocatalytic reactions (Rodriguez et al., 1998; Hebenstreit et al., 2000). Whether S impurities can enhance or prevent the photocatalytic reactions, it would be helpful to know how S is incorporated into TiO<sub>2</sub>. In the present study S impurities in anatase-TiO<sub>2</sub> are explored.

Using first-principles calculations, single-S defects in anatase-TiO<sub>2</sub> have been studied. These include substitutional sulfur on the titanium site (S<sub>Ti</sub>), substitutional sulfur on the oxygen site (S<sub>O</sub>), and sulfur interstitial (S<sub>i</sub>). It is found

that all sulfur defects can have low formation energies, depending on the growth conditions.

## 4.2 Computational Method and the Calculation Parameters

Density functional theory (DFT) within the local density approximation (LDA) and ultrasoft pseudopotentials (Vanderbilt, 1990) as implemented in the VASP codes (Kresse and Furthmüller, 1996a) are used in the calculations. The cutoff energy for the plane-wave basis set is set at 300 eV. The calculated (fully relaxed) crystal parameters of bulk anatase-TiO<sub>2</sub> are  $a = 3.764 \text{ \AA}$ ,  $c/a = 2.515$ , and  $u = 0.208$ . These are in good agreement with the experimental values:  $a = 3.785 \text{ \AA}$ ,  $c/a = 2.513$ , and  $u = 0.208$  (Howard et al., 1991). Other calculations (Fahmi et al., 1993; Asahi et al., 2000; Calatayud et al., 2001) also showed a similar agreement. To calculate the formation energy of defects, a supercell approach is used (Zhang and Northrup, 1991; Northrup and Zhang, 1994; Zhang et al., 2001). All atoms are allowed to relax by minimization of the Hellmann-Feynman force to less than 0.05 eV/Å. Our preliminary study is based on a supercell containing 48 atoms, i.e., a  $2 \times 2 \times 2$  repetition of the primitive anatase unit cell. To ensure the convergence of the calculations, all the calculations are repeated with a larger supercell size of 108 atoms, i.e., a  $3 \times 3 \times 2$  repetition of the primitive anatase unit cell. It is found that formation energies and transition levels calculated using the 48-atom cell are in good agreement with those calculated using the 108-atom cell as shown in Table 4.1. For formation energies, all agreements are within 0.6 eV (best case: S<sub>i</sub><sup>0</sup> and S<sub>O</sub><sup>0</sup>, 0.03 eV; worst case: S<sub>i</sub><sup>4+</sup>, 0.6 eV). For the Brillouin zone integration, a  $2 \times 2 \times 2$  Monkhorst-Pack special  $k$ -point mesh is used. Note that, all detailed results presented here, unless noted otherwise, are based on the 108-atom

cell calculations. The electronic structures are investigated based on the special  $k$ -points calculated; following Ref. (Zhang, 2002). The calculated band gap averaged over the special  $k$ -points is 2.44 eV which is still narrower than the experimental band gap of 3.2 eV (Tang et al., 1993) due to the well-known LDA gap error.

**Table 4.1** Formation energy of S defects in anatase-TiO<sub>2</sub> and its corresponding transition levels  $\varepsilon(q_1/q_2)$  with O-rich conditions is  $\mu_S = -3.00$  eV.

Defect	Charge state	$E^f$ (eV) (Ti-rich)		$E^f$ (eV) (O-rich)		$\varepsilon(q_1/q_2)$ (eV)	
		48-atom	108-atom	48-atom	108-atom	48-atom	108-atom
S <sub>i</sub>	0	3.74	3.71	7.53	7.5	2.24	2.04
	+4	-5.04	-4.44	-1.25	-0.65		
S <sub>Ti</sub>	0	5.79	5.93	2	2.14	1.43	1.46
	+2	2.96	3.01	-0.83	-0.78		
S <sub>O</sub>	0	1.75	1.72	9.33	9.3	1.66	1.58
	+2	-1.56	-1.45	6.02	6.13		

**Table 4.2** Formation energy of S defects in anatase-TiO<sub>2</sub> and its corresponding transition levels  $\varepsilon(q_1/q_2)$  with O-rich conditions is  $\mu_{s[\text{orth}]} = -4.52$  eV.

Defect	Charge state	$E^f$ (eV) (Ti-rich)		$E^f$ (eV) (O-rich)		$\varepsilon(q_1/q_2)$ (eV)	
		48-atom	108-atom	48-atom	108-atom	48-atom	108-atom
S <sub>i</sub>	0	3.05	2.85	3.05	2.85	2.24	2.04
	+4	-5.89	-5.3	-5.89	-5.3		
S <sub>Ti</sub>	0	5.12	5.07	-2.46	-2.51	1.43	1.46
	+2	2.26	2.15	-5.32	-5.43		
S <sub>O</sub>	0	1.05	0.86	4.84	4.65	1.66	1.58
	+2	-1.56	-1.45	6.02	6.13		

From supercell calculations, the formation energy of an impurity  $D$  in charge state  $q$  is defined as

$$E^f = E_{\text{tot}}[D^q] - E_{\text{tot}}[\text{TiO}_2, \text{bulk}] + \sum_x \Delta n_x \mu_x + q(E_F + E_v). \quad (4.1)$$

where  $E_{\text{tot}}[D^q]$  is the total energy of the supercell containing the defect  $D$  in charge state  $q$ .  $E_{\text{tot}}[\text{TiO}_2, \text{bulk}]$  is the total energy of  $\text{TiO}_2$  supercell without any defect.  $\Delta n_X$  is the number of species  $X$ , being removed from ( $\Delta n_x < 0$ ) or added to ( $\Delta n_x > 0$ ) a defect-free supercell to form the defect supercell. The energy of atoms in species  $X$  is referenced to their respective reservoir with chemical potential,  $\mu_x$ .  $E_F$  is the Fermi level referenced with respect to the valence band maximum (VBM) of bulk  $\text{TiO}_2$ .  $E_v$  is the VBM of bulk  $\text{TiO}_2$ .

For the illustration purposes, the formation energy of S interstitial in  $\text{TiO}_2$  can be written as

$$E^f[\text{S}_i^q] = E_{\text{tot}}[\text{S}_i^q] - E_{\text{tot}}[\text{TiO}_2, \text{bulk}] - \mu_s + q(E_F + E_v), \quad (4.2)$$

and the formation energy of substitutional S on the Ti site in  $\text{TiO}_2$  as

$$E^f[\text{S}_{\text{Ti}}^q] = E_{\text{tot}}[\text{S}_{\text{Ti}}^q] - E_{\text{tot}}[\text{TiO}_2, \text{bulk}] - \mu_s + \mu_{\text{Ti}} + q(E_F + E_v). \quad (4.3)$$

During the growth, if any chemical potential rises above its natural phase value (i.e., that of hcp Ti,  $\text{O}_2$ , and  $\text{S}_2$  molecules), then the natural phase will form instead of the  $\text{TiO}_2$ . Therefore, only the  $\mu_X$  values below those of the natural phases need to be considered. More strict limitations on the chemical potentials may be imposed by the formation of alternative phases containing Ti and O, sulfur-titanium as well as sulfur-oxygen phases, as discussed below.

For equilibrium growth to take place, the chemical potential values  $\mu_i$  have to obey the following conditions:

(i) To avoid precipitation of Ti, O, and the elemental dopant S,  $\mu_i$  are bound by

$$\mu_{\text{Ti}} < 0, \mu_{\text{O}} < 0, \mu_{\text{S}} < 0. \quad (4.4)$$

This is because all the chemical potentials are reference to their respective natural phase, i.e., hcp Ti, O<sub>2</sub> and solid S.

(ii)  $\mu_i$  of Ti and O are also related, in order to form TiO<sub>2</sub> in equilibrium, by the condition

$$\mu_{\text{TiO}_2} = \mu_{\text{Ti}} + 2\mu_{\text{O}}. \quad (4.5)$$

When  $\mu_X = 0$  is set as their respective natural phases, we obtained  $\mu_{\text{TiO}_2}$  per molecular formula (one Ti and two O).

In addition to TiO<sub>2</sub>, in certain growth conditions (certain domain in the phase space of  $\mu_{\text{Ti}}$  and  $\mu_{\text{O}}$ ), there may be other phases of titanium-oxygen compounds turns more stable. This would indicate that such compound would form instead of TiO<sub>2</sub>; rendering such growth condition unusable. It has been shown (Naphattalung et al., 2006) that the real upper limit of chemical potential of titanium ( $\mu_{\text{Ti}}$ ) is precipitated by Ti<sub>2</sub>O<sub>3</sub> at -2.67 eV.

(iii) To avoid the formation of the secondary phases of titanium-sulfur compounds or sulfur-oxygen compounds, the compounds in the general formula Ti<sub>m</sub>S<sub>n</sub> and S<sub>n</sub>O<sub>m</sub> have to be studied to see if any of them further posed an additional

limit.  $\mu_i$  are bound by following relationships:

$$n\mu_s + m\mu_{\text{Ti}} \leq \Delta H_f(\text{Ti}_m\text{S}_n) \quad (4.6)$$

or

$$n\mu_s + m\mu_{\text{O}} \leq \Delta H_f(\text{S}_n\text{O}_m). \quad (4.7)$$

The sulfur-titanium stable phases which may exist are TiS, TiS<sub>2</sub>, and Ti<sub>2</sub>S<sub>3</sub> whereas the sulfur-oxygen stable phases are SO, SO<sub>2</sub>, and SO<sub>3</sub>. It is found that the most stable sulfur compound under Ti-rich condition is TiS<sub>2</sub> (with the calculated formation energy of -6.00 eV) and the most stable sulfur compound under O-rich condition is SO<sub>3</sub> (with the calculated formation energy of -5.43 eV). Figure 4.1 shows the calculated chemical potential regions under equilibrium growth condition for TiO<sub>2</sub>:S in two dimension in two dimension ( $\mu_{\text{Ti}}$ ,  $\mu_{\text{O}}$ ). The upper bound of  $\mu_s$  under Ti-rich condition ( $\mu_{\text{Ti}} = -2.67$  eV,  $\mu_{\text{O}} = -3.97$  eV) is -3.00 eV. If  $\mu_s$  rises above this value, the precipitate TiS<sub>2</sub> phase will form; inhibiting the incorporation of S into TiO<sub>2</sub>. Under O-rich condition ( $\mu_{\text{O}} = 0$  eV, and  $\mu_{\text{Ti}} = -10.25$  eV), the upper bound of  $\mu_s$  is further reduced to -5.43 eV. If  $\mu_s$  rises above this value, the precipitate SO<sub>3</sub> phase will form; inhibiting the incorporation of S into TiO<sub>2</sub>. Strictly speaking, the  $\mu_s$  has to be controlled under the limits for Ti-rich and O-rich conditions at -3.00 and -5.43 eV, respectively. However, the calculated formation energy by using these values causes difficulty to compare the formation of defects under different growth conditions. To overcome this problem,  $\mu_s$  is fixed as a constant both under Ti-rich and O-rich conditions at its solid phase value

$$\mu_s = \mu_s(\text{solid}) = \mu_s(\alpha\text{-sulfur}) = -0.81\text{eV}. \quad (4.8)$$

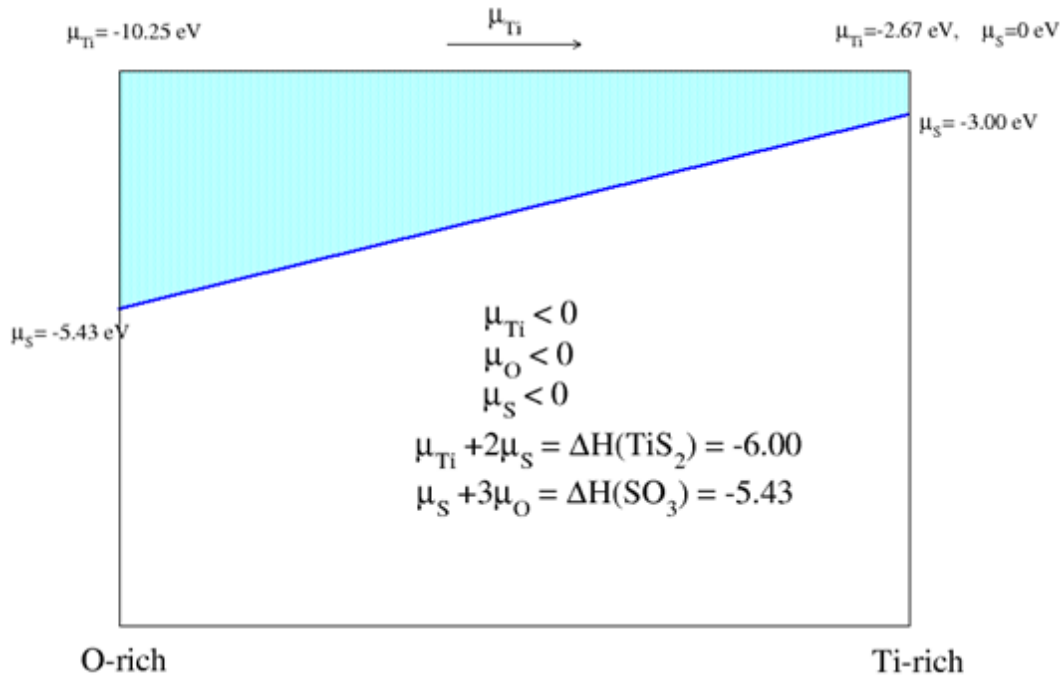


**Figure 4.1** Calculated domain for equilibrium growth of  $\text{TiO}_2:\text{S}$  as a function of  $\mu_{\text{Ti}}$  (or  $\mu_{\text{O}}$ ) and  $\mu_{\text{S}}$ .

This allows one to find the best growth condition to incorporate sulfur into the desired site in anatase- $\text{TiO}_2$ .

## 4.3 Results and Discussions

### 4.3.1 Formation Energies and Charge States

Figure 4.2 shows the calculated atomic structures of  $(\text{SO})_{\text{O}}$ ,  $\text{S}_{\text{O}}^0$ , and  $\text{S}_{\text{Ti}}^0$ . Their defect formation energies are tabulated in Table 4.1 and 4.2, as well as plotted as a function of the electron Fermi energy in Figure 4.3 and 4.4. For Table 4.1 and 4.3, the  $\mu_{\text{S}}$  are based on the maximum values allowed under Ti-rich and O-rich conditions. For Table 4.2 and Figure 4.4, the  $\mu_{\text{S}}$  is fixed at the solid phase value of sulfur. From Figure 4.3 and 4.4, we can see that the formation energies

of sulfur defects in anatase-TiO<sub>2</sub> show the similar trend ( $\mu_S$  just shifted the entire plot but relative energies among defects for each condition remain unchanged). Under Ti-rich conditions,  $S_i$  is the predominant defect. On the other hand,  $S_{Ti}$  is the leading defect for O-rich conditions. All S-defects introduce deep defect levels inside the band gap.

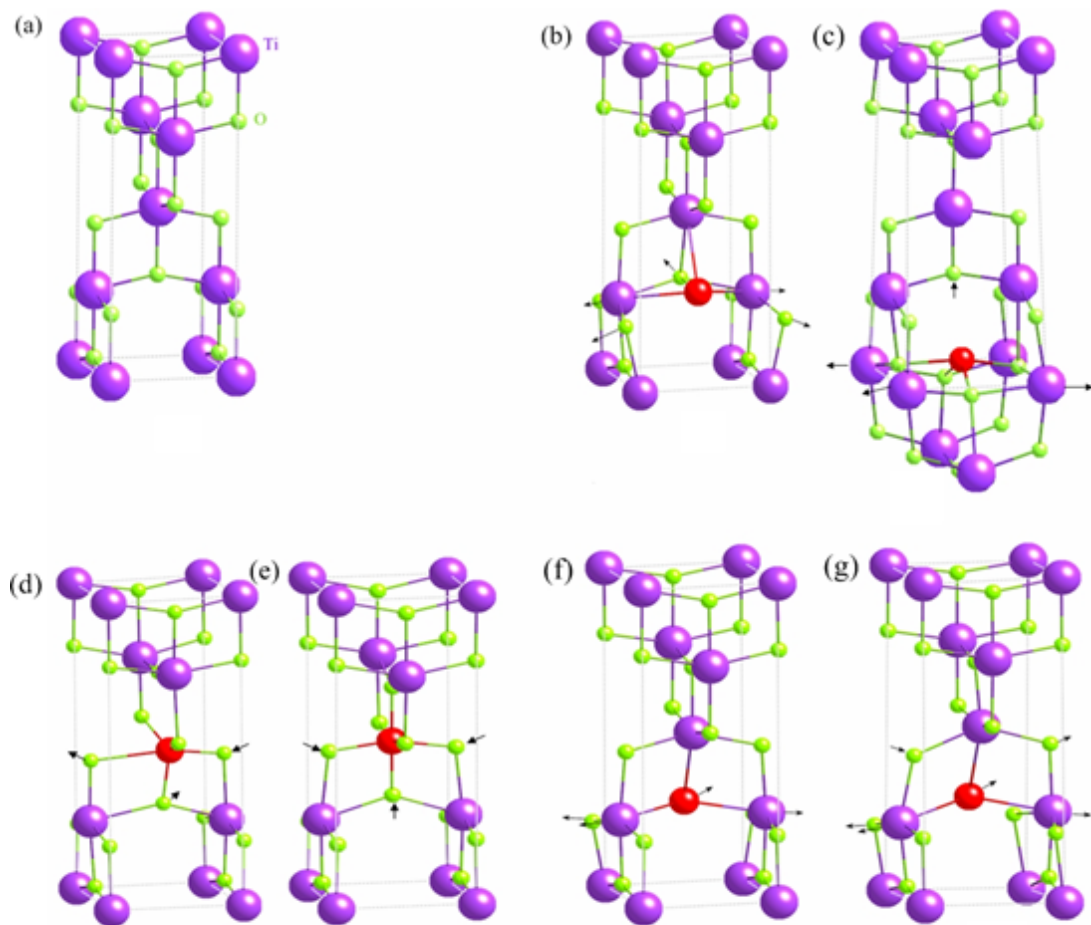


**Figure 4.2** Atomic structures of Bulk,  $(SO)_O$ ,  $S_i^{4+}$ ,  $S_{Ti}^0$ ,  $S_{Ti}^{2+}$ ,  $S_O^0$  and  $S_O^{2+}$ .

## 4.3.2 Structure and Stability of the Sulfur Defects

### 4.3.2.1 Sulfur Interstitial

Isolated interstitial S in neutral charge state has high formation energy and is hence unstable. It spontaneously binds with an O on the lattice site, forming a substitutional SO molecule,  $(\text{SO})_{\text{O}}$ . This substitutional diatomic molecules is similar to those in the cases of small diatomic molecules substitution for O in ZnO (Limpijumnong et al., 2005) and  $\text{TiO}_2$  (Na-Phattalung et al., 2006). On the other hand, an interstitial S in 4+ charge state favors an octahedral site which is similar to that of titanium interstitial in 4+ charge state,  $\text{Ti}_i^{4+}$  (Na-Phattalung et al., 2006). As shown in Figure 4.2 (b) and (c), stable charge states are 0 and 4+, respectively and other charge states have higher energy at all Fermi energy and are never stable. A neutral  $(\text{SO})_{\text{O}}$  has two more electrons compared to a free SO molecule in the vacuum (the additional two electrons are donated from the surrounding Ti). The substitutional SO with neutral charge state has a bond length of 1.75 Å which is longer than that of a free SO 1.48 Å (Greenwood and Earnshaw, 1997) due to additional electrons occupying the antibonding states. The bond lengths of the substitutional SO to the neighboring atoms are 2.35 and 2.10 Å for S-Ti and for O-Ti bonds, respectively. These are longer than that of bulk O-Ti bonds (1.92 Å). The atomic configurations of  $(\text{SO})_{\text{O}}$  and  $\text{Ti}_i^{4+}$  in anatase- $\text{TiO}_2$  are schematically illustrated in Figure 4.2 (b) and (c), respectively.

Under Ti-rich and *p*-type condition ( $E_F$  is at the VBM), the formation energy of  $\text{S}_i^{4+}$  is -4.44 eV which is the lowest among all sulfur defects studied. We, therefore, predicted that it is the predominant defect under Ti-rich *p*-type conditions. Figure 4.3 shows that sulfur interstitial has a low formation energy in *p*-type  $\text{TiO}_2$ , making them a likely compensating center for *p*-type samples. Its formation energy remains negative as long as  $E_F < 1.11$  eV (Figure 4.3, left panel). The negative formation energy means that the defect is spontaneously form under such condition. Under the O-rich condition, the formation energy of  $\text{S}_i$  is higher

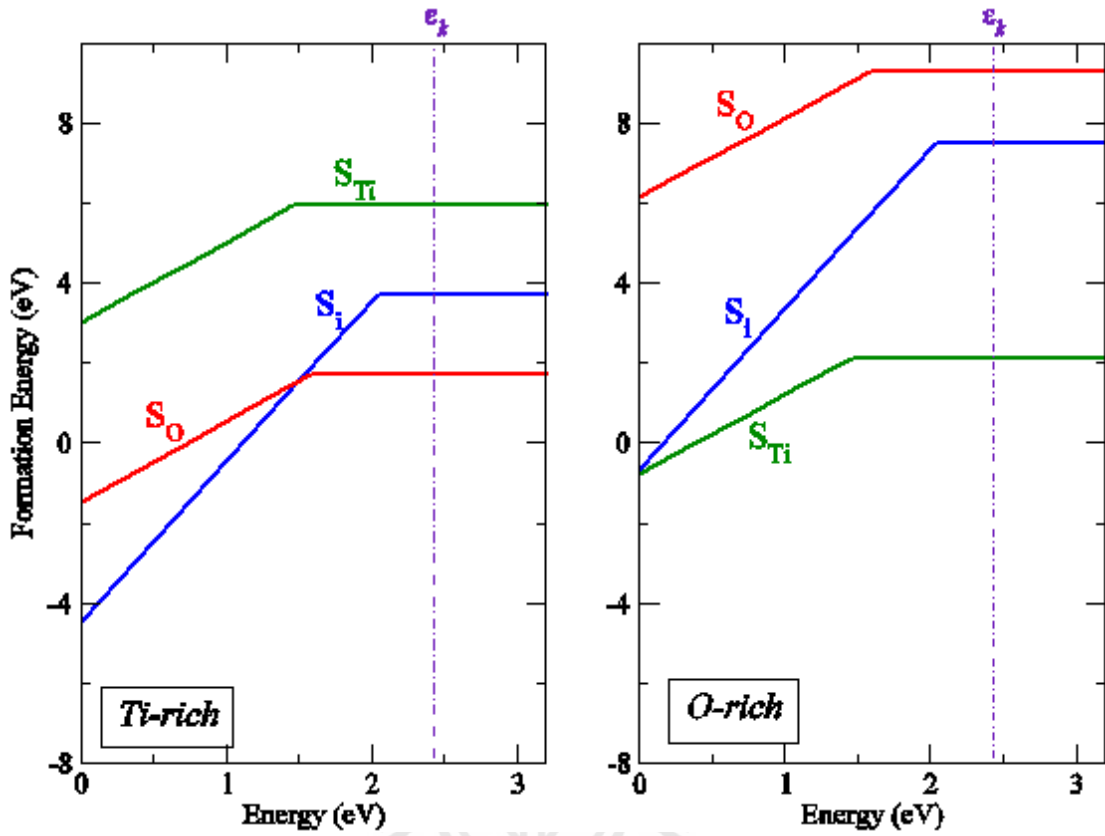


**Figure 4.3** Formation energies of S impurities as a function of the Fermi level, where chemical potential of sulfur is precipitated from  $\text{SO}_3$  and  $\text{TiS}_2$  under Ti-rich (left panel) and O-rich conditions (right panel), respectively.

than the Ti-rich condition.  $\text{S}_i^{4+}$  also has a small region of negative formation energies (see Figure 4.3, right panel).  $(\text{SO})_O$  has higher formation energy than that of  $\text{S}_i^{4+}$  in all conditions. Therefore, it should be easier to create  $\text{S}_i^{4+}$  than  $(\text{SO})_O$ . The transition level  $\varepsilon(4+/0)$  occurs at  $E_F = 2.04$  eV. Figure 4.5 shows the calculated total DOS of the supercell without and with the sulfur interstitial ( $\text{S}_i$ ). The neutral charge  $(\text{SO})_O$  introduces two doubly occupied deep levels denoted by  $p_2$  and  $p_3$ . Other main features of the bulk  $\text{TiO}_2$  DOS remain intact. To understand the nature of the impurity states, the partial density of state (PDOS) of the sulfur atom and its nearest neighbors (NN), i.e., the 3 Ti atoms and 2 O atoms, are calculated and showed in Figure 4.6. The PDOS of these NN atoms are

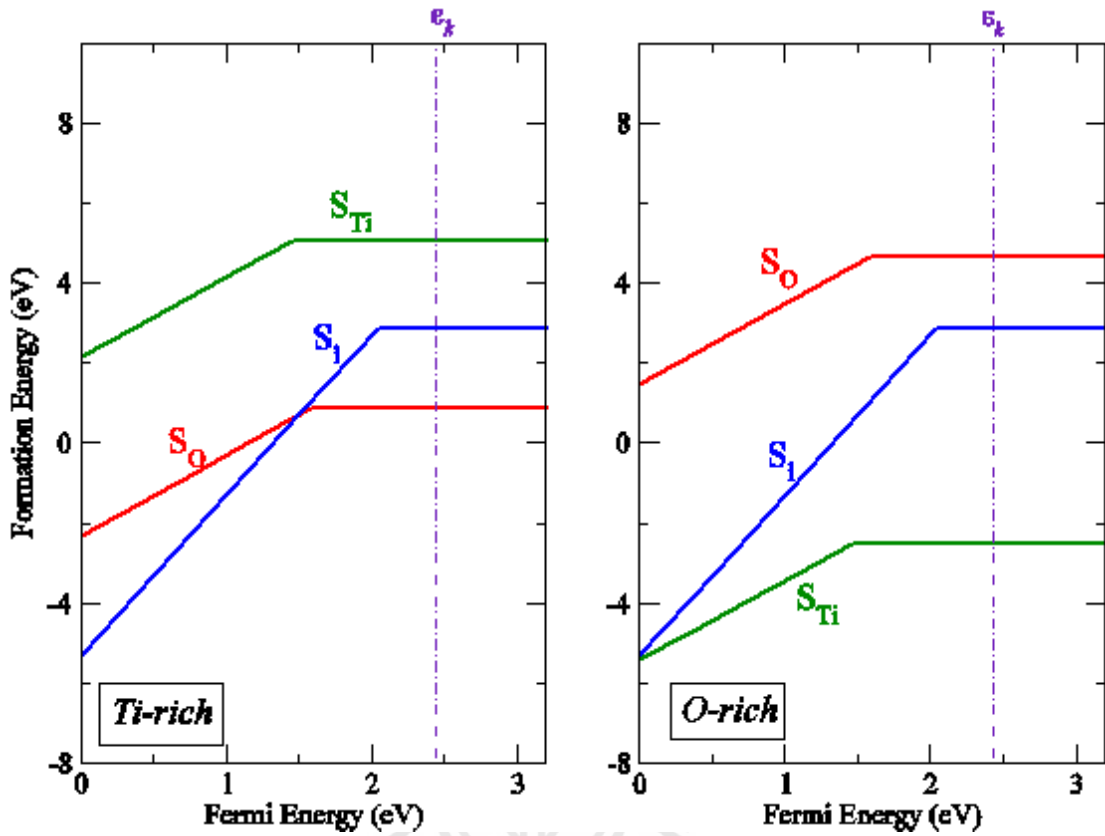


**Figure 4.4** Formation energies of S impurities as a function of the Fermi level, where chemical potential of sulfur is  $\alpha$ -sulfur (orthorhombic), both under the Ti-rich (left panel) and O-rich conditions (right panel).

different from that of the bulk due to the presence of a  $(\text{SO})_{\text{O}}$  defect. It is found that S  $3p$ , O  $2n$ , and Ti  $3d$  orbitals have a significant contribution to the  $p_2$  and  $p_3$  state, meaning that the defect states have substantial contributions from the sulfur atom as well as its NNs. When four electrons are excited from  $p_2$  and  $p_3$  states, the defect left in  $4+$  charge state ( $\text{S}_i^{4+}$ ) as shown in Figure 4.5 (c). In this new configuration, the unoccupied  $p_2$  and  $p_3$  states are shifted to higher energies and are resonances in the CB, while the doubly occupied deep level (denoted by  $p_1$ ) is remained above the VBM. Figure 4.7 shows the PDOS of  $\text{S}_i^{4+}$  and its NN. The occupied impurity level,  $p_1$  state, is mostly composed of S  $3s$ , S  $3p$ , and O  $2p$  orbital. The PDOS results are in agreement with the charge density distribution

of defect states that are localized around the S atom and its neighbors as shown in Figure 4.8.

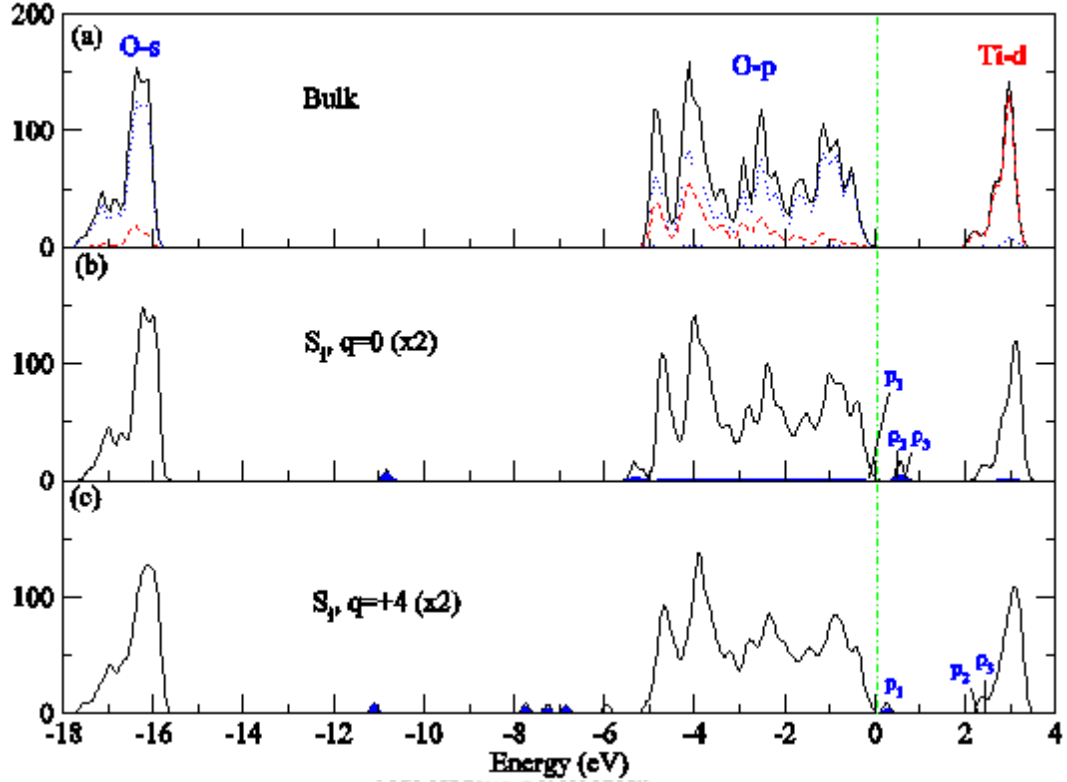


**Figure 4.5** Site decomposed electron density of states (DOS). For each atom center, the local partial DOS in a sphere radius  $R$  (Ti: $R = 1.48 \text{ \AA}$ , O: $R = 0.74 \text{ \AA}$  and S: $R = 1.164 \text{ \AA}$ ) is calculated.

#### 4.3.2.2 Sulfur Substituting on the Titanium Site

Sulfur substituting on the titanium site ( $S_{Ti}$ ) acts as a deep donor with the stable charge states of 0 and 2+ as illustrated by its formation energy in Figure 4.3. The transition level  $\varepsilon(2+/0)$  occurs at 1.46 eV above the VBM. Under the O-rich and  $p$ -type conditions,  $S_{Ti}^{2+}$  has a very low formation energy of -0.78 eV at the VBM and increases as the Fermi energy moves up. This makes it the lowest formation energy among all S defects studied under O-rich conditions. Under

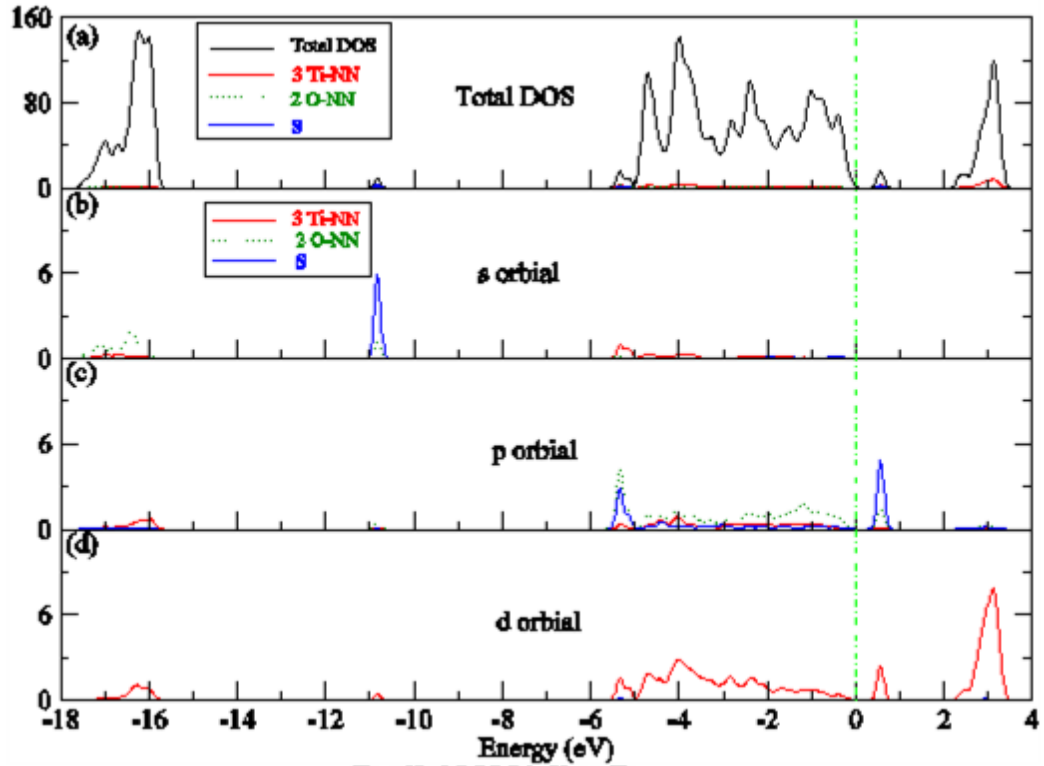


**Figure 4.6** Site decomposed electron density of states (DOS) of defect  $(SO)_O$  compared atomic orbital S plus 3 NN Ti and 2 NN O,  $s$ ,  $p$ , and  $d$  orbital.

Ti-rich conditions,  $S_{Ti}$  has higher formation energy, making it more difficult to form.

Table 4.3 summarizes the local structures (bond distances) of  $S_{Ti}$  in anatase- $TiO_2$ . Their configurations ( $S_{Ti}^0$  and  $S_{Ti}^{2+}$ ) are schematically illustrated in Figure 4.2 (d) and (e), respectively. The substitutional S atom is surrounded by six O neighbors. The S-O bonds are expected to be shorter than the lattice Ti-O bond because the atomic radius of S is smaller than that of Ti ( $R_S$ : 1.05 Å and  $R_{Ti}$ : 1.60 Å). Interestingly, the relaxation does not caused the surrounding neighbors of  $S_{Ti}^0$  to simply breathe inward around the S atom. Instead, S atom relaxes off-center (denoted by  $\Delta d_S$ ) by about 0.4 Å. Due to this off-center relaxation, the local structure of  $S_{Ti}^0$  is not symmetry. This off-center relaxation is due to an extra two electrons of  $S_{Ti}^0$  compared to the Ti atom it is substituting for. When

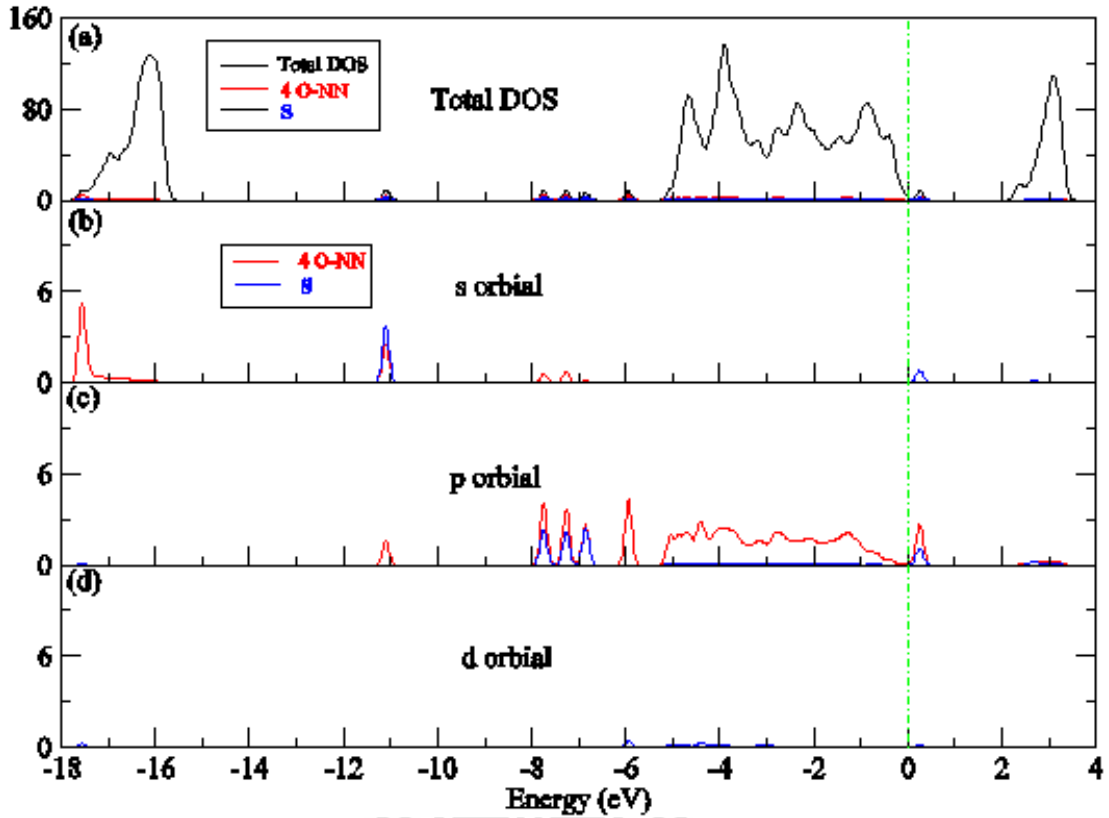


**Figure 4.7** Site decomposed electron density of states (DOS) of defect  $S_i^{4+}$  compared atomic orbital S plus and 4 NN O,  $s$ ,  $p$ , and  $d$  orbital.

the two extra electrons are excited and the charge state turns to  $2+$ , i.e.,  $S_{Ti}^{2+}$ , which leaves the defect with the number of electrons equal to that of the Ti atom it is substituting for, the  $S_{Ti}^{2+}$  does not move off-center. Instead, the neighboring O atoms have large inward relaxation by about 10-15% of the original Ti-O bond length. The S-O bond lengths of the  $S_{Ti}^{2+}$  are 1.72 and 1.67 Å for  $\Delta d_{||}$  and  $\Delta d_{\perp}$ , which are shorter than that of the bulk Ti-O of 1.97 and 1.92 Å by -15.4% and -10.8%, respectively (Table 4.3). Note that, for  $S_{Ti}$ , the  $1+$  charge state is never stable. This characteristic is called negative- $U$  which is normally associated with a large difference in the local structures of two charge states (in this case 0 and  $2+$ ) that causes one of them to have a much lower formation energy; suppressing the existence of the charge state in the middle.

Figure 4.9 shows the calculated total DOS of the supercells without and with the  $S_{Ti}$ . The impurity introduces a doubly occupied deep level denoted by  $p_1$  above the VBM. The PDOS in Figure 4.10 shows that the level has its main components derived from S  $3s$ , S  $3p$ , and O  $2p$  orbitals (of the six NNs). The charge density distribution plots of this level are shown in Figure 4.12. For  $S_{Ti}^0$ , the deep  $p_1$  level is occupied. When two electrons are excited from this  $p_1$  level and the defect changes its charge state to  $2+$ , the unoccupied  $p_1$  level shift higher and appears as a resonance state in the CB. Therefore, the  $S_{Ti}^{2+}$  defect leaves no defect level in the band gap.

**Table 4.3** Relaxation around S substitutes titanium ( $S_{Ti}$ ) in anatase-TiO<sub>2</sub>.

	$S_{Ti}^0$	$S_{Ti}^{2+}$
$\Delta d_s$ (Å)	0.4	0
$\Delta d_{  }$	1.60%	-15.40%
$\Delta d_{\perp}$	0.60%	-10.80%

#### 4.3.2.3 Sulfur Substitute on the Oxygen Site

Sulfur substituting on the oxygen site ( $S_O$ ) is a donor. Figure 4.3 shows the formation energy plot of the defect and shows that its stable charge states are 0 and  $2+$  with transition levels  $\epsilon(2+/0)$  occurs at 1.58 eV above the VBM. Under Ti-rich and  $p$ -type conditions (low  $E_F$  values), the defect has  $2+$  charge state ( $S_O^{2+}$ ) with the formation energy of -1.44 eV at the VBM. Note that, the formation energy is much higher than that of  $S_i^{4+}$ ; illustrating its misfit in size to the O site. The  $1+$  charge state of  $S_O$  ( $S_O^+$ ) has high formation energy and is unstable (negative- $U$  characteristic). Under the O-rich and  $n$ -type condition (large  $E_F$  values),  $S_O$  has even higher formation energy (see Figure 4.3, right panel), making it unlikely to form. Although, S atom is isovalent with the O atom, its covalent radius is much

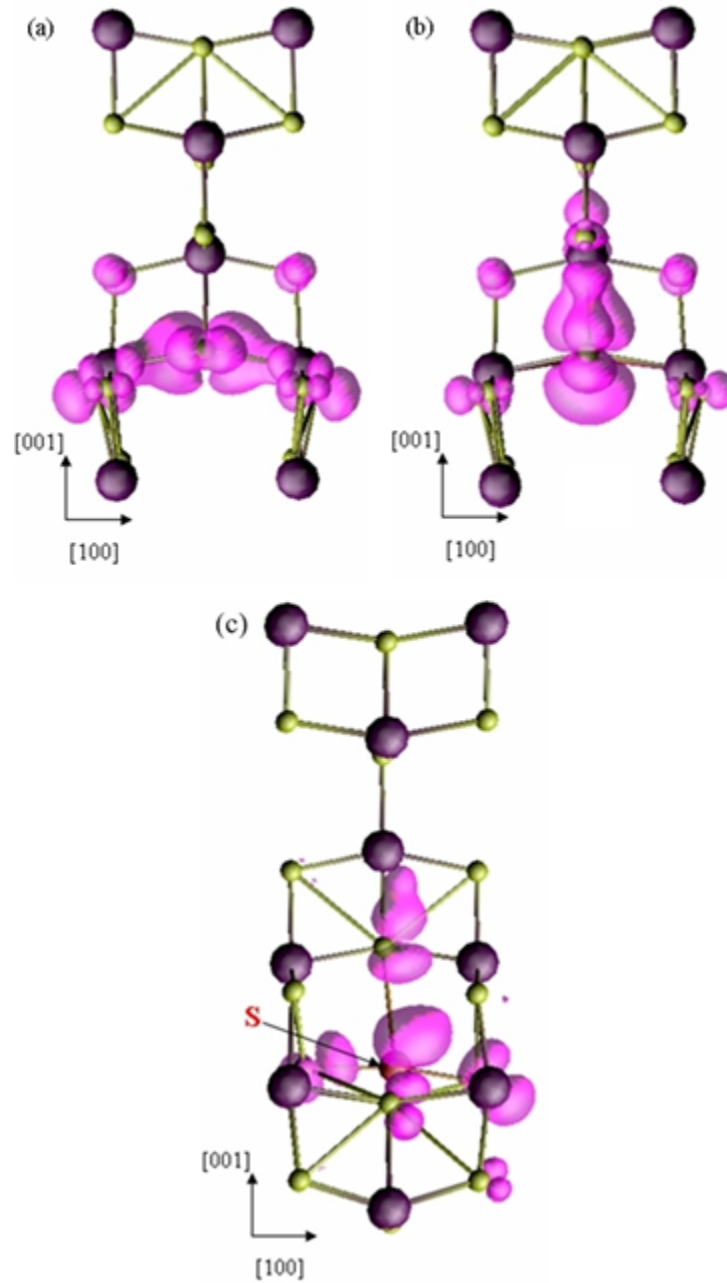


**Figure 4.8** Charge density of defect states of  $S_i$ .

larger than that of O atom [ $R_S$ : 1.05 Å and  $R_O$ : 0.66 Å (Cordero et al., 2008)], causing a large relaxation to the neighboring atoms when it is substituting for the O site.

Table 4.4 shows the parameters describing the atomic configurations of  $S_o$ .

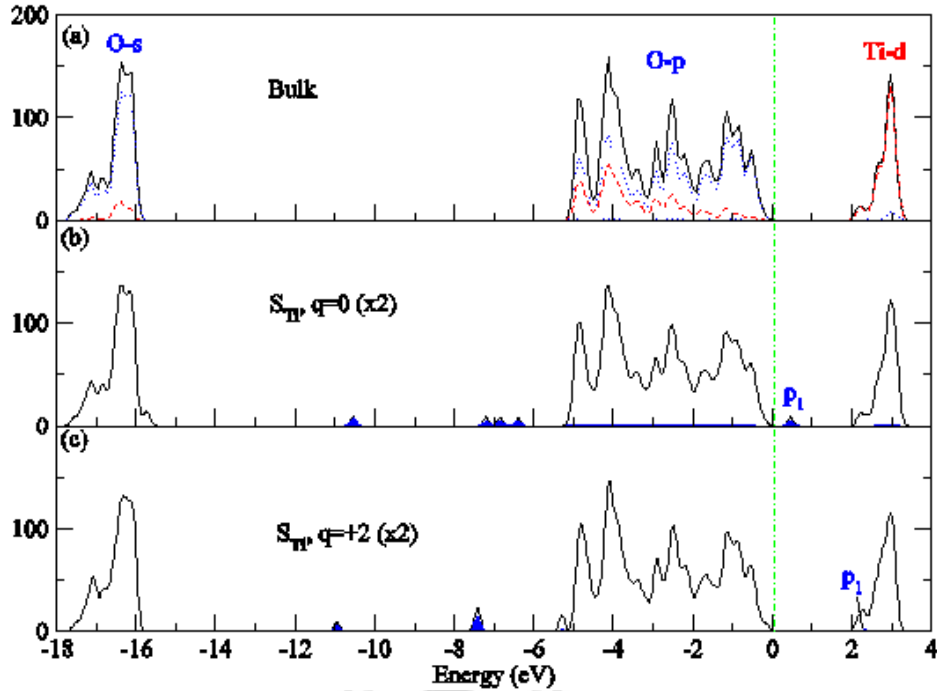


**Figure 4.9** Site decomposed electron density of states (DOS).

in the 0 and 2+ charge states. The local structures are schematically illustrated in Figure 4.2 (f) and (g), respectively. The substitutional S atom is surrounded by three Ti NNs. The S-Ti bond is expected to be longer than the lattice Ti-O bond because of the larger atomic radius of S compared to that of O. Strictly speaking, in the 2+ charge state, the S atom is completely left the O site and forming a strong S-O bond with the next nearest neighbor O leading to a  $(\text{SO})_{\text{O}}\text{-V}_{\text{O}}$  complex. This explains why it can have 2+ charge state, despite the fact that S is isovalent to O that it is substituting for.

For the neutral charge state,  $\text{S}_{\text{O}}^0$ , the S-Ti bond lengths are 2.34 and 2.25 Å for  $\Delta d_{\parallel}$  and  $\Delta d_{\perp}$  which are longer than the corresponding distances of the bulk Ti-O of 1.97 and 1.92 Å by 1.5% and 10.4%, respectively. For  $\text{S}_{\text{O}}^{2+}$ , the S-Ti bond lengths are 2.44 and 2.39 Å for  $\Delta d_{\parallel}$  and  $\Delta d_{\perp}$  which are longer than those corresponding distances of the bulk Ti-O by 7.2% and 12.8%, respectively. The

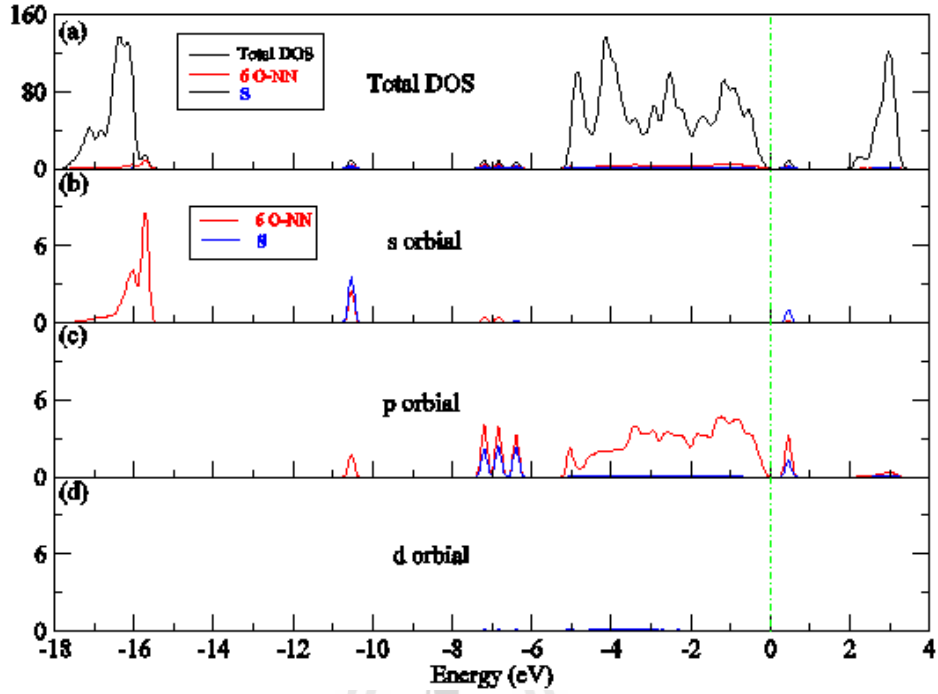


**Figure 4.10** Site decomposed electron density of states (DOS) of defect  $S_{Ti}^0$  compared atomic orbital S plus and 6 NN O,  $s$ ,  $p$ , and  $d$  orbital.

**Table 4.4** Relaxation around S substitutes oxygen ( $S_O$ ) in anatase- $TiO_2$ .

	$S_O^0$	$S_O^{2+}$
$\Delta d_s$ (Å)	0.8	1.0
$\Delta d_{  }$	1.5%	7.2%
$\Delta d_{\perp}$	10.4%	12.8%

large off-center (off plane) displacement from the nominal substitutional S site are observed to be 0.76 and 1.05 Å for  $S_O^0$  and  $S_O^{2+}$ , respectively).

Figure 4.13 shows the calculated total DOS of the supercell without and with the  $S_O$ . In the neutral charge state, the impurity introduces three doubly occupied deep levels denoted by  $p_1$ ,  $p_2$ , and  $p_3$ . To interpret the nature of these defect states, the PDOS of the sulfur atom and three NN Ti atoms are shown in

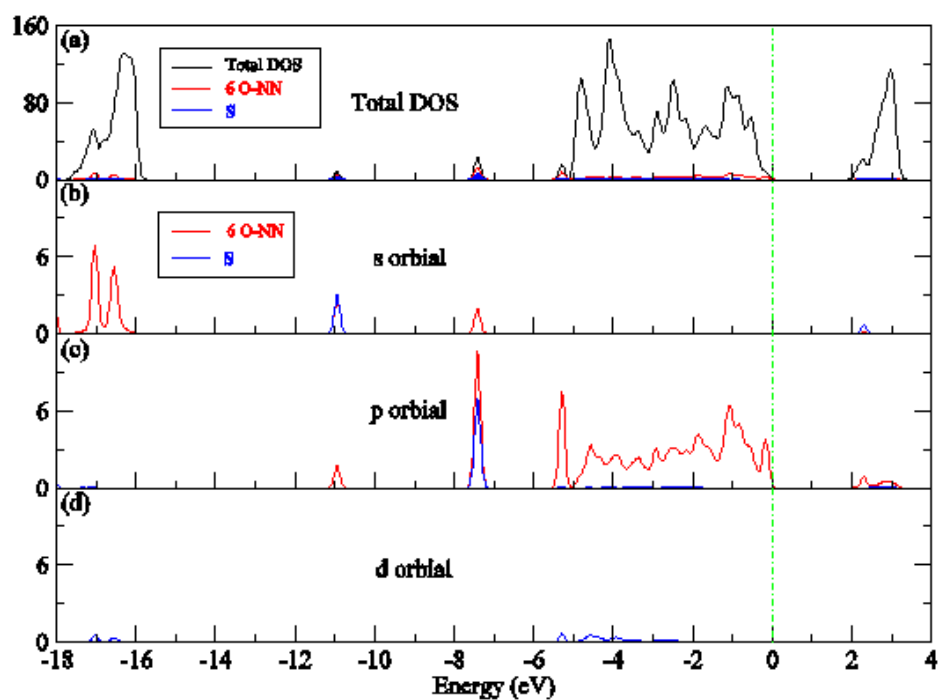


**Figure 4.11** Site decomposed electron density of states (DOS) of defect  $S_{Ti}^{2+}$  compared atomic orbital S plus and 6 NN O,  $s$ ,  $p$ , and  $d$  orbital.

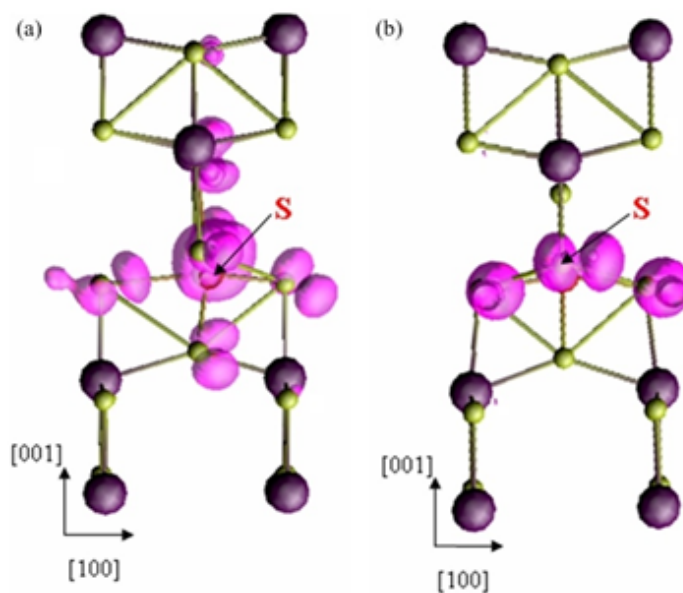


**Figure 4.12** Charge density of a defect state of  $S_{Ti}$ .

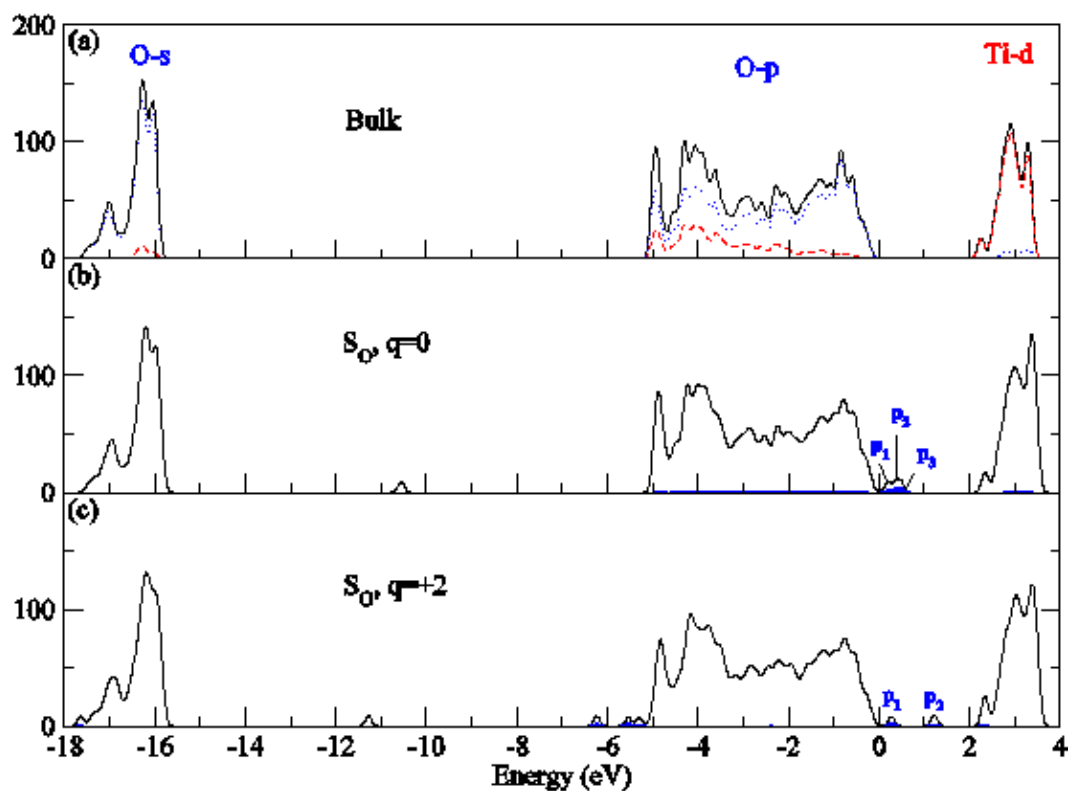
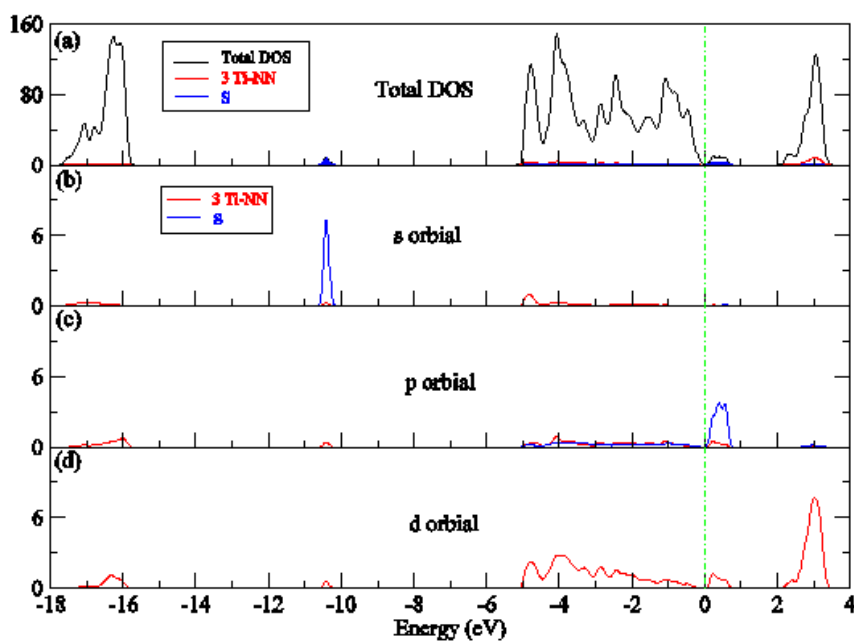
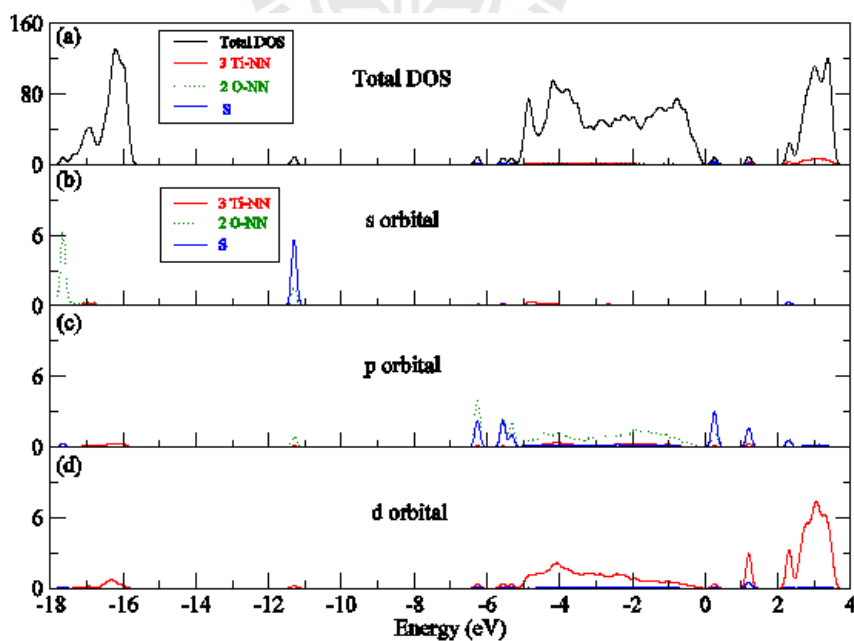


Figure 4.13 Site decomposed electron density of states (DOS).

Figure 4.14 - 4.15. The decomposition of the PDOS with respect to their angular momentum components indicates that the  $p_1$ ,  $p_2$ , and  $p_3$  states are derived from the S  $3_p$  and Ti  $3_d$  orbitals. When the S atom moves away from the site to bind with the next neighboring O, the unoccupied  $p_3$  level shifts above the CBM. Removing two electrons from this level leads to 2+ charge state. The other two doubly occupied deep levels (denoted by  $p_1$  and  $p_2$ ) remain in the gap. The charge density distribution plots are shown in Figure 4.16. The electrons are localized on the S atom and its NNs.



**Figure 4.14** Site decomposed electron density of states (DOS) of defect  $S_O^0$  compared atomic orbital S plus 3 NN Ti,  $s$ ,  $p$ , and  $d$  orbital.



**Figure 4.15** Site decomposed electron density of states (DOS) of defect  $S_O^{2+}$  compared atomic orbital S plus 3 NN Ti and 2 NN O,  $s$ ,  $p$ , and  $d$  orbital.

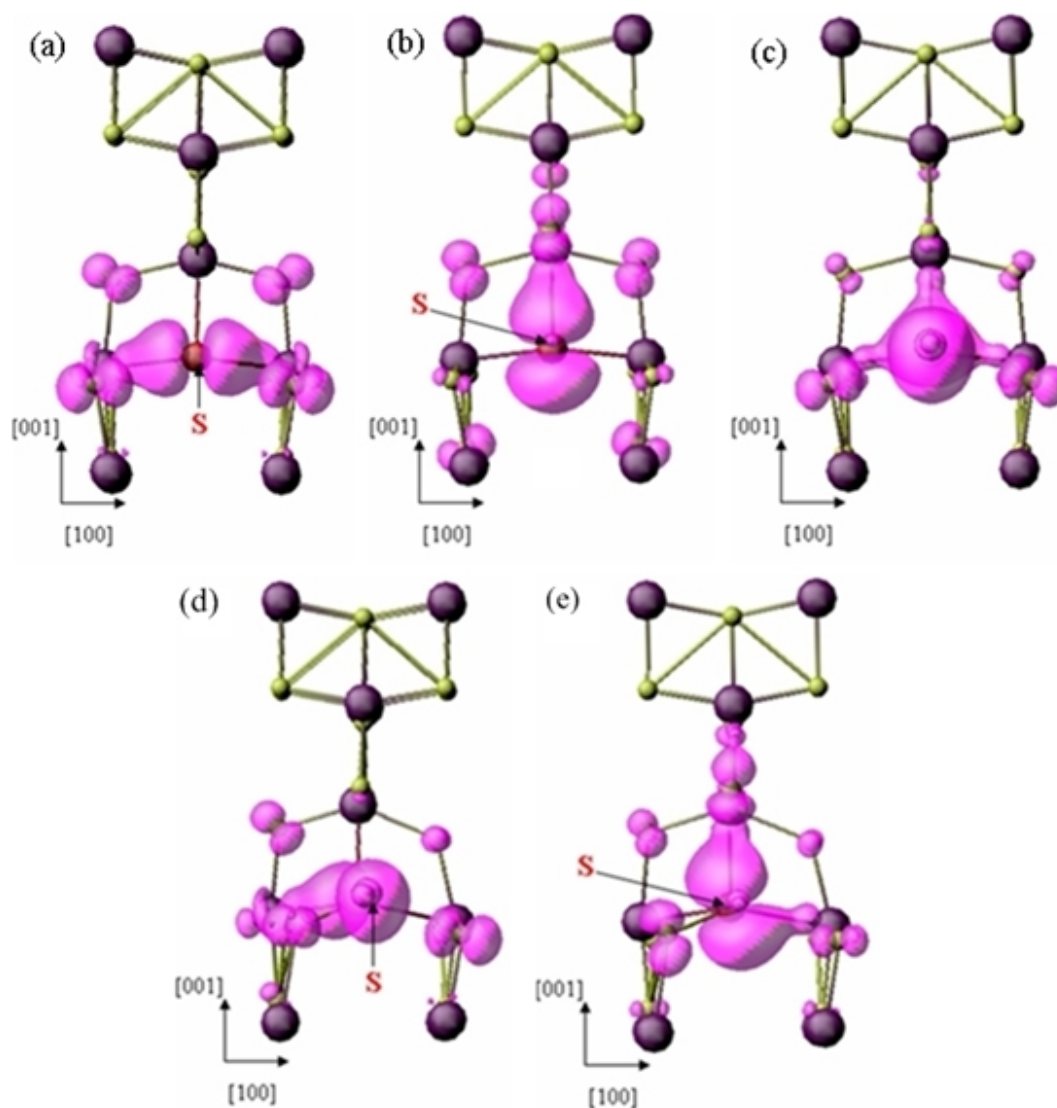


**Figure 4.16** Charge density of defect states of  $S_{\text{O}}^0$  and  $S_{\text{O}}^{2+}$ .

#### 4.4 Conclusions

The calculated results of sulfur defects in anatase- $\text{TiO}_2$  including the detailed information on the atomic structures, charge distribution plots and electronic properties are reported. It is found that all of the studied sulfur defects act as donors. Under Ti-rich condition,  $S_{\text{O}}$  and  $S_i$  have low formation energies, especially under  $p$ -type conditions. On the other hand,  $S_{\text{Ti}}$  and  $S_i$  have low formation energies under O-rich conditions. Due to the low formation energy of  $S_i$  under

both Ti-rich and O-rich conditions,  $S_i$  should be the leading defect in S-TiO<sub>2</sub>, especially under *p*-type conditions. Our calculations also show that all three sulfur defects,  $S_i$ ,  $S_{Ti}$ , and  $S_O$ , introduce deep defect levels inside the band gap.



# CHAPTER V

## CODOPING IN ANATASE-TiO<sub>2</sub>

### 5.1 Introduction

TiO<sub>2</sub> is a photocatalyst used in various applications such as air and water purification (Hoffmann, 1995; Diebold, 2003; Hashimoto et al., 2005). Many researchers have directed their attention towards the development of TiO<sub>2</sub> as a photocatalyst using solar energy. Although TiO<sub>2</sub> has high oxidizing power and high chemical stability, which make it indeed suitable for photocatalysis, its major drawback is a large band gap (3.23 eV), limiting its absorption to only a small portion of the solar spectrum. To increase the activation by sunlight, TiO<sub>2</sub> should be engineered to have a narrower band gap. If this effort were successful then, TiO<sub>2</sub> could be used to split water to acquire hydrogen as a clean and renewable energy source (Gai et al., 2009). In addition, it could be used more effectively as an antibacterial agent (Han et al., 2009). There are reports (Gai et al., 2009) on the possibility to narrow the bandgap of TiO<sub>2</sub> by doping with anions. However, anion-doping generally leads to a lower photocatalytic activity (Fujishima et al., 2007). This is likely due to a reduction of the redox potential of either the photoelectron or photohole. While reducing the band gap leads to an increase in visible light absorption, it gives weaker potentials, either less negative electron potential or less positive hole potential (Byrne et al., 2011). As a result, the photocatalytic activity under visible light is found to be less than that under UV light.

We believe that this problem can be remedied by choosing the dopants carefully. Moreover, if two different kinds of dopant are introduced simultaneously,

so-called codoping, then the effects of the right combination could be more beneficial than that of any single species. Each application requires different electron and hole potentials, and thus different appropriate doping elements. To select a suitable codopant for the desired application, the type of impurity, codopant location, position of impurity levels, and semiconductor-interface reactions of reactive oxygen species (ROS) as well as their redox potentials have to be considered. Developing  $\text{TiO}_2$  photocatalysts that have a high photo quantum yield, strong redox potential and, at the same time, that utilize visible-light photons is among the most challenging subjects in present photocatalytic research.

There are a large number of research works focusing on the doping of  $\text{TiO}_2$  by anions [B (Zaleska et al., 2008), C (Di Valentin et al., 2004), N (Asahi et al., 2001; Asahi and Morikawa, 2007), chalcogen (Zheng et al., 2010), and halogen atoms (Asahi et al., 2001; Umebayashi et al., 2002)] or cations (Emeline et al., 2008). The main focus of those works was on band gap narrowing in the hope of improving solar photocatalytic efficiency. Although monodoping can reduce the band gap, it generally introduces partially occupied defect levels that acts as carrier recombination centers. As a result, it reduces the carrier mobility and the photocatalytic activity of the sample (Umebayashi et al., 2002). In this work, a passivated codoping approach, a way to reduce the band gap without creating recombination centers, is explored. When the defect bands are successfully passivated, the levels will no longer act as carrier-recombination centers (Ahn et al., 2007; Huda et al., 2008; Gai et al., 2009). This should suppress the carrier recombination center problems in  $\text{TiO}_2$  (Gai et al., 2009).

In this thesis, I used first-principles calculations to study various passivated codoping models that can red-shift the  $\text{TiO}_2$  absorption edge. The aim is to find codoping pairs that could enhance photocatalytic activity. The main focus is on

the specific technological application of antibacterial agents and disinfection (this choice determines the criteria for choosing suitable dopants). After examining the density of state (DOS) and formation energy of various codoping models in  $\text{TiO}_2$ , ( $\text{V}_{\text{Ti}}\text{-N}_{\text{O}}$ ) is proposed to be the best candidate cation-anion codopant pair for antibacterial agent applications.

## 5.2 Computational Method for Defects Calculations

Density functional theory (DFT) under the local density approximation (LDA) and projector augmented wave (PAW) (Blöchl, 1994), as implemented in the VASP codes (Kresse and Furthmüller, 1996a) are generally used to obtain the results in this chapter. In order to investigate the realistic defect-level positions of the best candidate, the hybrid functional Heyd-Scuseria-Ernzerhof (HSE06) is applied (Heyd et al., 2003; Heyd et al., 2006; Paier et al., 2006). The exchange potential in the HSE06 is divided into short- and long-range parts. In the short-range part, Hartree-Fock (HF) exchange is mixed with Perdew-Burke-Ernzerhof (PBE) exchange (Becke, 1993a; Becke, 1993b; Perdew et al., 1996). To avoid the tremendously expensive calculation of long-range HF exchange, which would render the calculations impossible for solid crystals, the long-range PBE exchange is used to replace this term. A plane-wave basis set with the cutoff energy of 400 eV is employed. The LDA-calculated crystal parameters of bulk anatase- $\text{TiO}_2$  are  $a = 3.764 \text{ \AA}$ ,  $c/a = 2.488$ , and  $u = 0.208$ . These values are in good agreement with the experimental values of  $a = 3.785 \text{ \AA}$ ,  $c/a = 2.513$ , and  $u = 0.208$  (Howard et al., 1991) and other calculations (Fahmi et al., 1993; Asahi et al., 2000; Calatayud et al., 2001). To calculate the formation energy of defects, a supercell approach is used (Zhang and Northrup, 1991; Northrup and Zhang, 1994; Zhang et al., 2001). In the calculations, all atoms are allowed to relax

by minimization of the Hellmann-Feynman force to less than 0.05 eV/Å. Our preliminary study is based on a supercell containing 48 atoms, a  $2 \times 2 \times 2$  repetition of the primitive anatase unit cell. To ensure the convergence of the calculations, all the calculations are repeated with a larger supercell containing 96 atoms, a  $4 \times 2 \times 2$  repetition of the primitive anatase unit cell. It is found that formation energies calculated using the 48-atom cell are in agreement with those calculated using the 96-atom cell to within 0.4 eV. For the Brillouin zone integrations, a shifted  $2 \times 2 \times 2$  Monkhorst-Pack special  $k$ -point mesh (Monkhorst and Pack, 1976) is used (for both supercell sizes). All numerical results presented in this work are based on the 96-atom cell calculations except for the HSE06 calculations where the 48-atom cell is used. Our calculated LDA band gap is 2.48 eV which suffers from the well known DFT underestimation but is in agreement with the other calculations (Na-Phattalung et al., 2006; Ma et al., 2010). Our HSE06 band gap is 3.30 eV, in good agreement with the experimental band gap of 3.23 eV (Tang et al., 1993). HSE calculations allow us to calculate the defect levels without the need to apply band gap corrections.

From a supercell calculation, the formation energy of an impurity  $D$  in charge state  $q$  is defined (Zhang and Northrup, 1991; Northrup and Zhang, 1994), as

$$E^f[D^q] = E_{tot}[D^q] - E_{tot}[\text{TiO}_2, \text{bulk}] + \sum_x \Delta n_x \mu_x + q(E_F + E_V), \quad (5.1)$$

where  $E_{tot}[D^q]$  is the total energy of a supercell containing defect  $D$  in charge state  $q$  from the calculation,  $E_{tot}[\text{TiO}_2, \text{bulk}]$  is the energy of the defect-free supercell,  $\Delta n_X$  is the number of atom specie  $X$  being remove (positive) or add (negative) to the supercell to create the defect cell,  $\mu_X$  is the chemical potential of atoms specie

$X$ ,  $E_F$  and  $E_V$  are the electron Fermi energy and the position of the valence band maximum, respectively. To remedy the band gap problems (for LDA calculations), the valence band maximum at the special  $k$  points is averaged for  $E_V$ .

During the equilibrium growth, if any chemical potential rises above its natural phase value (i.e., that of metal Ti, O<sub>2</sub>, metal V, and *etc*), then the natural phase would form as an inclusion. These set the upper limit of the possible chemical potential for each element. In order for TiO<sub>2</sub>, to grow in equilibrium, it is also required that

$$\mu_{\text{TiO}_2} = \mu_{\text{Ti}} + 2\mu_{\text{O}}, \quad (5.2)$$

where  $\mu_{\text{TiO}_2}$  is the heat of formation of a molecular formula of TiO<sub>2</sub> (-10.10 eV, calculated value). All chemical potentials are referenced to their natural phases. Additional limitations on the chemical potentials are imposed by the formation of alternative phases containing Ti and O such as TiO (Na-Phattalung et al., 2006).

### 5.3 Results and Discussions

The band gap narrowing has an upside regarding the ability to absorb photons in the visible light region which allows the utilization of sun light more effectively. However, it also weakens the redox potential of TiO<sub>2</sub> and increases the recombination rate of photoexcited carriers. The reduction of the electron (or hole) redox potential causes a decrease in the production of major oxidizing species, namely reactive oxygen species (ROS) that can act as antibacterial agents. Therefore, it is important to carefully manage these factors (balancing between the reduction of the band gap and the weakening of the redox potential) to reach the best photocatalytic activity. This mainly involves the choices of codopants

for the desired application. Therefore, in this work the type of doping element and the desired lattice location are examined in detail to facilitate the design of the doping mechanism that could provide the desired energy levels. The desired energy levels depend on the semiconductor-interface reaction of reactive oxygen species (ROS) as well as their redox potentials on  $\text{TiO}_2$  surface as discussed below.

### 5.3.1 Redox Potentials of Major Reactions on Semiconductor-solution Interface

Figure 5.1 illustrates redox potentials of major species for photocatalyst disinfection and antibacterial agents compared to that for water splitting. The redox potential of the oxidizing species are compared against the potential of the standard hydrogen electron (SHE) at  $\text{pH} = 7$  (Fujishima, 2000). The higher negative potential provides higher reducing power whereas the higher positive potential provides higher oxidizing power. In the other words, the higher the CBM energy, the stronger the reducing reducing power, whereas the lower the VBM energy, the higher the oxidizing power. Therefore, high positive potential and high negative potential of oxidizing species are preferred. However, to reach higher solar absorption, it is necessary to lower the band gap of  $\text{TiO}_2$  which would weaken the redox potential of either the hole or the electron (or both) in the bulk.

To maintain the reaction, the redox potentials should not be weaker than that of the surface-reaction potentials, as displayed in Figure 5.1. As a result, the defect levels (which would define the new band edges) should be induced in the regions between the band edges and the desired reactions. As shown in Figure 5.1, the potential of hole is  $+2.53$  eV, whereas the electron potential is  $-0.52$  eV (with respect to SHE) (Fujishima, 2000). Holes have much higher redox potential than that of electron, making it more reactive. It reacts with hydroxyl ion

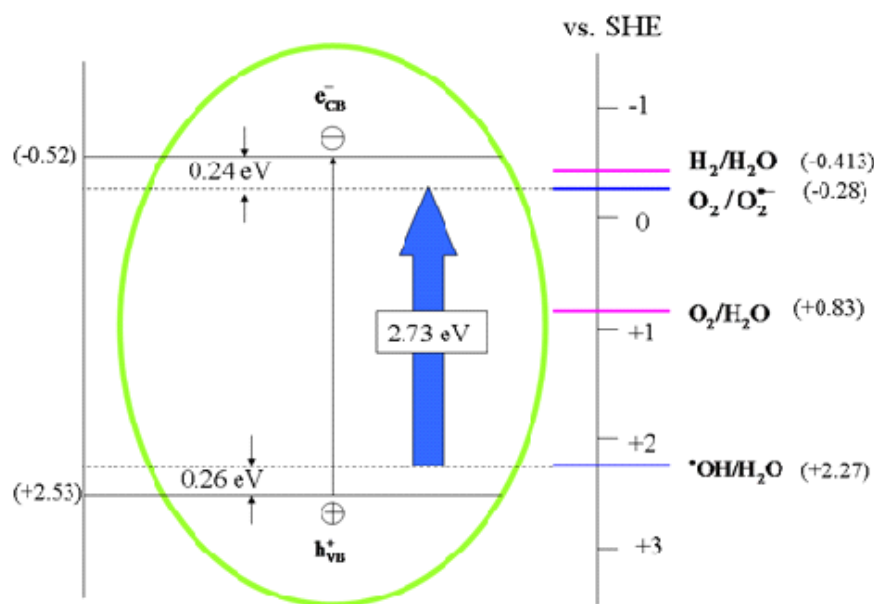


**Figure 5.1** Potentials for redox processes occurring at anatase-TiO<sub>2</sub> surface at pH = 7.

OH<sup>-</sup> or water H<sub>2</sub>O (depending on the pH) on the TiO<sub>2</sub> surface and gives hydroxyl radical •OH(+2.27 eV) as a product. On the other hand, oxygen molecule O<sub>2</sub> is the main electron scavenger to prevent the electron-hole recombination. O<sub>2</sub> traps photoelectron and turns into superoxide anion O<sub>2</sub><sup>•-</sup> (-0.28 eV). Both •OH and O<sub>2</sub><sup>•-</sup> play important roles in the photocatalytic reaction mechanism. To maintain the creation of •OH and O<sub>2</sub><sup>•-</sup>, the new band edge levels should be created within the narrow ranges of 0.26 eV above the VBM and 0.24 eV below the CBM, respectively. Otherwise, the desired surface reactions would be suppressed. The suitable codopants for this work should give defect levels at about 0.24 eV above the VBM and below the CBM which would lead to the total band-gap reduction of about 0.50 eV. The targeted band gap of 2.70 eV would allow significant improvement in generating photoelectrons and photoholes under the solar spectrum.

Recently, a lot of attention has been paid to engineer TiO<sub>2</sub> for water splitting applications, including the modification by codopants (Gai et al., 2009). Gai

et al. suggested that the suitable codopants for water splitting should significantly shift the valence band edge up and leave the conduction band edge almost unchanged. This is consistent with the redox potentials for water splitting (Figure 5.1, pink lines) (Fujishima, 2000; Gai et al., 2009). Unlike water-splitting application, to produce both  $\bullet\text{OH}$  and  $\text{O}_2^{\bullet-}$ , which are important ROSs for antibacterial agent, only the shallow levels (within 0.26 and 0.24 eV, respectively) are allowed on VBM and CBM edges. The deeper level (than 0.26 eV) from the VBM edge would suppress  $\bullet\text{OH}$  productions while the deeper level (than 0.24 eV) from the CBM edge would suppress  $\text{O}_2^{\bullet-}$  productions. In addition, the deeper levels that are not fully occupied (or levels that have been charged by photo-excitation) may act as recombination centers that further decrease the photocatalytic activity. Clearly, the criteria for selecting appropriate dopants for antibacterial agent applications are quite different than those for water-splitting.

### 5.3.2 Monodoping in $\text{TiO}_2$

As a first step before studying the codoping, the monodoping of both O and Ti sites are studied in order to identify the potential elements that could provide the defect levels at the desired position. Here, one should be aware that the levels are likely to shift during codoping due to the pair interactions. Therefore, the numerical value of the defect levels from the monodoping should not yet be taken seriously.

Figure 5.2 shows the total electronic density of states (DOS) and partial density of states (PDOS) of bulk- $\text{TiO}_2$ . The valence bands are composed mainly of O  $2p$  states, whereas the conduction bands show predominant Ti  $3d$  character. Therefore, replacing O and Ti with other elements should directly affect the valence bands and conduction bands, respectively.

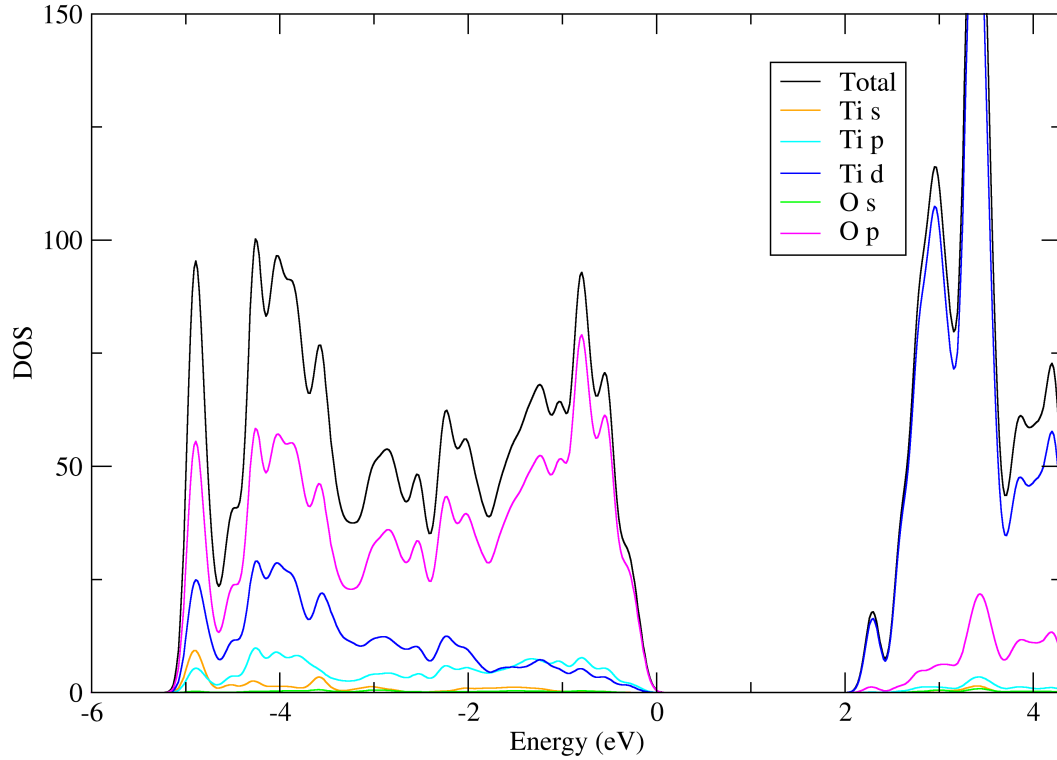


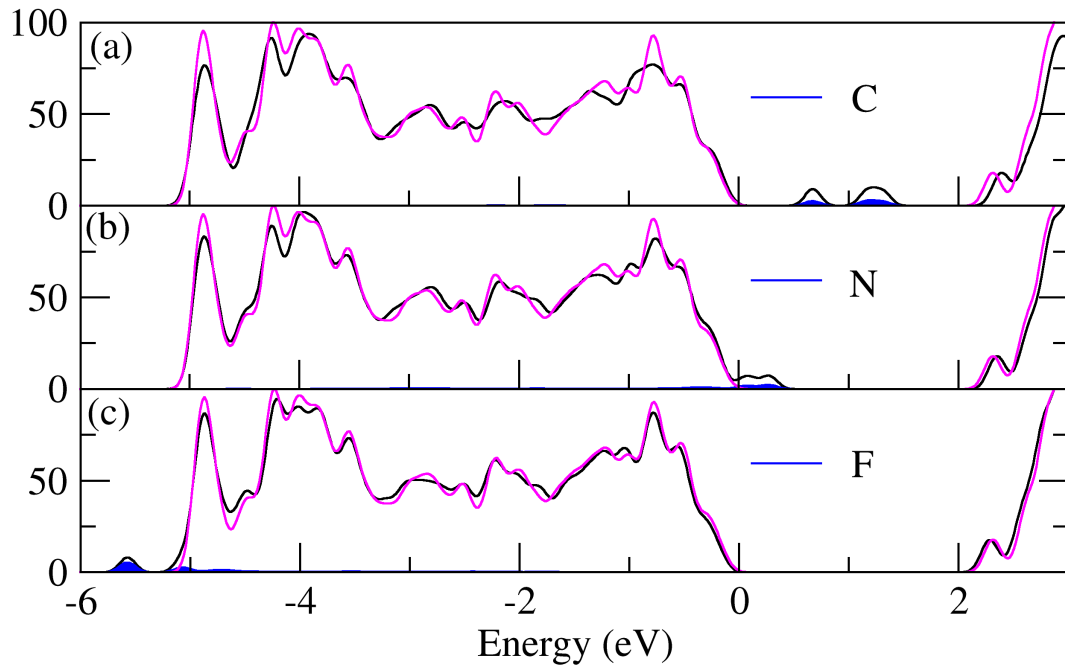
**Figure 5.2** Site decomposed electron density of states (DOS) of total and atom-projected DOS of bulk  $\text{TiO}_2$ . For each atom center, the local partial DOS in a sphere radius  $R$  (Ti:  $R=1.48 \text{ \AA}$  and O:  $R=0.74 \text{ \AA}$ ) is calculated.

In the present work, C, N, S, and F substitutions on the O site ( $\text{C}_\text{O}$ ,  $\text{N}_\text{O}$ , and  $\text{F}_\text{O}$ ) are studied and expected to modify the valence band edge, whereas group-III, -V, and -VI elements substituting on the Ti site [group-III elements: ( $\text{Sc}_\text{Ti}$ ,  $\text{Y}_\text{Ti}$ ,  $\text{Al}_\text{Ti}$ ,  $\text{Ga}_\text{Ti}$ ,  $\text{In}_\text{Ti}$ , and  $\text{Tl}_\text{Ti}$ ), group-V elements: ( $\text{V}_\text{Ti}$ ,  $\text{Nb}_\text{Ti}$ ,  $\text{Ta}_\text{Ti}$ ,  $\text{P}_\text{Ti}$ ,  $\text{As}_\text{Ti}$ , and  $\text{Sb}_\text{Ti}$ ), and group-VI elements: ( $\text{S}_\text{Ti}$ ,  $\text{Se}_\text{Ti}$ ,  $\text{Te}_\text{Ti}$ ,  $\text{Cr}_\text{Ti}$ ,  $\text{Mo}_\text{Ti}$ , and  $\text{W}_\text{Ti}$ )] are expected to modify the conduction band edge.

Figure 5.3 illustrates the calculated DOS of anion-doped  $\text{TiO}_2$ . To align the DOS of different systems, the core levels of the atom farthest from the impurity are selected as the references (Van de Walle et al., 2001).  $\text{C}_\text{O}$  and  $\text{N}_\text{O}$  induce defect levels in the band gap, [as shown in Figure 5.3 (a) and (b)]. The induced states due to C  $2p$  are deep in the band gap and are split into three levels at 0.84,

1.35, and 1.47 eV. The energy levels split as a result of the decrease in the local symmetry. Because CO induces deep states, far from the VBM, which are not appropriate for our purpose, its codopants are not further considered. For N<sub>O</sub>, similar to C<sub>O</sub>, there are also three defect states above the VBM derived from N 2*p*, as shown in Figure 5.3 (b). Although N<sub>O</sub> produces shallower levels compared to those of C<sub>O</sub>, they are still too deep, i.e. about 0.49 eV above the VBM. This may explain why N-doped TiO<sub>2</sub> gives worse photocatalytic activity than that of pure-TiO<sub>2</sub> (Hashimoto et al., 2005). Although, N<sub>O</sub> by itself may not be a good choice to enhance the photocatalytic activity of TiO<sub>2</sub>, its levels could potentially be reduced down to the desired value by codoping. Therefore, N-codopants are further studied. For F-doped TiO<sub>2</sub>, there are no defect states in the band gap as shown in Figure 5.3 (c) because the F levels are very low compared to TiO<sub>2</sub> VBM.

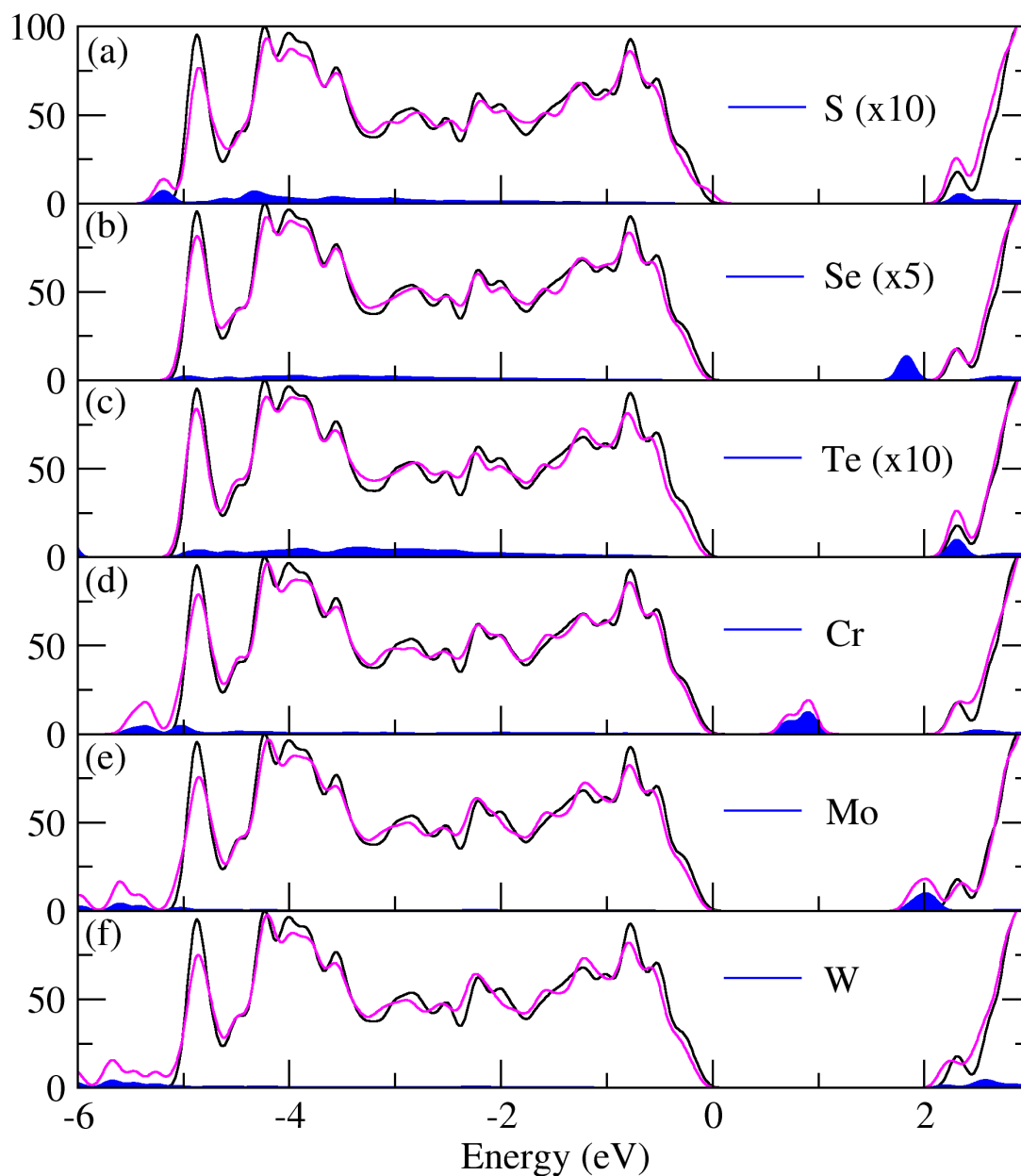
Figure 5.4 shows the calculated DOS of TiO<sub>2</sub> doped by group-VIA and group-VIB on the Ti site. As expected, substitutions of Ti by these elements affect the CBM of TiO<sub>2</sub>. For group-VIA elements, as shown in Figure 5.4 (a)-(c), Se induces deep levels in the band gap, whereas S and Te do not produce any defect level. For group-VIB elements (Cr, Mo, and W), Cr produces mid gap states, while Mo and W give shallow levels as shown in Figure 5.4 (d)-(f). Because Mo and W show shallow states below the CBM, both elements are potentially suitable for our purpose. However, these group-VI elements that are isovalent to the O require its pair to be isovalent to the Ti in order to keep the electron counting such that all valence states are occupied and conduction states are empty. Carbon (isovalent to Ti), which is the best choice to bind with these elements as their passivated codopant, is not suitable for our purpose because of its deep states. Therefore, the C-codopants (C binds with group-VI elements) are not further considered in



**Figure 5.3** Site decomposed electron density of states (DOS) for monodoped  $\text{TiO}_2$  (anions) where (a)  $\text{C}_\text{O}$ , (b)  $\text{N}_\text{O}$ , and (c)  $\text{F}_\text{O}$  in  $\text{TiO}_2$  (magenta), compared with undoped  $\text{TiO}_2$  (black). The shaded area refers the PDOS for impurity atoms.

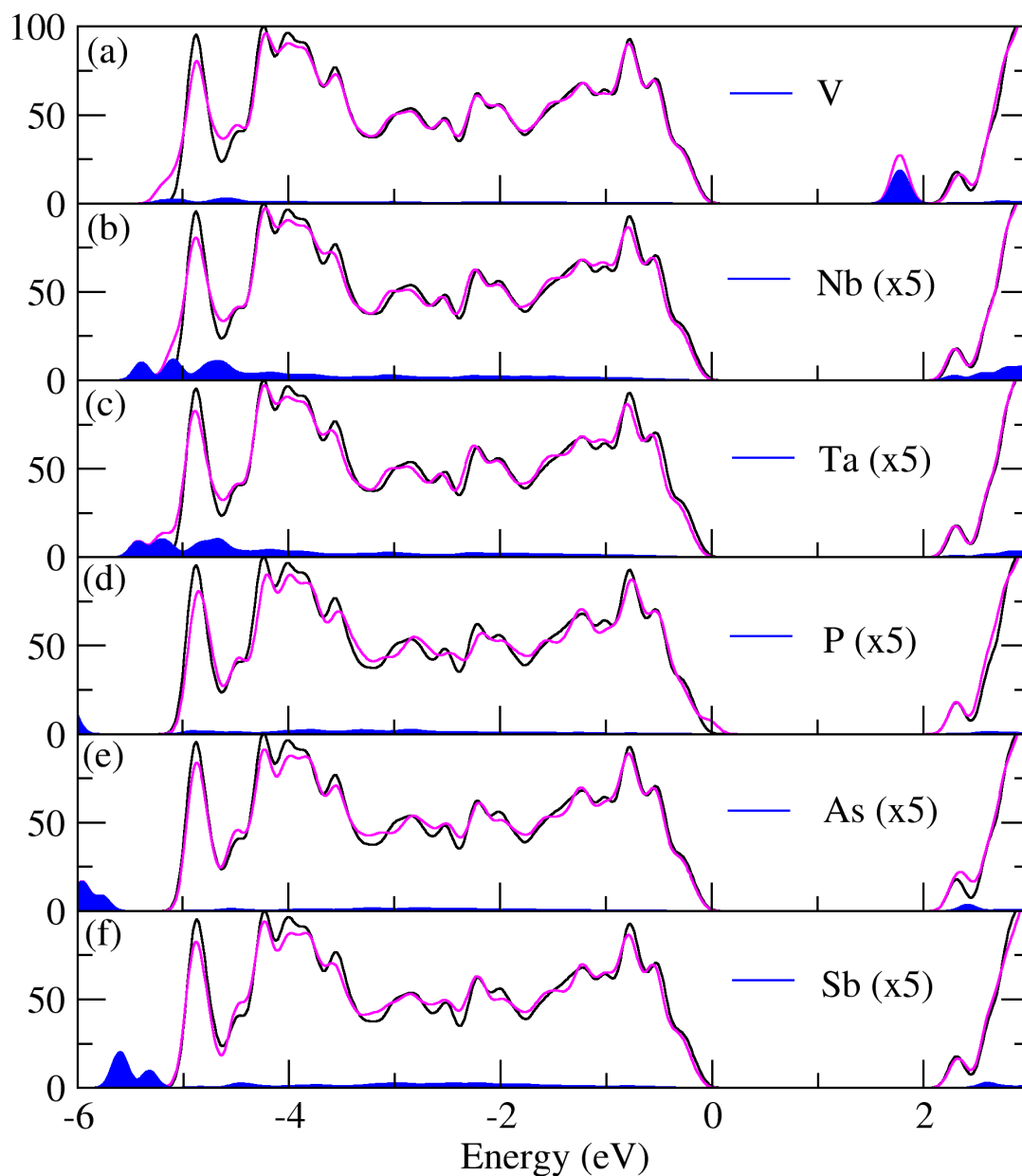
detail.

Figure 5.5 suggests that, among group-V elements, vanadium is the only element which can induce defect states below the CBM. The three defect states are derived from  $T_{2g}$  states of V  $3d$ . Although, these levels are rather deep, i.e., about 0.54 eV, they could shift to the shallower side when the codopant is formed. Therefore, vanadium-codopants are further studied. Another element, which may induce defect levels inside the band gap when it participates as a codopant, is niobium (Nb). The defect levels induced by Nb make contributions in the CBM. These states may shift down below the CBM when NbTi participates as a codopant. Other elements (in this case: Ta, P, As, and Sb), when substituting for Ti, give defect levels that lie well below the VB (as presented in Figure 5.5) making them unsuitable to produce levels near the CBM.



**Figure 5.4** Site decomposed electron density of states (DOS) for monodoped  $\text{TiO}_2$  by group-VI elements (anions).

For group-III substitution for Ti, none of the studied elements induced the defect levels in the band gap, as shown in Figure 5.6. However,  $\text{Tl}_{\text{Ti}}$  significantly shifts the VBM upward and might be a good candidate for modifying the VBM (as opposed to the CBM we originally expect it to modify). Therefore, we further studied their codopants with V and Nb that may be suitable for our purpose.



**Figure 5.5** Site decomposed electron density of states (DOS) for monodiploid  $\text{TiO}_2$  by group-V elements (cations).

Cobalt has been reported experimentally that it can modify the band gap and catalytic activity of  $\text{TiO}_2$ . Therefore, we include the study of cobalt impurity in this thesis. The DOS of  $\text{Co}_{\text{Ti}}$  is shown along with the site decomposed DOS on the Co atom in Figure 5.7.

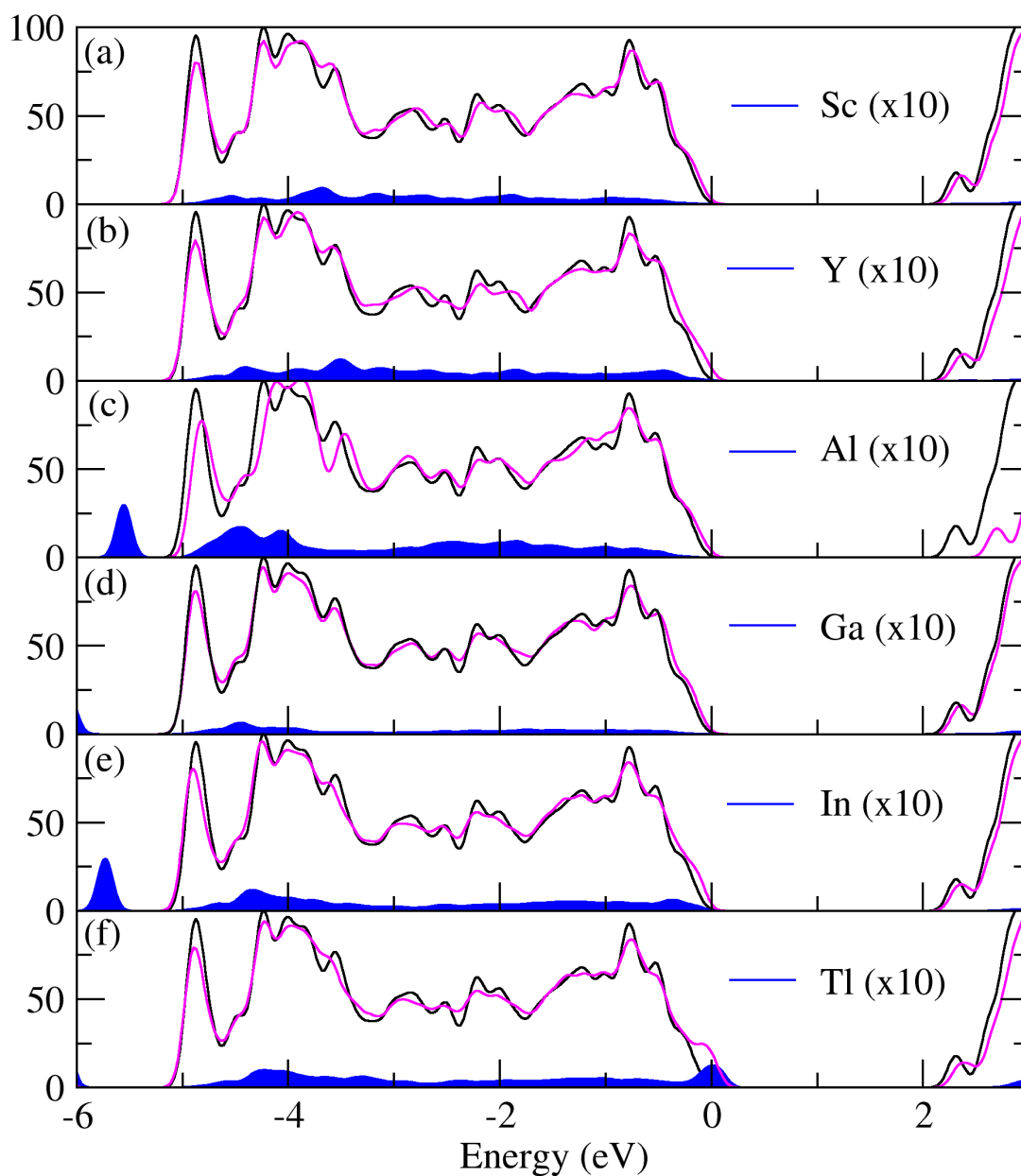


**Figure 5.6** Site decomposed electron density of states (DOS) for monodoped  $\text{TiO}_2$  by group-III elements (cations).

### 5.3.3 Passivated Codoping in $\text{TiO}_2$

Because monodoping generally introduces partially occupied defect states that act as the recombination centers, it can compromise photocatalytic efficiency. To avoid this problem, one may dope  $\text{TiO}_2$  with charge compensated

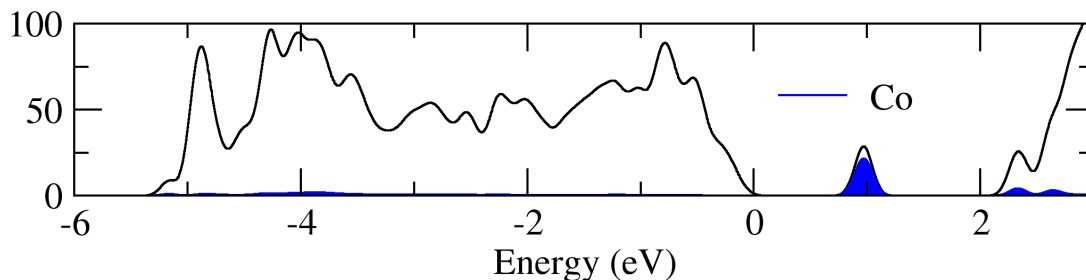


**Figure 5.7** Site decomposed electron density of states (DOS) for  $\text{Co}_{\text{Ti}}$  compared with undoped  $\text{TiO}_2$  (black).

donor-acceptor pairs to preserve the electron counting. For example, to provide a compensated pair for  $\text{N}_{\text{O}}$ , which is a single acceptor, one may co-dope it with a group V dopant such as  $\text{V}_{\text{Ti}}$  or  $\text{Nb}_{\text{Ti}}$ , which is a single donor. The Coulomb attraction between the donor and acceptor, i.e.,  $\text{N}_{\text{O}}-\text{V}_{\text{Ti}}$  and  $\text{N}_{\text{O}}-\text{Nb}_{\text{Ti}}$ , should lower the formation energy and help stabilize the complex. Although codoping by substituting cations and anions allows the donor-acceptor pairs to form with the minimum separation (hence, gaining the largest Coulombic attraction), in practice, it could be difficult to find the growth conditions that favor both cation and anion substitutions. Therefore, codopings on the cation site alone such as  $\text{In}_{\text{Ti}}-\text{V}_{\text{Ti}}$  or anion site alone such as  $\text{N}_{\text{O}}-\text{F}_{\text{O}}$  could be beneficial for the ease of doping process.

### 5.3.3.1 Substituting Sites and Defect Locations

The sites for codoping pairs can be grouped into three types, i.e., the cation-cation ( $\text{X}_{\text{Ti}}-\text{Y}_{\text{Ti}}$ ) pair, cation-anion ( $\text{X}_{\text{Ti}}-\text{Y}_{\text{O}}$ ) pair, and anion-anion ( $\text{X}_{\text{O}}-\text{Y}_{\text{O}}$ ) pair, as illustrated more than one inequivalent pair for each type. For the case of cation-cation codopant ( $\text{X}_{\text{Ti}}-\text{Y}_{\text{Ti}}$ ) and cation-anion codopant ( $\text{X}_{\text{Ti}}-\text{Y}_{\text{O}}$ ) pairs, there are two inequivalent pairs for each, named near site and far site. For the case of anion-anion ( $\text{X}_{\text{O}}-\text{Y}_{\text{O}}$ ) pair, there are three inequivalent pairs, named near site, middle site, and far site, as shown in Figure 5.8. Because the near sites allow the donor-

acceptor pairs to form at the closest proximity compare to other sites of the same type, the near site always give the lowest energy. The only exception observed is the case of ( $N_O-F_O$ ) which has an exceptional electron occupation property due to the unusually deep level of  $F_O$ . While the expected role of group-VII F when substitution for group-VI O is a donor, the electronegativity of F is so strong such that it behaves as an acceptor. Therefore, the  $N_O-F_O$  complex is a donor-donor pair, leading to a repulsion force between N and F instead of an attractive force.

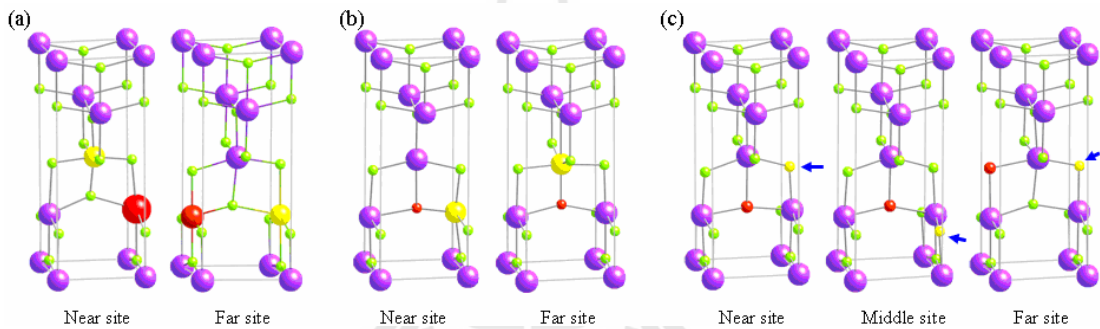


**Figure 5.8** Atomic structure of codopants in  $TiO_2$  by cation-cation, cation-anion, and anion-anion.

### 5.3.3.2 Density of States and Defect Levels

Figure 5.9 shows the DOS and partial density of states (decomposed by projecting the DOS on the atoms of interest) of several codoping pairs with  $N_O$ . In the first three cases (the first three plots), the  $N_O$  successfully introduced a level slightly above the VBM as expected. This can be seen from the partial density of  $N_O$  (green shaded area). The N states induced by  $N_O$  in the ( $V_{Ti}-N_O$ ), ( $Nb_{Ti}-N_O$ ), and ( $Ta_{Ti}-N_O$ ) pairs are at 0.27, 0.27, and 0.34 eV, respectively, above the VBM. However, the only defect pair that successfully introduces another state slightly below the CBM is ( $V_{Ti}-N_O$ ). For ( $V_{Ti}-N_O$ ), the partial density of states of V (blue shaded area) shows a defect levels below the CBM by about 0.13 eV, in

the numerical values of other pairs and states can be found in Figure 5.9. Note that, this 0.13 eV state induced by the V atom in ( $V_{Ti}$ - $N_O$ ) is shallower than that induced by V-monodoping. Because ( $V_{Ti}$ - $N_O$ ) induces both shallow acceptor states above the VBM and shallow donor states below the CBM, it is a potential candidate for our proposed application. This is consistent with previous theoretical studies (Ma et al., 2010; Zhao and Liu, 2008). Other three remaining codopants studied, i.e., ( $P_{Ti}$ - $N_O$ ), ( $As_{Ti}$ - $N_O$ ), and ( $F_O$ - $N_O$ ), give deep acceptor levels which are 1.30, 0.67, and 0.47 eV from the VBM, respectively. Therefore, they are not good candidates.

$V_{Ti}$ ,  $N_O$ , and ( $V_{Ti}$ - $N_O$ ) are the best candidates for the  $n$ -type dopant, the  $p$ -type dopant, and the codopant, respectively, because each meets our required conditions.

**Table 5.1** The calculated  $\Delta E_v$ ,  $\Delta E_c$ ,  $\Delta E_g$ , and binding energy ( $E^b$ ) for anatase- $TiO_2$  doped with N-codopants.

Codopants	$\Delta E_v$	$\Delta E_c$	$\Delta E_g$	$E^b$ (eV)
( $V_{Ti}$ - $N_O$ )	0.27 (0.38)	-0.13 (-0.11)	-0.39 (-0.49)	0.77
( $Nb_{Ti}$ - $N_O$ )	0.27 (0.42)	0.02 (0.05)	-0.25 (-0.37)	0.19
( $Ta_{Ti}$ - $N_O$ )	0.34	0.03	-0.31	0.05
( $P_{Ti}$ - $N_O$ )	1.22	-0.10	-1.32	0.69
( $As_{Ti}$ - $N_O$ )	0.65	-0.15	-0.80	3.07
( $F_O$ - $N_O$ )	0.43	0.06	-0.37	0.31

Therefore, we explored these defects in more detail. The DOS and PDOS of them are plotted in Figure 5.12. For a clear visualization, the smearing width for the plots is reduced. For V-doping, impurity states which have the  $T_{2g}$  symmetry are induced below the CBM. The lowest donor state is located at 0.54 eV below the CBM, as shown in Figure 5.12 (a). The band gap of V-doped  $TiO_2$  is reduced to 1.94 eV compared to the LDA band gap of undoped- $TiO_2$  of 2.47 eV. Electrons

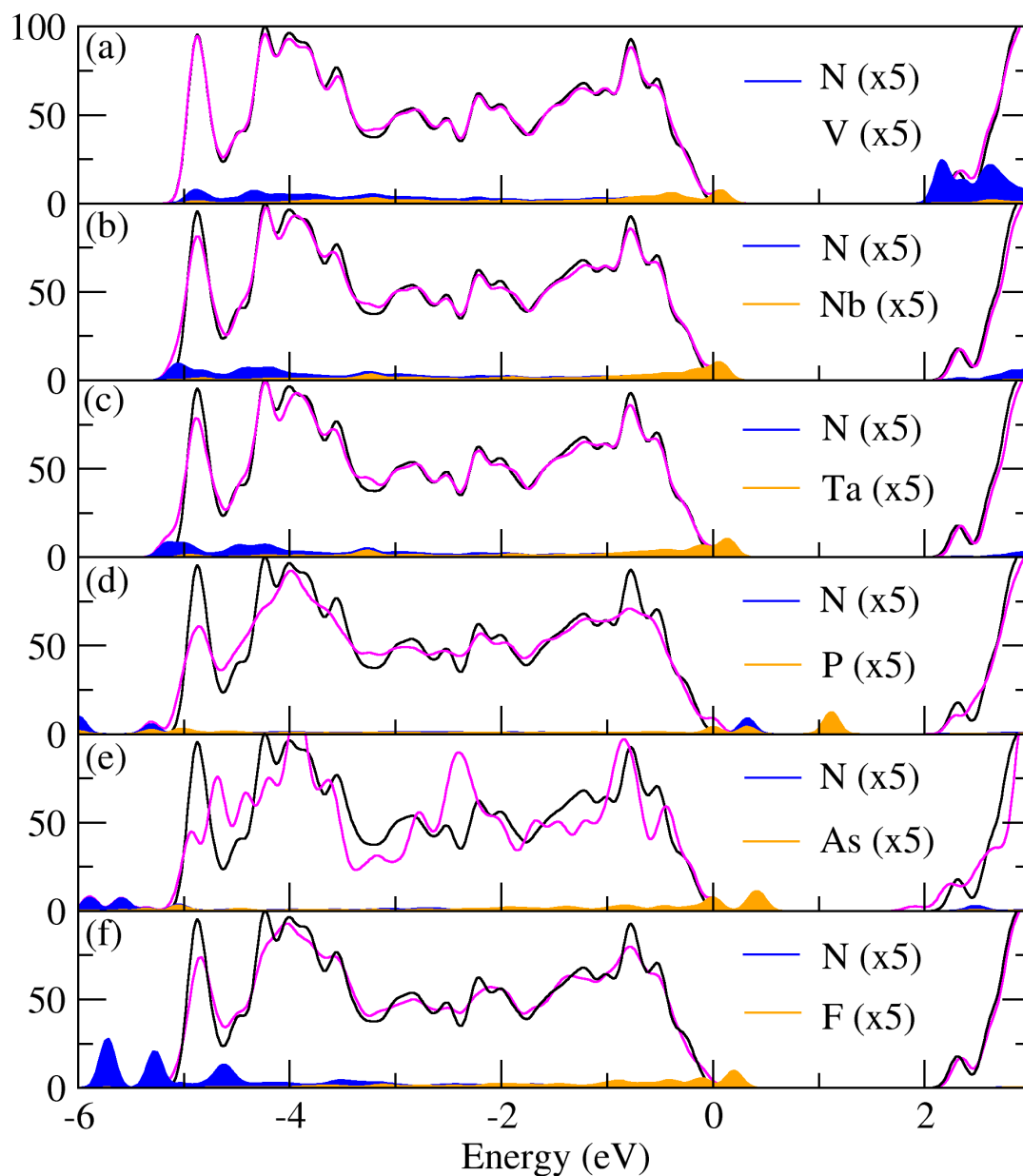


**Figure 5.9** Site decomposed electron density of states (DOS) of N-codopants.

in the VB can be excited to these deep isolated defect states under visible light and then to the CB. For N-doped  $\text{TiO}_2$ , it is clearly seen in Figure 5.12 (b) that three N  $2p$  states are localized. The highest impurity level is located at 0.49 eV above the VBM and the band gap is shrunk to be 2.02 eV. Although both dopants lead to a significant red shift of the optical absorption, these monodoping

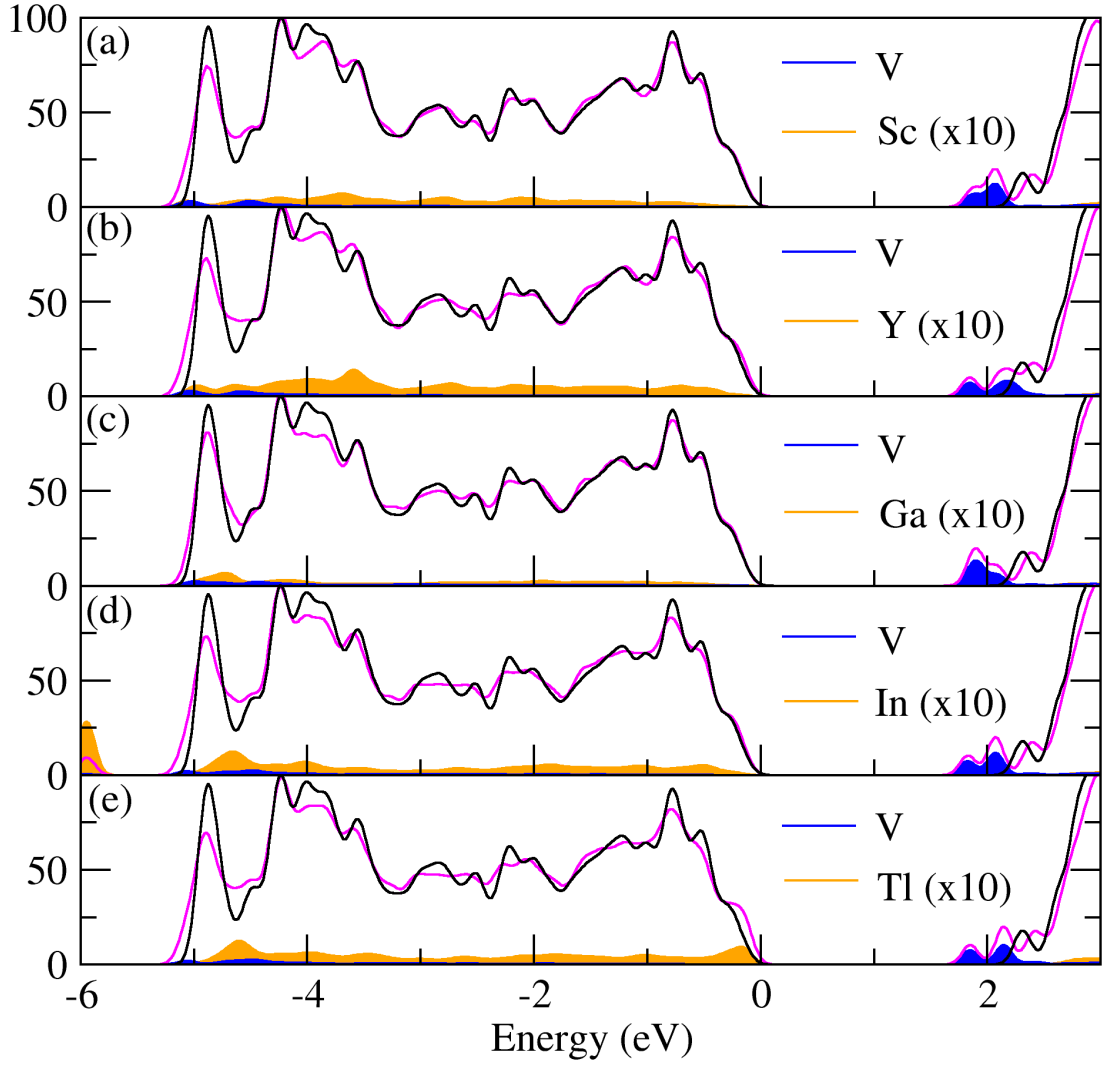


**Figure 5.10** Site decomposed electron density of states (DOS) of V-codopants.

**Table 5.2** The calculated  $\Delta E_v$ ,  $\Delta E_c$ , and  $\Delta E_g$  for anatase-TiO<sub>2</sub> doped with V-codopants.

Codopants	$\Delta E_v$	$\Delta E_c$	$\Delta E_g$
(Sc <sub>Ti</sub> -V <sub>Ti</sub> )	0	-0.42	-0.42
(Y <sub>Ti</sub> -V <sub>Ti</sub> )	0.03	-0.45	-0.48
(Ga <sub>Ti</sub> -V <sub>Ti</sub> )	0.01	-0.41	-0.42
(In <sub>Ti</sub> -V <sub>Ti</sub> )	0.03	-0.45	-0.48
(Tl <sub>Ti</sub> -V <sub>Ti</sub> )	0.07	-0.44	-0.51

(by V and N) produces deep partially occupied states and have the levels too deep compared to the targeted redox potential, making them unsuitable for the antibacterial agent applications. On the other hand, for the passivated codopant ( $V_{Ti}-N_O$ ), the acceptor states due to N  $2p$  and the donor states due to the V  $3d$  are located at 0.27 eV above the VBM and 0.13 eV below the CBM, respectively. These levels match well with the targeted values for the redox potentials [donor states: 0.24 eV and acceptor states: 0.26 eV, as shown in Figure 5.12]. Ma et al. (Ma et al., 2010) attributed the cause of the shallower states in the codoping compared to those of the monodoping to the strong covalence bond of V-N. The shallower state near the VBM also promotes the mixing of the N  $2p$  and O  $2p$  states in the VB which can enhance the lifetimes of charge carriers (Tang and Ye, 2005; Ma et al., 2010). On the conduction band side, the positions of the V  $3d$  are also shifted closer to the CBM which increases the combination of the V  $3d$  and Ti  $3d$  in the CB. Since both acceptor states and donor states are shallower than their monodoping cases, the band gap reduction is 0.39 eV compared to pure  $TiO_2$ . Although, this band gap reduction is less than the targeted value of 0.5 eV, it should provide significant improvement in the solar absorption. The present calculations are in good agreement with previous study as shown in Table 5.3. Because the ( $V_{Ti}-N_O$ ) codopant pair induces the shallow acceptor states and donor states near the targeted values, it is the best candidate to be applied for antibacterial applications.

Because the LDA band gap is highly underestimated, it is not clear how band gap corrections would affect the defect levels. In order to confirm that the qualitative defect locations are still the same the electronic structures are calculated again by HSE06 which is generally provides the band gaps close to the experimental values. The DOS calculated by using HSE06 for the  $V_{Ti}$ ,  $N_O$ , and

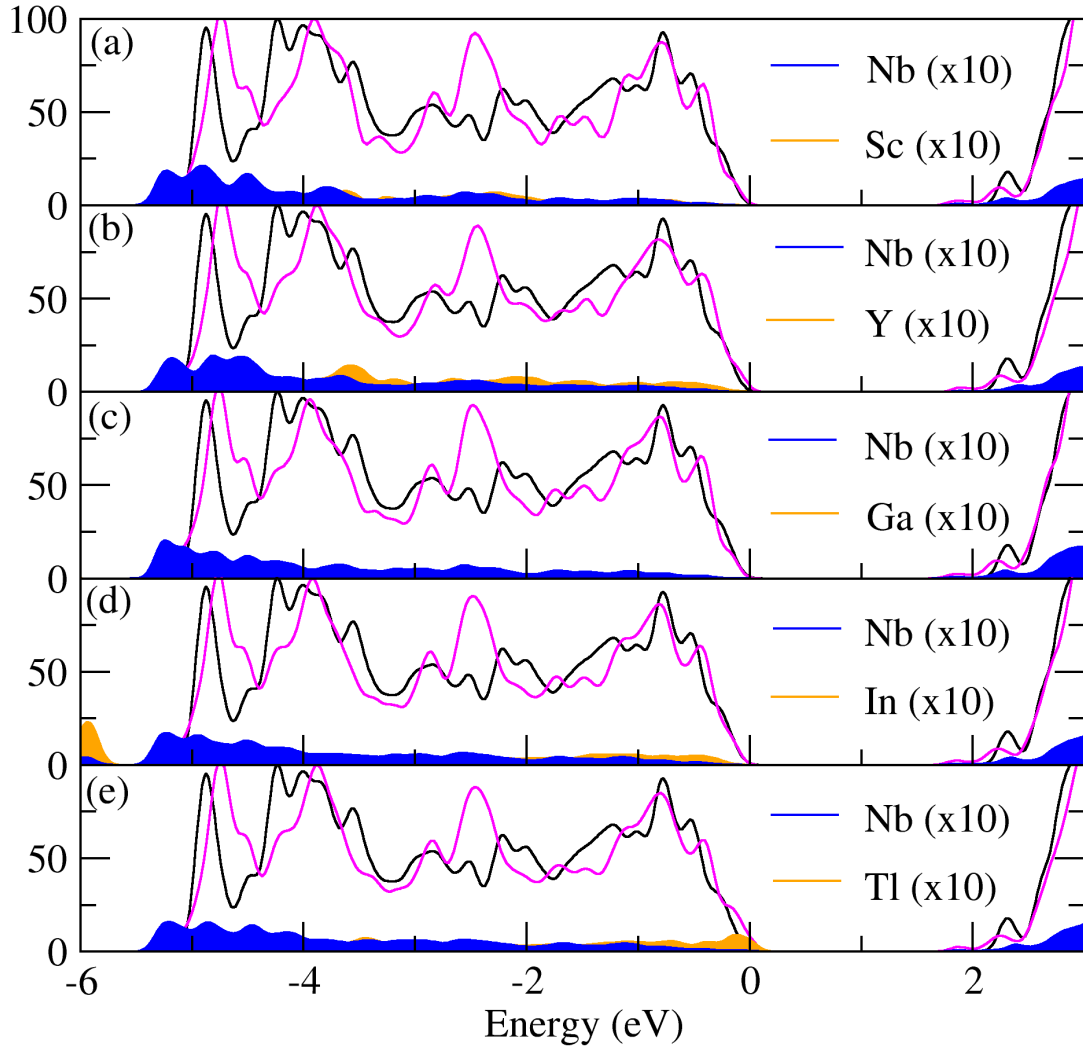


**Figure 5.11** Site decomposed electron density of states (DOS) of Nb-codopants.

**Table 5.3** The calculated  $\Delta E_v$ ,  $\Delta E_c$ ,  $\Delta E_g$ , and formation energy ( $E^f$ ) for anatase- $\text{TiO}_2$  doped with  $\text{N}_\text{O}$ ,  $\text{V}_\text{Ti}$ , and  $(\text{V}_\text{Ti}-\text{N}_\text{O})$ .

Impurity	$\Delta E_v$	$\Delta E_c$	$\Delta E_g$	$E^f$ (eV)	
				Ti-rich	O-rich
$\text{V}_\text{Ti}$	-0.01	0.54	-0.53 (-0.52)	-0.89 (0.32)	- 8.16 (-9.98)
$\text{N}_\text{O}$	0.49	0.04	-0.45 (-0.35)	0.85 (0.04)	4.48 (5.18)
$(\text{V}_\text{Ti}-\text{N}_\text{O})$	0.27 (0.38)	-0.13 (-0.11)	-0.39 (-0.49)	-0.79 (-1.96)	-4.42 (-7.11)

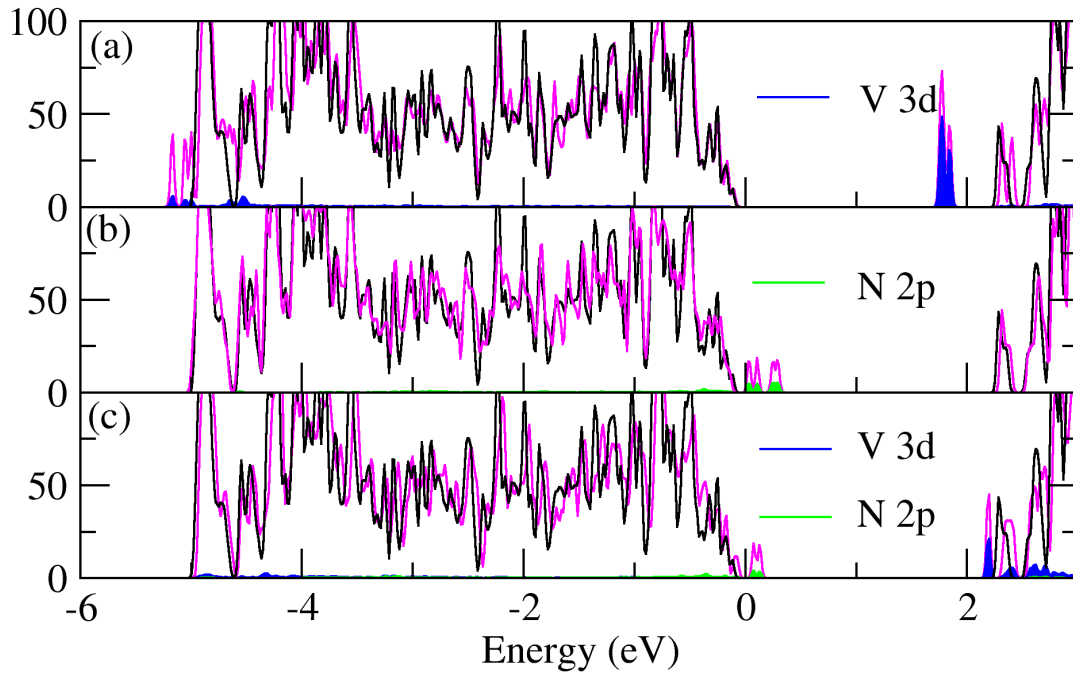


**Figure 5.12** Site decomposed electron density of states (DOS) of  $V_{Ti}$ ,  $N_O$ , ( $V_{Ti}-N_O$ ) in  $TiO_2$ , compared with undoped  $TiO_2$ .

( $V_{Ti}-N_O$ ) are shown in Figure 5.13. For  $V_{Ti}$ , there are three defect levels which are localized below the CBM due to  $V 3d$  [Figure 5.13(a)]. Other  $V 3d$  orbitals are high up in the conduction band. For  $N_O$ ,  $N 2p$  induces three states above the VBM composing of a shallow level near the VBM and two deeper levels [Figure 5.13(b)]. These deep levels are much deeper than those calculated using LDA. For the ( $V_{Ti}-N_O$ ) pair, the defect levels both from  $V_{Ti}$  and  $N_O$  are shallower than those of their isolated defects [Figure 5.13(c)] which is consistent with what has been observed using LDA.

### 5.3.3.3 Binding Energy

To determine if a complex is stable, the binding energy of a complex (Van de

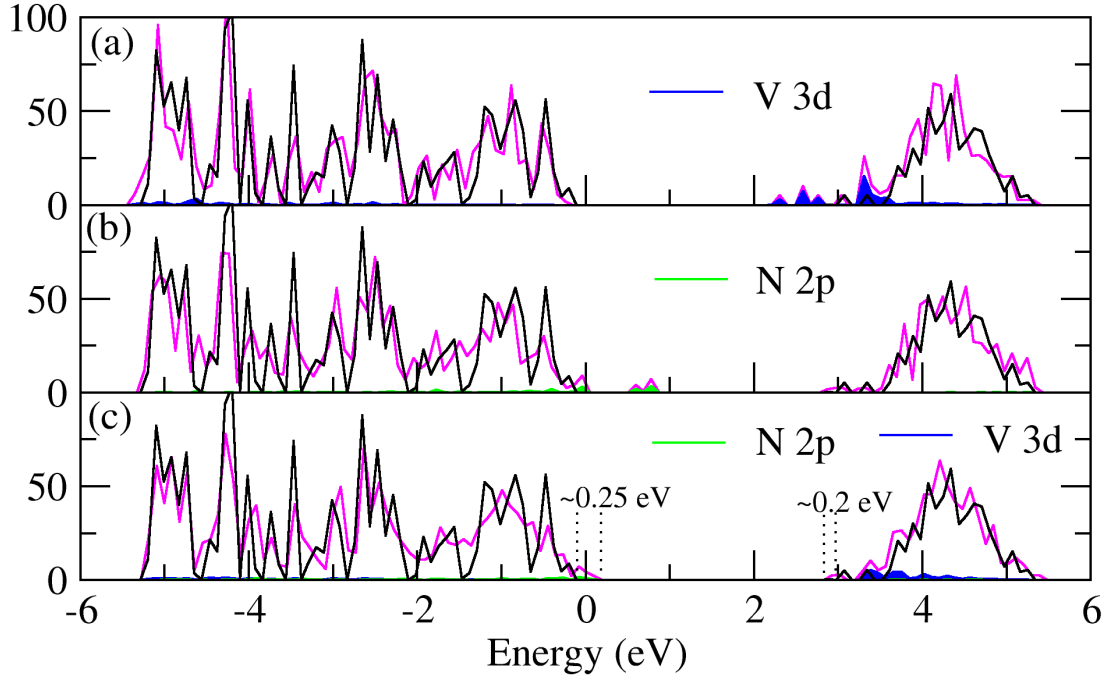


**Figure 5.13** Site decomposed electron density of states (DOS) by HSE06 of  $V_{Ti}$ ,  $N_O$ , and  $(V_{Ti}-N_O)$  in  $TiO_2$ , compared with undoped  $TiO_2$ .

Walle and Neugebauer, 2004) can be calculated as

$$E^b = E^f(A) + E^f(B) - E^f(AB), \quad (5.3)$$

where  $E^f(A)$ ,  $E^f(B)$ , and  $E^f(AB)$  are the formation energies of defects  $A$ ,  $B$ , and a complex defect  $AB$ , respectively. A positive binding energy indicates that the complex is bound. As summarized in Table 5.1, the calculated binding energies for  $(V_{Ti}-N_O)$ ,  $(Nb_{Ti}-N_O)$ , and  $(Ta_{Ti}-N_O)$  are 0.77, 0.19, and 0.05 eV, respectively (assuming the electron Fermi energy at the VBM). The low binding energies of  $(Nb_{Ti}-N_O)$ , and  $(Ta_{Ti}-N_O)$  indicate that these codopants are bound but only weakly so. Therefore, both of them are unlikely or difficult to form. On the other hand, the strong binding energy of  $(V_{Ti}-N_O)$ , indicates that the pair is bound rather strongly.

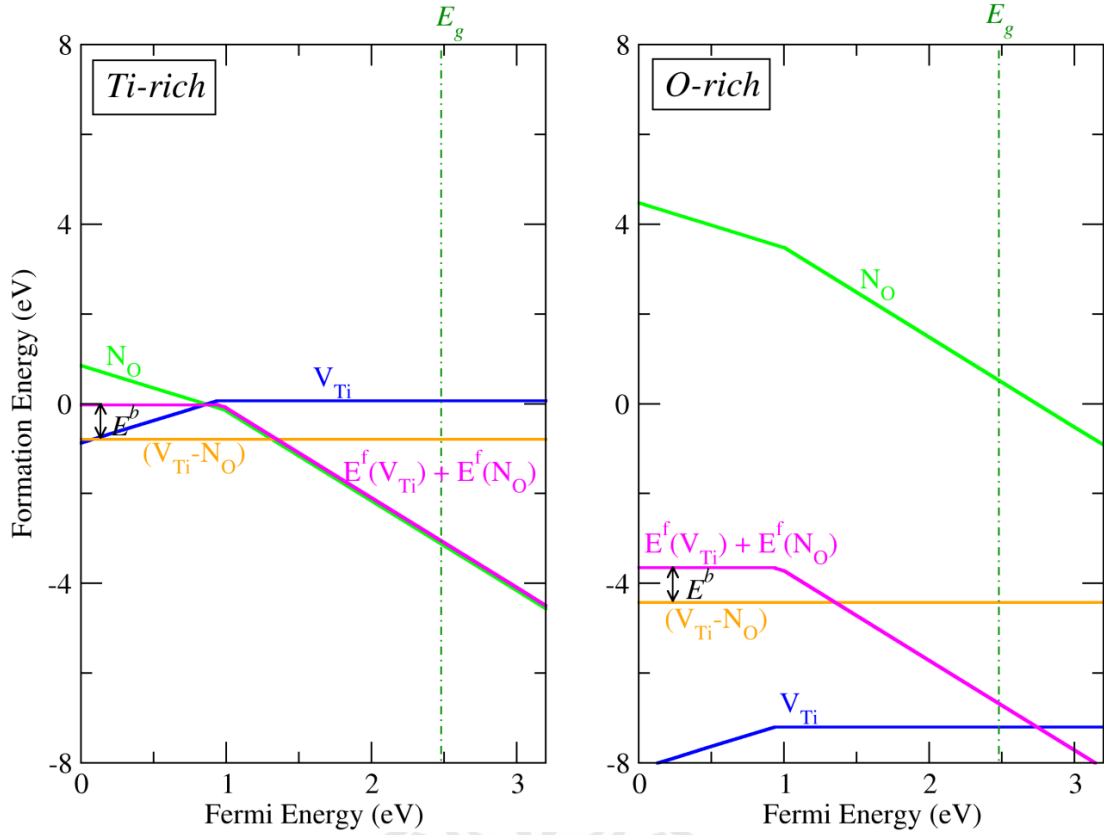


**Figure 5.14** Formation energies and binding energies of  $V_{\text{Ti}}$ ,  $N_{\text{O}}$ ,  $(V_{\text{Ti}}-N_{\text{O}})$  codopants, and its isolated form in  $\text{TiO}_2$  as a function of the Fermi level, under the Ti-rich and O-rich conditions, respectively.

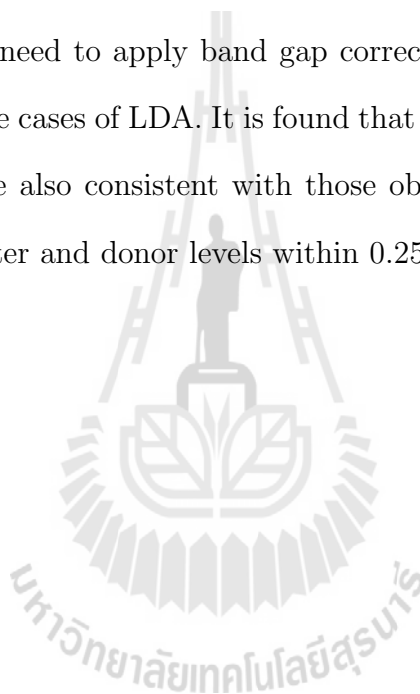
In the process of calculating the binding energy, it is necessary to calculate the formation energy of individual defects as well as the pair. The calculated formation energies of  $V_{\text{Ti}}$  and  $N_{\text{O}}$ , as well as the  $(V_{\text{Ti}}-N_{\text{O}})$  pair are summarized in Table 5.3 and plotted in Figure 5.14. Our values are in a reasonable agreement with Ma et al. (2010), that are also shown in Table 5.3. Figure 5.14 shows the formation energies under two extreme growth conditions; Ti-rich and O-rich. The binding energy, which is the difference between the combined energy of the two individual defect (magenta line) and the energy of the complex pair (orange line), remains the same in both growth conditions. As shown in Figure 5.14, the binding energy is the highest at 0.77 eV for  $E_f < 0.94$  eV. At higher  $E_f$  the binding energy

is quickly reduced and diminished at  $E_F = 1.35$  eV. Note, however, that the formation energy of each individual defect as well as the complex pair can vary depending on the growth condition. According to our results, the Ti-rich condition can provide all defects with reasonable energy to form and the O-rich condition promotes the formation of  $V_{Ti}$  but suppresses the formation of  $N_O$ . This plot can serve as a guide to help designing experimental doping conditions to balance the creation of both individual defects to form the pair. For example, one would shift toward the O-rich side to suppress  $N_O$  formation and enhance  $V_{Ti}$  formation or one could shift the growth condition toward the Ti-rich side to suppress  $V_{Ti}$  formation and enhance  $N_O$  formation.

## 5.4 Conclusions

Comprehensive first-principles calculations on isolated impurities and impurity pairs in anatase- $TiO_2$  have been performed with the goal to seek out the appropriate passivated codopants that can narrow the band gap of anatase- $TiO_2$  while preserving high photocatalytic activity for antibacterial purposes. From the investigation of the required redox potentials for the antibacterial purposes, it is found that the best passivated codopant pairs should provide the shallow acceptor and donor levels at about 0.25 eV from the VBM and CBM, respectively. In addition, the pairs should have a reasonably large binding energy to ensure that the pair is bound. Various possible defect pair configurations have been investigated and it is found that, for these donor-acceptor pairs, the configurations that provide the closest distance between the two, called “near site configuration” in all cases, is the most stable form. Among sixteen pairs studied, it is found that ( $V_{Ti}$ - $N_O$ ) is the best candidate that gives the acceptor and donor levels close to the targeted redox potentials for the antibacterial agent and disinfection appli-

cations. The complex pair provides the acceptor level about 0.27 eV above the VBM and the donor level at about 0.13 eV below the CBM. This results in the band gap reduction of about 0.4 eV which would significantly improve the solar photocatalytic activity. The ( $V_{\text{Ti-N}_O}$ ) complex pair also has a reasonable binding energy of about 0.7 eV. The electronic structures calculations for the ( $V_{\text{Ti-N}_O}$ ) complex pair is repeated using the HSE06 calculations which can provide a full band gap without the need to apply band gap correction before comparing with the experiments like the cases of LDA. It is found that the levels obtained by using HSE06 calculations are also consistent with those obtained using LDA, i.e., the pair has shallow acceptor and donor levels within 0.25 eV from the edges.



# CHAPTER VI

## FLUORINE IMPURITIES IN ZnO

### 6.1 Introduction

ZnO is of current interest because of its suitable properties for short wavelength optoelectronic applications in the blue, violet, and ultra-violet regions. This is mainly due to its wide electronic band gap of 3.3 eV and the availability of bulk crystals (Look et al., 2004). ZnO lattice parameters are similar to those of GaN which is currently the workhorse material for blue and UV photonics (Morkoc, 1999; Look et al., 2004). Another major advantage of ZnO is its large exciton binding energy of 60 meV, which is much larger than that of GaN (25 meV). A large exciton binding energy leads to efficient excitonic emission at room temperature or higher. Therefore, a ZnO-based light emitter is expected to be much brighter than those made from GaN (Li et al., 2006). To fabricate optoelectronic devices both high quality *n*- and *p*-type ZnO are necessary. However, a major obstacle is the difficulty of growing *p*-type ZnO.

There are a number of techniques used to grow ZnO. However, most of them give rise to unintentional *n*-type ZnO. High level *n*-type ZnO can be utilized in various applications such as transparent conductors. A number of recent research works have been focused on finding a way to reduce the *n*-type background and to achieve high quality *p*-type ZnO via doping. The difficulties can arise from various causes. Some dopants have low solubility in ZnO. Other dopants have rather good solubility but produce deep acceptor levels, leading to a low carrier concentration at working temperature. In addition, ZnO is known to have high level of *n*-

type background from unintentional impurities such as H and its native defects of low formation energies are usually *n*-type, causing the spontaneous formation of compensating defects such as  $V_{\text{O}}$  or  $\text{Zn}_i$  (Zhang, 2002).

Substituting on the Zn site by group I dopants is a potential way to give *p*-type ZnO. Li, Na, and K are predicted by first principles calculations to give acceptor energy levels at 0.09, 0.17, and 0.32 eV, respectively, when substituting on the Zn site (Park et al., 2002). However, experimental attempts to dope ZnO with these elements have not been successful so far. For example, it is now known that Li prefers to incorporate in the interstitial form ( $\text{Li}_i$ ) which is a donor. This is especially true when the sample turns *p*-type, making it a self-compensated dopant (Park et al., 2002). Substituting on the O site by group-V dopants have been tried experimentally despite the first principles predictions that these dopants induce deep levels and would not give rise to *p*-type ZnO. Among group V elements, N is the most promising *p*-type doping candidate owing to its close ionic radius to O ( $R_{\text{N}}$ : 1.68 Å and  $R_{\text{O}}$ : 1.38 Å). However, its defect level is still too deep to provide reasonable carrier concentration.

Many computational studies predicted that  $V_{\text{Zn}}$  by itself is a deep acceptor. However, when  $V_{\text{Zn}}$  binds with high-electronegative elements such as F substituting for O, the acceptor level can get shallower (Yan and Wei, 2008). Therefore, it is important to identify the favorable site of F in ZnO crystal to access the feasibility of  $V_{\text{Zn}}\text{-F}_{\text{O}}$  formation. In addition to  $V_{\text{Zn}}\text{-F}_{\text{O}}$ , selected defect complexes containing F are also explored in this thesis.

In this thesis, the focus is on the site identification of F in ZnO. In collaboration with the experimental group, who characterized the F doped ZnO samples by using the synchrotron X-ray absorption spectroscopy (XAS) technique, the first-principles calculations are used to simulate the XAS spectra for various potential

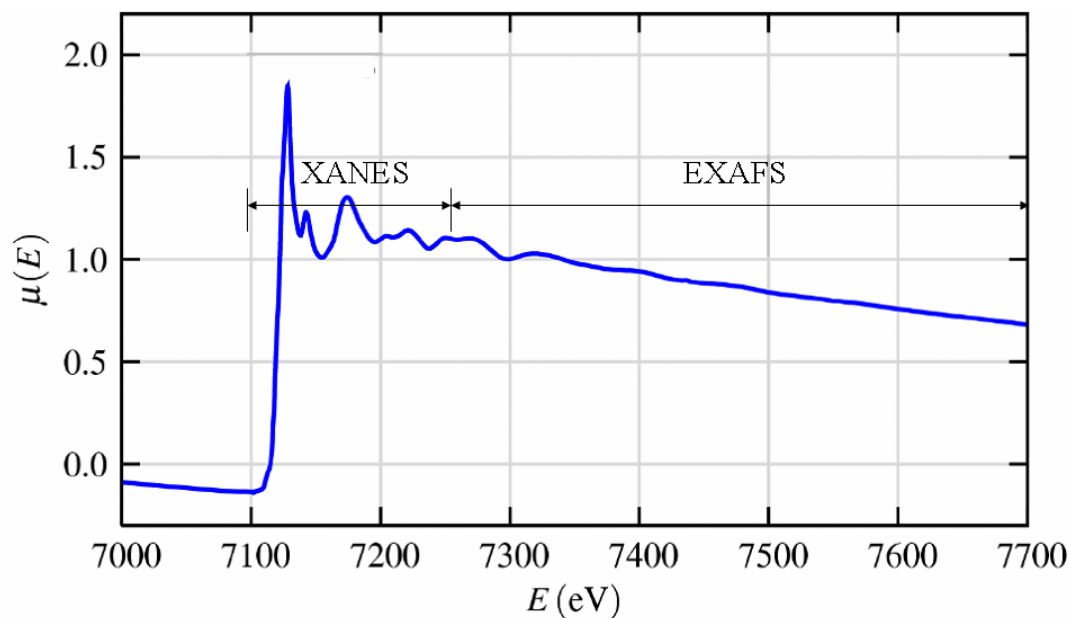


**Figure 6.1** X-ray absorption spectrum for FeO.

configurations of F in order to find the best match with the measurement. XAS spectra are elemental-selective and sensitive to the local structure of the absorbing atom. By choosing the X-ray energy to match the characteristic absorption threshold of a certain element, one can selectively probe the element of interest (in our case, F). Typically, the X-ray absorption spectrum is divided into two regions as shown in Figure 6.1: the near-edge region is the subject of X-ray absorption near-edge spectroscopy (XANES) and the high-energy region is that of the X-ray absorption fine-structure spectroscopy (EXAFS). XANES is sensitive to oxidation state and coordination chemistry of the absorbing atom. EXAFS is reminiscent of electron wave scattering and is mostly used to determine the coordination number, bond lengths, and species of the neighbors of the absorbing atom. Although the X-ray spectra certainly contain detailed information about local electronic and crystal structure, it is difficult in many cases, especially for the XANES region, to extract such information without some prior knowledge of similar systems. For

such cases, first-principles calculations can be used in conjunction with the measurements to interpret the results. This approach has proved itself to be successful in local structure identifications in various systems (Limpijumnong et al., 2006; Limpijumnong et al., 2007; T-Thienprasert et al., 2008; T-Thienprasert et al., 2010).

## 6.2 Computational Method

### 6.2.1 Crystal Structure and Formation Energy

The calculations were based on density functional theory within an orbital-dependent rotationally invariant local density approximation (LDA+ $U$ ). Projector augmented wave (PAW) potentials (Kresse and Joubert, 1999) were used for the electron-ion interactions, as implemented in the VASP code (Kresse and Hafner, 1994; Kresse and Furthmüller, 1996a). The cutoff energy for the plane-wave basis set is 400 eV. For a choice of Coulomb repulsion term  $U$ , we followed Ref. (Janotti and Van de Walle, 2007) which is 4.7 eV. The calculated lattice parameters of wurtzite ZnO are  $a = 3.148 \text{ \AA}$ ,  $c/a = 1.606$ , and  $u = 0.381$  which are in good agreement with the experimental values of  $a = 3.249 \text{ \AA}$ ,  $c/a = 1.602$ , and  $u = 0.381$  (Schulz and Thiemann, 1977) as well as other calculations (Janotti et al., 2006; Panpan et al., 2009). To calculate the formation energies of defects, a supercell approach is used (Northrup and Zhang, 1994; Zhang et al., 2001) with the supercell size of 72 atoms, i.e. a  $3 \times 3 \times 2$  repetition of the primitive wurtzite unit cell. All atoms in the supercell are allowed to relax by minimization of the Hellmann-Feynman force until all forces turned less than  $0.05 \text{ eV/\AA}$ . For the Brillouin zone integration, a  $2 \times 2 \times 2$  Monkhorst-Pack special  $k$ -point mesh is employed. The calculated band gap by LDA+ $U$  is 1.53 eV which is in good agreement with another

theoretical work (Janotti et al., 2006) but much smaller than the experimental band gap (3.3 eV).

The defect formation energies were calculated using the approach described in Chapter III. The upper limits for Zn and O chemical potentials ( $\mu_{\text{Zn}}$  and  $\mu_{\text{O}}$ ) were set by the energies per atom of metallic Zn and  $\text{O}_2$  molecule. In order to grow ZnO in thermal equilibrium, it is also required that  $\mu_{\text{ZnO}} = \mu_{\text{Zn}} + \mu_{\text{O}}$ , where  $\mu_{\text{ZnO}}$  is the formation energy of wurtzite ZnO. For the chemical potential of F ( $\mu_{\text{F}}$ ), the energy per F atom of  $\text{ZnF}_2$  and  $\text{F}_2\text{O}_2$  for Zn-rich and O-rich conditions are used, respectively.

### 6.2.2 X-ray Absorption Spectroscopy

Due to the low concentration of F, only the spectra in the near edge region (XANES) of the F  $K$ -edge are obtained experimentally. The electronic transition associated with the XAS measurement must follow the dipole selection rule, in which the X-ray absorbance  $\mu(\omega)$  is given by the Fermi's golden rule

$$\mu \propto \sum_f |\langle f | D | i \rangle|^2 \delta(E_i - E_f + \omega), \quad (6.1)$$

where  $|i\rangle$ ,  $|f\rangle$ ,  $E_i$ , and  $E_f$  are the initial and final states and their energies, respectively.  $\omega$  and  $D$  denote the photon frequency and dipole operator. The Fermi's golden rule restricts the transition of the core electrons to only the symmetry-allowed states.  $K$ -edge absorption refers to the excitation where the initial state is the first shell (1s) electron which has an even parity, i.e. is symmetric under inversion. Therefore, the final state with the dipole operator in Eqn. (6.1) has to have an odd parity, and in this case the final state is one of the empty  $p$  states.

To calculate a XANES spectrum, first we relax the local structure to its

unstrained configuration by using first principles calculations (the VASP codes in this case) and then employs the FEFF8.2 codes (Ankudinov et al., 1998) to simulate the XANES spectrum of that configuration. The FEFF codes uses a full multiple scattering approach based on *ab initio* overlapping muffin-tin potentials. The muffin-tin potentials are obtained using self-consistent calculations with Hedin-Lundqvist exchange-correlation function (Hedin and Lundqvist, 1969). By constructing a sphere with a radius of 8 Å (containing approximately 200 atoms) around the absorbing atom, the self-consistent calculations are obtained. From the simulations of pure-ZnO, it is found that the calculated XANES features are in good agreement with the measured spectra. Note that the simulated absolute photon energies differ from the experimental values by about 5 - 10 eV, depending on the system. This is expected due to the known incomplete correction of the empty core states during the excitation process that were not included in the ground state energy level calculations. Despite the error in the absolute energy, the relative energy, which holds the crucial information on the spectra features, is much more reliable.

## 6.3 Results and Discussions

### 6.3.1 Formation Energy of Fluorine in ZnO

In order to identify the favorable sites for F in ZnO, the formation energies of various F configurations, as well as selected native defects, are calculated. The formation energy of each defect indicates the likelihood of it to form (the low energy ones are more likely to form). In Figure 6.2, the formation energy is plotted as a function of electron Fermi energy in two extreme growth conditions (Zn-rich and O-rich). For actual growth conditions that might differ from either of

the two cases described in Chapter III. The formation energies of defects depend on the growth conditions because the chemical potential of F ( $\mu_F$ ) is set to the maximum possible value of F as limited by  $\text{ZnF}_2$  formation in Zn-rich conditions or as limited by  $\text{F}_2\text{O}_2$  molecule formation in O-rich conditions. For charged defects, the formation energies also depend on the Fermi energy,  $E_F$ , which can vary from the valence band maximum (VBM) to the conduction band minimum (CBM) in semiconductors. Both native defects and F impurities are plotted in the same graph for comparison. The calculated formation energy of an oxygen vacancy ( $V_{\text{O}}$ ) agrees well with the calculation by Janotti et al. (Janotti et al., 2006). The three F impurity defects with the lowest formation energies are  $F_{\text{O}}$ ,  $F_{i(\text{oct})}\text{-F}_{\text{O}}$ , and  $F_{\text{Zn}}\text{-F}_{\text{O}}$ . Their (calculated) relaxed local structures are shown in Figure 6.3. The calculations show that none of these three impurity defects induce defect levels inside the band gap.  $F_{\text{O}}$ ,  $F_{i(\text{oct})}\text{-F}_{\text{O}}$ , and  $F_{\text{Zn}}\text{-F}_{\text{O}}$  act as a shallow donor, charge neutral mid-gap state, and shallow acceptor, respectively. Under Zn-rich conditions (Figure 6.2, left panel),  $F_{\text{O}}$  has the lowest formation energy, indicating that F prefers to substitute for the oxygen atom. On the other hand, under O-rich conditions (Figure 6.2, right panel),  $F_{i(\text{oct})}\text{-F}_{\text{O}}$  and  $F_{\text{Zn}}\text{-F}_{\text{O}}$  complexes have low formation energies. When the Fermi energy is less than 0.9 eV, i.e. under *p*-type conditions, the self-compensating complex  $F_{i(\text{oct})}\text{-F}_{\text{O}}$ , which is electrically inactive, is the most stable complex. For a higher Fermi level,  $F_{\text{Zn}}\text{-F}_{\text{O}}$  which is a shallow acceptor is the most stable complex. Under our presumed chemical potential conditions (especially for F),  $V_{\text{Zn}}\text{-F}_{\text{O}}$ , which was earlier suggested to be the source of *p*-type ZnO (Yan and Wei, 2008) has higher formation energy than the  $F_{\text{Zn}}\text{-F}_{\text{O}}$  complex, indicating that both  $F_{\text{Zn}}\text{-F}_{\text{O}}$  and  $V_{\text{Zn}}\text{-F}_{\text{O}}$  could be the sources of *p*-type, depending on the specific chemical potential conditions of the growth environment. Note that, under *p*-type conditions, the self-compensating complex

$F_{i(\text{oct})}-F_{\text{O}}$  has lower formation energy than those of the acceptor complexes ( $F_{\text{Zn}}-F_{\text{O}}$  and  $V_{\text{Zn}}-F_{\text{O}}$ ). Therefore, one needs to tune the Fermi energy during growth to a value near the middle of the gap in order to successfully incorporate the desired acceptor complexes and suppress the unwanted ones. To further explore the stability of the complexes, their binding energies are calculated following the equation

$$E_b(AB) = E^f(A) + E^f(B) - E^f(AB), \quad (6.2)$$

where  $E^f(A)$ ,  $E^f(B)$ , and  $E^f(AB)$  are formation energies of isolated defect  $A$ , isolated defect  $B$ , and complex  $AB$ , respectively. The positive binding energy indicates that the complex is stable. Note, however, that having a positive binding energy is a requirement for a stable complex but is not a guarantee that the complex will form in a reasonable concentration. The populations of the complexes also depend on the growth conditions and absolute formation energies of them. Under thermodynamic approximations, the defects and defect complex concentrations can be calculated by using the detailed balance. The calculated binding energies of  $V_{\text{Zn}}-F_{\text{O}}$ ,  $F_{\text{Zn}}-F_{\text{O}}$ , and  $F_{i(\text{oct})}-F_{\text{O}}$  are 0.85, 1.60, and 1.07 eV, respectively, indicating that these complexes are all bound.

### 6.3.2 XANES of Fluorine in ZnO

To interpret the measured XANES features, the first principles simulations of F  $K$ -edge XANES for F at various locations in wurtzite-ZnO were performed. The measured spectrum is shown in the top panel [Figure 6.4 (a)], whereas the middle [Figure 6.4 (b)] and bottom panels [Figure 6.4(c)] display the simulated spectra. Figure 6.4 (b) depicts the simulated spectra of  $F_{\text{O}}$  and its complexes

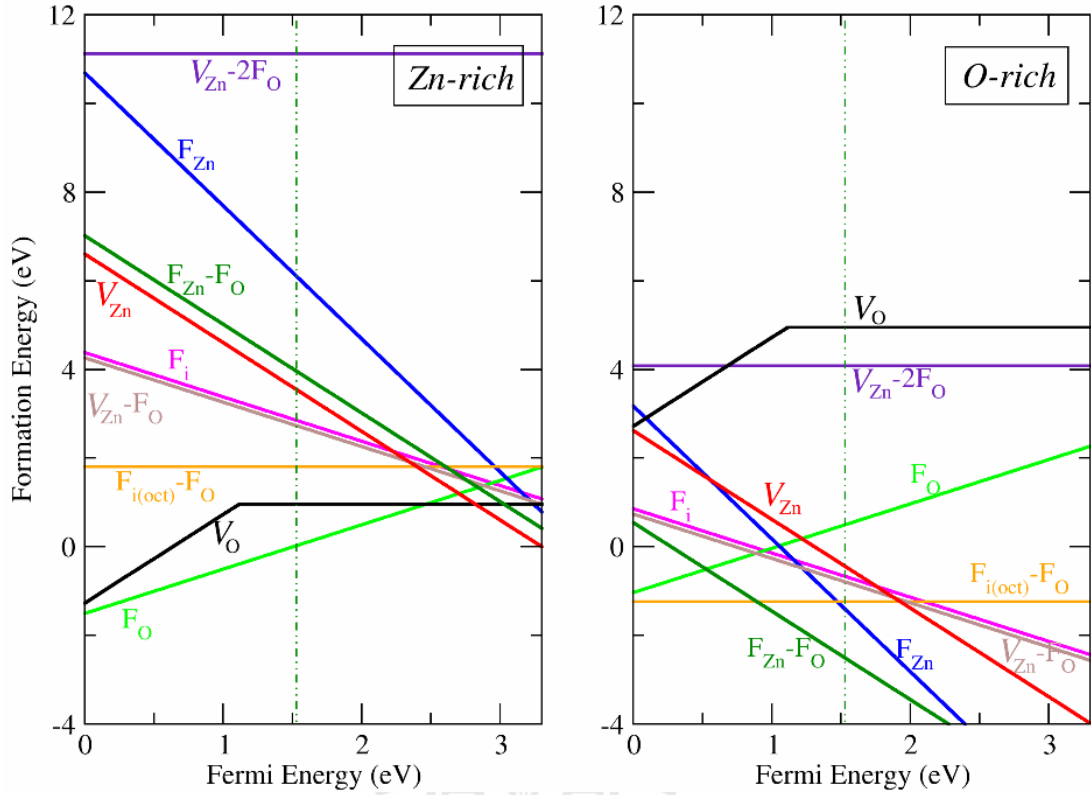


**Figure 6.2** The calculated formation energies of native defects and F impurities in wurtzite ZnO as a function of Fermi level calculated under Zn-rich and O-rich conditions, respectively.

with  $V_{Zn}$  as well as other defects ( $F_{Zn}$ ,  $F_i$ , and  $F_i-F_O$ ). The simulated spectrum of  $ZnF_2$  is illustrated in Figure 6.4 (c). The optimized local structures of them are shown in Figure 6.3. It is found by comparing the main peaks that the simulated spectra are shifted from the measured one by about 11 eV due to the incomplete core-hole corrections. However, this should not affect the feature comparison between them. The measured XANES can be divided into two regions: the lower-energy region which contains a strong-absorption peak  $p_1$  (692 eV) and a shoulder  $s_1$  (near 696 eV) and the higher-energy region, where the spectrum is much broader and has only a weak-absorption peak  $p_2$  (701 eV). Note that  $F_O$  and its complexes with  $V_{Zn}$  have similar features except that  $F_O$  has stronger peaks than those of the complexes as shown in Figure 6.4 (b). Because the features of

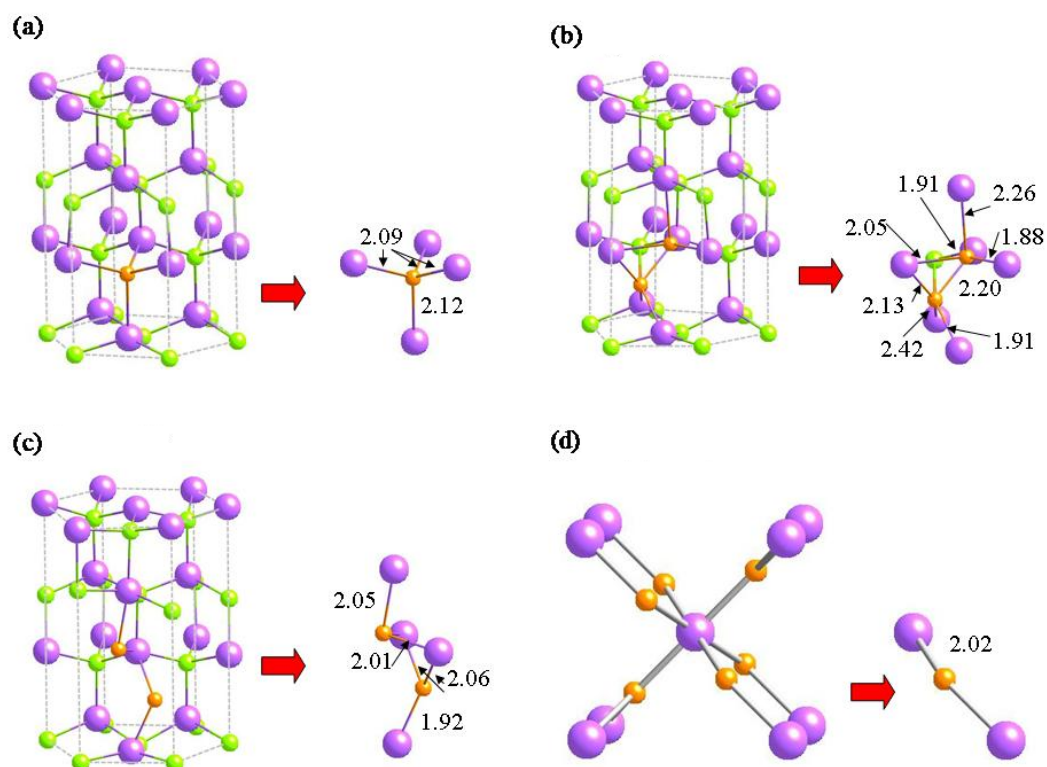


**Figure 6.3** The local structure of F atoms in  $F_O^+$ ,  $(F_{i(oct)}-F_O)^0$ ,  $(F_{Zn}-F_O)^{2-}$ , and  $ZnF_2$  in wurtzite ZnO.

$F_O$  and its complexes with  $V_{Zn}$  are similar, it would be difficult to distinguish between them. Other defects ( $F_{Zn}$ ,  $F_i$ , and  $F_i-F_O$ ) do not resemble the experimental data. Based on the formation energies we can predict that, under Zn-rich conditions, isolated  $F_O$  could form in higher concentration because  $V_{Zn}$  has high formation energy. On the other hand, under O-rich conditions, where the  $V_{Zn}$  can form more easily, the  $V_{Zn}-F_O$  complex is expected to be favorable, especially when the Fermi level is in the  $p$ -type range. In the low-energy region, the peak  $p_1$  and the shoulder  $s_1$ , indicated by red- and light-blue dashed line in Figure 6.4, are consistent with a peak and a shoulder observed in the simulated spectra of  $F_O$  as well as its complexes with  $V_{Zn}$ . However, the simulated spectrum of  $ZnF_2$  also contains similar features. To simulate the best fit, we mix the simulated spectra

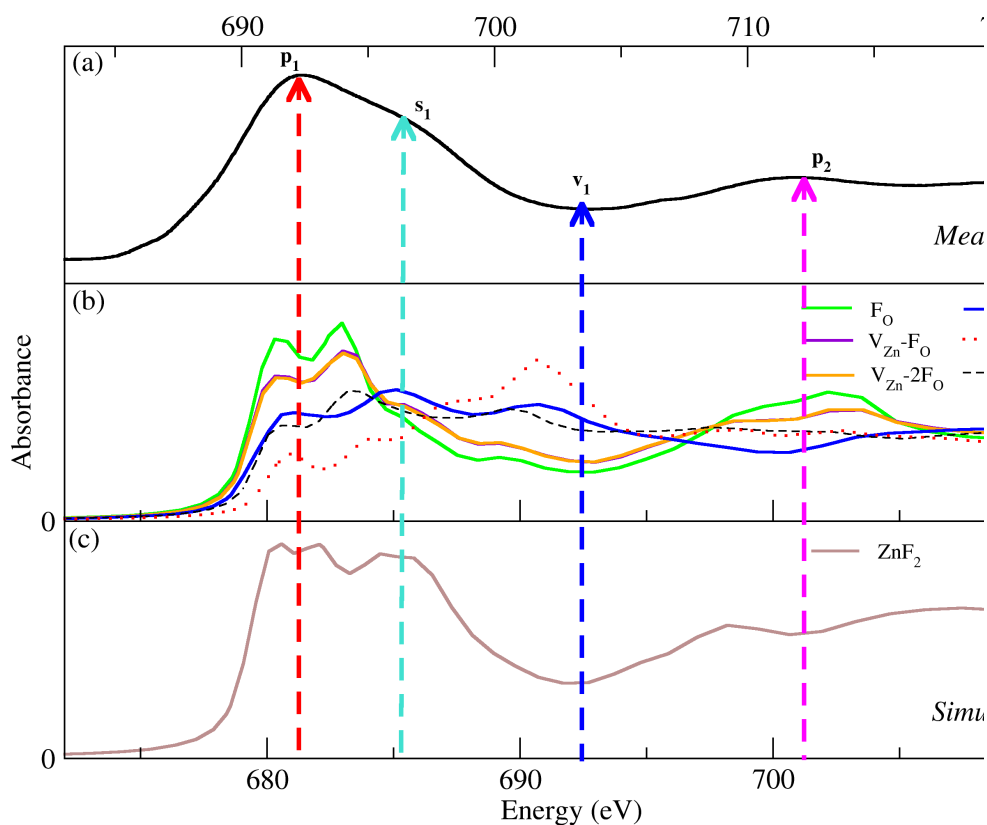


**Figure 6.4** Comparison between the measured F  $K$ -edge XANES spectra (taken from SNU) and the calculated F  $K$ -edge XANES spectra obtained from FEFF.

of  $F_0$  and  $ZnF_2$  with different ratios and plotted them in the same graph (Figure 6.5) along with the measured one. For ease of comparison, the simulated spectra are shifted by 11 eV to align the main features with the measure one. It is found that the mixing ratio of 1:1 provide the spectrum with the best match of  $p_1$  and  $s_1$  to the measured features. In the higher energy region, the simulated spectrum has a broad peak near peak  $p_2$  of the measured one.

## 6.4 Conclusions

In order to identify the local structure of fluorine in  $ZnO$ , first principles calculations have been employed to simulate the XANES of various local structures

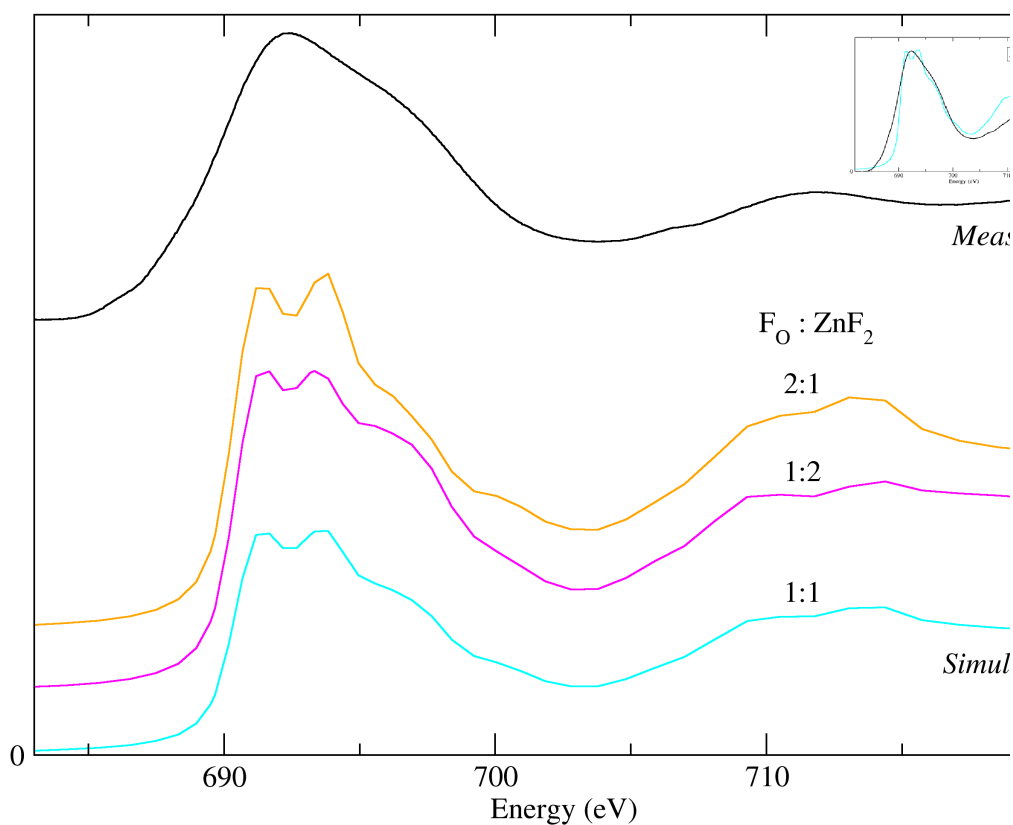


**Figure 6.5** The measured (taken from SNU) and the simulated F *K*-edge XANES spectra of combination of  $F_O$  and  $ZnF_2$  with various ratios in ZnO.

of F in ZnO as well as some possible phase precipitated F. By comparing with the actual XANES measurement of F-doped ZnO, it is found that the combination of  $F_O$  (as well as the complexes of  $V_{Zn}$  and  $F_O$  which has similar XANES features) and  $ZnF_2$  provides the spectrum that best matches the observed one. This is also consistent with the formation energy calculations where  $F_O$  and  $V_{Zn}-F_{Ah070}$  are found to have low formation energies.

# CHAPTER VII

## CONCLUSION AND FUTURE WORK

In this thesis, selected point defects and impurities in  $\text{TiO}_2$  and  $\text{ZnO}$  were studied by first-principles calculations. A theoretical background of first-principles density functional theory was given in Chapter II. In Chapter III, the calculation methods for defects in semiconductors were explained briefly.

For  $\text{TiO}_2$ , it is of current interest to modify the band gap such that it can serve more effectively as a photocatalyst under solar spectrum. In Chapter IV, the study of sulfur doped  $\text{TiO}_2$  were reported in detailed. Despite mixed success in the experimental reports of attempts to lower the band gap while maintaining high photocatalytic activity of  $\text{TiO}_2$  by doping with S, we found that all of the studied sulfur defects ( $S_i$ ,  $S_{\text{Ti}}$ , and  $S_{\text{O}}$ ) act as donors and introduce deep defect levels inside the band gap. Therefore, there are no indications from our results that S-doping is a good approach to lower the band gap of  $\text{TiO}_2$ . In Chapter V, the study of various impurity pairs were reported. The purpose of this study was to find potentially good co-doping pairs that could lower the band gap and maintain high photocatalytic activity of  $\text{TiO}_2$  with a focus on antibacterial applications. Based on the analysis, a good co-doping pair should maintain  $\text{TiO}_2$  electron counting and provide two impurity levels within  $\approx 0.25$  eV of the VBM and CBM, respectively. It is found that vanadium substitution for Ti and N substitution for O ( $V_{\text{Ti}}\text{-N}_{\text{O}}$ ) are the best candidates. However, the doping procedure to deposit impurities on both Ti and O sites could be challenging.

$\text{ZnO}$  is one of the most studied wide band gap semiconductors due to its

strong potential as a brighter blue-light emitter than GaN, the current standard material. However, there is as yet no high quality *p*-type ZnO. Fluorine is one of the impurities that has been proposed as a means of doping ZnO into *p*-type. In Chapter VI, first principles calculations of F doped ZnO were reported. Based on the formation energy calculations, it is found that F prefers to substitute for O and to behave as a donor. However, under certain conditions, it could form a complex with Zn vacancy ( $F_O-V_{Zn}$ ) which is a shallow acceptor. To help identify the local structures of F, the simulation of X-ray absorption spectra of various F configurations in ZnO are studied. After comparing with the measured spectrum, the best candidate for the observed spectrum is the mixture of F substitution for O ( $F_O$ ) and phase precipitated  $ZnF_2$ . However, the spectral features of the  $F_O$  and  $F_O-V_{Zn}$  are quite similar and  $F_O-V_{Zn}$  could not completely be ruled out.

In the future, I am planning to employ the methodology used in this thesis to study defects in other material systems. For example, defects in  $Al_2O_3$  that are known to be the cause of the variable color of this material. Potential impurities to be studied are chromium (believed to be the source of red in ruby), Ti and Fe (believed to be the source of blue). Although, these impurities might have been previously studied by first principles calculations, most (if not all) of them are based on DFT where the band gap is severely underestimated. To obtain the correct color information, precise defect levels are needed. Therefore, a much more computational intensive calculations based on hybrid functional, which just becomes possible recently, are needed. This opens up an opportunity to repeat those calculations with this new and computationally expensive approach.



## REFERENCES

## REFERENCES

- Ahn, K. S., Yan, Y., Shet, S., Deutsch, T., Turner, J., and Al-Jassim, M. (2007). Enhanced photoelectrochemical responses of ZnO films through Ga and N codoping. **Appl. Phys. Lett.** 91: 231909–231912.
- Anisimov, V. I., Zaanen, J., and Anderson, O. K. (1991). Band theory and Mott insulators: Hubbard U instead of Stoner I. **Phys. Rev. B** 44: 943–954.
- Ankudinov, A. L., Ravel, B., Rehr, J. J., and Conradson, S. D. (1998). Real-space multiple-scattering calculation and interpretation of X-ray-absorption near edge structure. **Phys. Rev. B** 58: 7565–7576.
- Asahi, R. and Morikawa, T. (2007). Nitrogen complex species and its chemical nature in TiO<sub>2</sub> for visible-light sensitized photocatalysis. **Chem. Phys.** 339: 57–63.
- Asahi, R., Morikawa, T., Ohwaki, T., Aoki, A., and Taga, Y. (2001). Visible-light photocatalysis in nitrogen-doped titanium oxides. **Science.** 293: 269–271.
- Asahi, R., Taga, Y., Mannstadt, W., and Freeman, A. J. (2000). Electronic and optical properties of anatase TiO<sub>2</sub>. **Phys. Rev. B** 61: 7459–7465.
- Barth, U. V. and Hedin, L. (1972). A local exchange-correlation potential for the spin polarized Case: I. **J. Phys. Cond. Matter** 5: 1629–1642.
- Becke, A. D. (1993a). A new mixing of HartreeFock and local density-functional theories. **J. Chem. Phys.** 98: 1372–1377.

- Becke, A. D. (1993b). Density-functional thermochemistry. III. The role of exact exchange. **J. Chem. Phys.** 99: 5648–5652.
- Bloch, F. (1928). Über die Quantenmechanik der Elektronen in Kristallgittern. **Phys. Rev. B** 52: 555–600.
- Bloch, P. E. (1994). Projector augmented-wave method. **Phys. Rev. B** 50: 17953–17979.
- Born, M. and Oppenheimer, J. R. (1927). On the quantum theory of molecules. **Ann. Physik.** 84: 457–484.
- Byrne, J. A., Fernandez-Ibanez, P. A., Dunlop, P. S. M., Alrousan, D. M. A., and Hamilton, J. W. J. (2011). Photocatalytic enhancement for solar disinfection of water: A review. **Int. J. Photoenergy.** 78051: 1–12.
- Calatayud, M., Mori-Sánchez, P., Beltrán, A., Pendas, A. M., F. E. A. J., and Recio, J. M. (2001). Quantum-mechanical analysis of the equation of state of anatase TiO<sub>2</sub>. **Phys. Rev. B** 64: 184113–184121.
- Ceperley, D. M. and Alder, B. J. (1980). Ground state of electron gas by a stochastic method. **Phys. Rev. Lett.** 45: 566–569.
- Chand, N., Henderson, T., Klem, J., Masselink, W. T., Fischer, R., Chang, Y.-C., and Morko, H. (1984). Comprehensive analysis of Si-doped Al<sub>x</sub>Ga<sub>1-x</sub>As (x=0 to 1): Theory and experiments. **Phys. Rev. B** 30: 4481–4492.
- Cordero, B., Gómez, V., Platero-Prats, A. E., Revs, M., Echeverría, J., Cremades, E., Barragán, F., and Alvarez, S. (2008). Covalent radii revisited. **Dalton Trans** 21: 2832–2838.

- Di Valentin, C., Pacchioni, G., and Selloni, A. (2004). Origin of the different photoactivity of N-doped anatase and rutile  $\text{TiO}_2$ . **Phys. Rev. B** 70: 085116–085119.
- Diebold, U. (2003). The many faces of rutile titania. **Surf. Sci. Rep.** 48: 53–229.
- Dirac, P. A. M. (1930). Note on the exchange phenomena in the Thomas atom. **Proc. Cambridge Philos. Soc.** 26: 376–385.
- Emeline, A. V., Kuzmin, G. N., and Serpone, N. (2008). Wavelength-dependent photostimulated adsorption of molecular  $\text{O}_2$  and  $\text{H}_2$  on second generation titania photocatalysts: The case of the visible-light-active N-doped  $\text{TiO}_2$  system. **Chem. Phys. Lett.** 454: 279–283.
- Fahmi, A., Minot, C., Silvi, B., and Caus, M. (1993). Theoretical analysis of the structures of titanium dioxide crystals. **Phys. Rev. B** 47: 11717–11724.
- Fermi, E. (1928). A statistical method for the determination of some atomic properties and the application of this method to the theory of the periodic system of elements. **Z. Physik.** 48: 73–79.
- Feynman, R. P. (1939). Forces in molecules. **Phys. Rev.** 56: 340–343.
- Filippi, C., Singh, D. J., and Umrigar, C. J. (1994). All-electron local-density and generalized-gradient calculations of the structural properties of semiconductors. **Phys. Rev. B** 50: 14947–14951.
- Fujishima, A. (2000). Titanium dioxide photocatalysis. **J. Photochem. Photobiol. C: Photochem. Rev.** 1: 1–21.
- Fujishima, A., Zhang, X., and Tryk, D. A. (2007). Heterogeneous photocatalysis:

From water photolysis to applications in environmental cleanup. **Int. J. Hydrogen Energy.** 32: 2664–2672.

Gai, Y., Li, J., Li, S. S., Xia, J. B., and Wei, S. H. (2009). Design of narrow-gap TiO<sub>2</sub>: A passivated codoping approach for enhanced photoelectrochemical activity. **Phys. Rev. Lett.** 102: 036402–036410.

Greenwood, N. N. and Earnshaw, A. (1997). **Chemistry of the elements.** 2. United Kingdom: Oxford University press.

Han, F., Kambala, V. S. R., Srinivasan, M., Rajarathnam, D., and Naidu, R. (2009). Tailored titanium dioxide photocatalysts for the degradation of organic dyes in wastewater treatment: A review. **Appl. Catal. A** 359: 25–40.

Hashimoto, K., Irie, H., and Fujishima, A. (2005). TiO<sub>2</sub> photocatalysis: A historical overview and future prospects. **Jpn. J. Appl. Phys.** 44: 8269–8285.

Hattori, A., Yamamoto, M., Tada, H., and Ito, S. (1998). A promoting effect of NH<sub>4</sub>F addition on the photocatalytic activity of sol-gel TiO<sub>2</sub> films. **Chem. Lett.** 8: 707–708.

Hebenstreit, E. L., Hebenstreit, W., and Diebold, U. (2000). Adsorption of sulfur on TiO<sub>2</sub>(110) studied with STM, LEED and XPS: Temperature-dependent change of adsorption sites combined with O-S exchange. **Surf. Sci.** 461: 87–97.

Hedin, L. and Lundquist, B. I. (1971). Explicit local exchange-correlation potentials. **J. Phys. C** 4: 2064–2083.

- Hedin, L. and Lundqvist, S. (1969). Effects of electron-electron and electron-phonon interactions on the one-electron states of solids. **Sol. Stat. Phys.** 23: 1–181.
- Heine, V. (1970). **The Pseudopotential Concept**. 24. New York: Academic Press.
- Hellmann, H. (1937). **Einführung in die Quantenchemie**. Deuticke: Leipzig.
- Heyd, J., Scuseria, G. E., and Ernzerhof, M. (2003). Hybrid functionals based on a screened Coulomb potential. **J. Chem. Phys.** 118: 8207–8215.
- Heyd, J., Scuseria, G. E., and Ernzerhof, M. (2006). Hybrid functionals based on a screened Coulomb potential. **J. Chem. Phys.** 124: 219906.
- Hoffmann, M. R. (1995). Environmental applications of semiconductor photocatalysis. **Chem. Rev.** 95: 69–96.
- Hohenberg, P. and Kohn, W. (1964). Inhomogeneous electron gas. **Phys. Rev. B** 136: 864–871.
- Howard, C. J., Sabine, T. M., and Dickson, F. (1991). Structural and thermal parameters for rutile and anatase. **Acta Cryst. B** 47: 462–468.
- Huda, M. N., Yan, Y., Wei, S.-H., and Al-Jassim, M. (2008). Electronic structure of ZnO:GaN compounds: Asymmetric bandgap engineering. **Phys. Rev. B** 78: 195204–195208.
- Janotti, A., Segev, D., and Van de Walle, C. G. (2006). Effects of cation d states on the structural and electronic properties of III-nitride and II-oxide wide-band-gap semiconductors. **Phys. Rev. B** 74: 045202–045208.

- Janotti, A. and Van de Walle, C. G. (2007). Native point defects in ZnO. **Phys. Rev. B** 76: 165202–165222.
- Khan, S. U. M., Al-Shahry, M., and Ingler, W. B. (2002). Efficient photochemical water splitting by a chemically modified  $n$ -TiO<sub>2</sub>. **Science**. 297: 2243–2245.
- Klein, A., Singh, D. J., and Umrigar, C. J. (1995). All-electron study of gradient corrections to the local-density functional in metallic systems. **Phys. Rev. B** 51: 4105–4109.
- Kittel, C. (1996). **Introduction to Solid State Physics**. New York: Wiley.
- Koch, W. and Holthausen, M. C. (2001). **A Chemists Guide to Density Functional Theory**. Wiley-VCH Verlag GmbH.
- Kohn, W. (1999). Nobel Lecture: Electronic structure of matterwave functions and density functionals. **Rev. Mod. Phys.** B 71: 1253–1266.
- Kohn, W. and Sham, L. (1965). Self-consistent equations including exchange and correlation effects. **Phys. Rev. A** 140: 1133–1138.
- Kresse, G. and Furthmüller, J. (1996a). Efficiency of ab-initio total energy calculations for metals and semiconductors using a plane-wave basis set. **Comput. Mater. Sci.** 6: 15–50.
- Kresse, G. and Furthmüller, J. (1996b). Efficient iterative schemes for ab initio total-energy calculations using a plane-wave basis set. **Phys. Rev. B** 54: 11169–11186.
- Kresse, G. and Hafner, J. (1994). Ab-initio molecular-dynamics simulation of the

liquid-metal-amorphous-semiconductor transition in germanium. **Phys. Rev. B** 49: 14251–14269.

Kresse, G. and Joubert, D. (1999). From ultrasoft pseudopotentials to the projector augmented-wave method. **Phys. Rev. B** 59: 1758–1775.

Lany, S. and Zunger, A. (2008). Assessment of correction methods for the band-gap problem and for finite-size effects in supercell defect calculations: Case studies for ZnO and GaAs. **Phys. Rev. B** 78: 235104–235111.

Lee, I. H. and Martin, R. M. (1997). Applications of the generalized-gradient approximation to atoms, clusters, and solids. **Phys. Rev. B** 56: 7197–7205.

Li, J., Wei, S.-H., Li, S.-S., and Xia, J.-B. (2006). Design of shallow acceptors in ZnO: First-principles band-structure calculations. **Phys. Rev. B** 74: 081201–081204.

Liechtenstein, A. I., Anisimov, V. I., and Zaanen, J. (1995). Density-functional theory and strong interactions: Orbital ordering in Mott-Hubbard insulators. **Phys. Rev. B** 52: 5467–5470.

Limpijumnong, S., Li, X., Wei, S.-H., and Zhang, S. B. (2005). Substitutional diatomic molecules NO, NC, CO, N<sub>2</sub>, and O<sub>2</sub>: Their vibrational frequencies and effects on *p* doping of ZnO. **Appl. Phys. Lett.** 86: 211910–211913.

Limpijumnong, S., Rujirawat, S., Boonchun, A., Smith, M. F., and Cherdhirunkorn, B. (2007). Identification of Mn site in Pb(Zr,Ti)O<sub>3</sub> by synchrotron X-ray absorption near-edge structure: Theory and experiment. **Appl. Phys. Lett.** 90: 103113–103115.

- Limpijumnong, S., Smith, M. F., and Zhang, S. B. (2006). Characterization of As-doped, p-type ZnO by X-ray absorption near-edge structure spectroscopy: Theory. **Appl. Phys. Lett.** 89: 222113–222115.
- Look, D. C., Claffin, B., Alivov, Y. I., and Park, S. J. (2004). The future of ZnO light emitters. **Phys. Stat. Sol. A** 201: 2203–2212.
- Ma, X., Miao, L., Bie, S., and Jiang, J. (2010). Synergistic effect of V/N-codoped anatase TiO<sub>2</sub> photocatalysts. **Solid State Commun.** 150: 689–692.
- Marsman, M., Paier, J., Stoppa, A., and Kresse, G. (2008). Hybrid functionals applied to extended systems. **J. Phys. Condens. Matter** 20: 064201–064209.
- Marx, D. and Hutter, J. (2000). **Ab initio molecular dynamics: Theory and implementation; Modern Methods and Algorithms of Quantum Chemistry**. 1. Jülich: Forschungszentrum.
- Methfessel, M. and Paxton, A. T. (1989). High-precision sampling for Brillouin-zone integration in metals. **Phys. Rev. B** 40: 3616–3621.
- Monkhorst, H. J. and Pack, J. D. (1976). Special points for Brillouin-zone integrations. **Phys. Rev. B** 13: 5188–5192.
- Morkoc, H. (1999). **Nitride Semiconductors and Devices**. New York: Springer.
- Na-Phattalung, S., Smith, M. F., Kim, K., Du, M. H., Wei, S., Zhang, S. B., and Limpijumnong, S. (2006). First-principles study of native defects in anatase TiO<sub>2</sub>. **Phys. Rev. B** 73: 125205–125210.

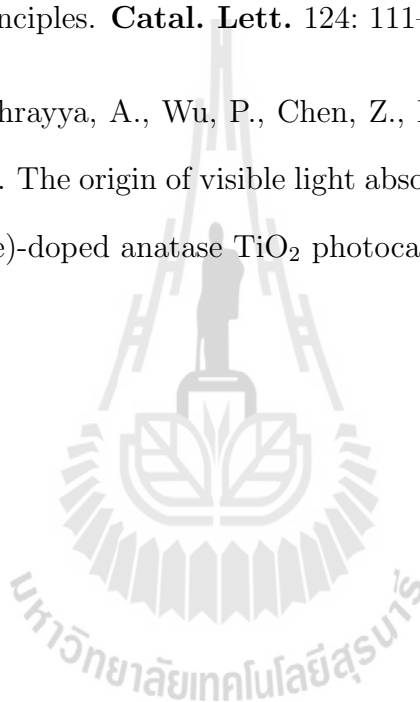
- Nieminen, R. M. (2009). Issues in first-principles calculations for defects in semiconductors and oxides. **Modelling Simul. Mater. Sci. Eng.** 17: 084001.
- Northrup, J. E. and Zhang, S. B. (1994). Energetics of the As vacancy in GaAs: The stability of the 3+ charge state. **Phys. Rev. B** 50: 4962–4964.
- Ortiz, G. and Ballone, P. (1991). Pseudopotentials for non-local-density functionals. **Phys. Rev. B** 43: 6376–6387.
- Paier, J., Marsman, M., Hummer, K., Kresse, G., Gerber, I. C., and Angyan, J. G. (2006). Screened hybrid density functionals applied to solids. **J. Chem. Phys.** 124: 154709–154712.
- Paier, J., Marsman, M., and Kresse, G. (2007). Why does the B3LYP hybrid functional fail for metals? **J. Chem. Phys.** 127: 024103–024112.
- Panpan, S., Xiyu, S., Qinying, H., Yadong, L., and Wei, C. (2009). First-principles calculation of the electronic band of ZnO doped with C. **J. Semicond.** 30: 52001.
- Park, C. H., Zhang, S. B., and Wei, S. H. (2002). Origin of p-type doping difficulty in ZnO: The impurity perspective. **Phys. Rev. B** 66: 073202–073204.
- Payne, M. C., Teter, M. P., Allan, D. C., Arias, T. A., and Joannopoulos, J. D. (1992). Iterative minimization techniques for ab initio total-energy calculations: molecular dynamics and conjugate gradients. **Rev. Mod. Phys.** 64: 1045–1097.
- Perdew, J. P. (1985). Density functional theory and the band gap problem. **Int. J. Quant. Chem.** 28: 497–523.

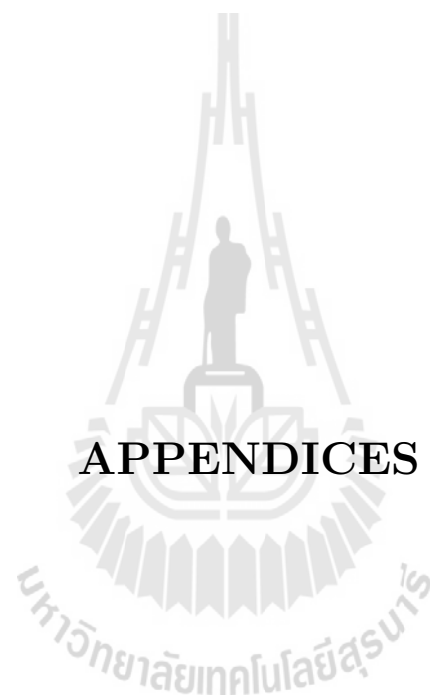
- Perdew, J. P., Burke, K., and Ernzerhof, M. (1996). Generalized gradient approximation made simple. **Phys. Rev. Lett.** 77: 3865–3868.
- Perdew, J. P. and Levy, M. (1983). Physical content of the exact Kohn-Sham orbital energies: Band gaps and derivative discontinuities. **Phys. Rev. Lett.** 51: 1888–1891.
- Perdew, J. P. and Wang, Y. (1986). Accurate and simple density functional for the electronic exchange energy: Generalized gradient approximation. **Phys. Rev. B** 33: 8800–8802.
- Perdew, J. P. and Wang, Y. (1993). Accurate and simple analytic representation of the electron-gas correlation energy. **Phys. Rev. B** 45: 13244–13249.
- Perdew, J. P. and Zunger, A. (1981). Self-interaction correction to density-functional approximations for many-electron systems. **Phys. Rev. B** 23: 5048–5079.
- Rodriguez, J. A., Chaturvedi, S., Kuhn, M., and Hrbek, J. (1998). Reaction of H<sub>2</sub>S and S<sub>2</sub> with metal/oxide surfaces: Band-gap size and chemical reactivity. **J. Phys. Chem. B** 192: 5511–5519.
- Schulz, H. and Thiemann, K. H. (1977). Crystal structure refinement of AlN and GaN. **Sol. Stat. Comm.** 23: 815–819.
- Sham, L. J. and Schluter, M. (1983). Density-functional theory of the energy gap. **Phys. Rev. Lett.** 51: 1888–1891.
- Stibor, A. (2001). **CO adsorption on iron surfaces: An ab-initio density-functional study**. Retrieved from <http://www.pit.physik.uni-tuebingen.de/stibor/>.

- T-Thienprasert, J., Nukeaw, J., Sungthong, A., Porntheeraphat, S., Singkarat, S., Onkaw, D., Rujirawat, S., and Limpijumnong, S. (2008). Local structure of indium oxynitride from X-ray absorption spectroscopy. **Appl. Phys. Lett.** 93: 051903–051905.
- T-Thienprasert, J., Rujirawat, S., Nukeaw, J., and Limpijumnong, S. (2010). X-ray absorption spectroscopy of indium nitride, indium oxide, and their alloys. **Comput. Mater. Sci. S** 49: 37–42.
- Tang, H., Berger, H., Schmid, P. E., Lvy, F., and Burri, G. (1993). Photoluminescence in TiO<sub>2</sub> anatase single crystals. **Solid State Commun.** 87: 847–850.
- Tang, J. and Ye, J. (2005). Photocatalytic and photophysical properties of visible-light-driven photocatalyst ZnBi<sub>12</sub>O<sub>20</sub>. **Chem. Phys. Lett.** 410: 104–107.
- Thomas, L. H. (1927). The calculation of atomic fields. **Proc. Cambridge Philo. Soc.** 23: 524–548.
- Troxell, J. R. and Watkins, G. D. (1980). Interstitial boron in silicon: A negative-U system. **Phys. Rev. B** 22: 921–931.
- Umabayashi, T., Yamaki, T., Itoh, H., and Asao, K. (2002). Band gap narrowing of titanium dioxide by sulfur doping. **Appl. Phys. Lett.** 81: 454.
- Umabayashi, T., Yamaki, T., Yamamoto, M., Miyashita, A., Tanaka, S., Sumita, T., and Asai, K. (2003). Sulfur-doping of rutile-titanium dioxide by ion implantation: Photocurrent spectroscopy and first-principles band calculation studies. **J. Appl. Phys.** 93: 5156.

- Van de Walle, C. G., Limpijumnong, S., and Neugebauer, J. (2001). First-principles studies of beryllium doping of GaN. **Phys. Rev. B** 63: 245205–245221.
- Van de Walle, C. G. and Neugebauer, J. (2004). First-principles calculations for defects and impurities: Applications to III-nitrides. **J. Appl. Phys.** 95: 3851–3879.
- Vanderbilt, D. (1990). Soft self-consistent pseudopotentials in a generalized eigenvalue formalism. **Phys. Rev. B** 41: 7892–7895.
- Vosko, S. H., Wilk, L., and Nusair, M. (1980). Accurate spin-dependent electron liquid correlation energies for local spin density calculations: a critical analysis. **Can. J. Phys.** 58: 1200–1211.
- Wang, H. and Lewis, J. P. (2005). Anion doping in  $\text{TiO}_2$ . **J. Phys. Condens. Matter. L** 17: 209.
- Yan, Y. and Wei, S. H. (2008). Doping asymmetry in wide-bandgap semiconductors: Origins and solutions. **Phys. Stat. Sol.** 245: 641–652.
- Zaleska, A., Sobczak, J. W., Grabowska, E., and Hupka, J. (2008). Preparation and photocatalytic activity of boron-modified  $\text{TiO}_2$  under UV and visible light. **Appl. Catal. B** 78: 92–100.
- Zhang, S. B. (2002). The microscopic origin of the doping limits in semiconductors and wide-gap materials and recent developments in overcoming these limits: A review. **J. Phys. Condens. Matter. R** 14: 881.
- Zhang, S. B. and Northrup, J. E. (1991). Chemical potential dependence of defect formation energies in GaAs: Application to Ga self-diffusion. **Phys. Rev. Lett.** 67: 2339–2342.

- Zhang, S. B., Wei, S.-H., and Zunger, A. (2001). Intrinsic *n*-type versus *p*-type doping asymmetry and the defect physics of ZnO. **Phys. Rev. B** 63: 075205–075212.
- Zhao, Z. and Liu, Q. (2008). Designed highly effective photocatalyst of anatase TiO<sub>2</sub> codoped with nitrogen and vanadium under visible-light irradiation using first-principles. **Catal. Lett.** 124: 111–117.
- Zheng, J. W., Bhattcahrayya, A., Wu, P., Chen, Z., Highfield, J., Dong, Z., and Xu, R. (2010). The origin of visible light absorption in chalcogen element (S, Se, and Te)-doped anatase TiO<sub>2</sub> photocatalysts.





**APPENDICES**

# APPENDIX A

## PUBLICATIONS AND PRESENTATIONS

### A.1 List of Publications

Smith, M. F., Setwong, K., Tongpool, R., Onkaw, D., Na-phattalung, S., Limpijumnong, S. and Rujirawat, S. (2007). Identification of bulk and surface sulfur impurities in  $\text{TiO}_2$  by synchrotron X-ray absorption near edge structure. **Appl. Phys. Lett.** 91: 142107.

T-Thienprasert, J., Klaithong, S., Niltharach, A., Worayingyong, A., Na-phattalung, S. and Limpijumnong, S. (2011). Local structures of cobalt in Co-doped  $\text{TiO}_2$  by synchrotron X-ray absorption near edge structures. **Curr. Appl. Phys.** 11: S279.

### A.2 List of Presentations (oral)

Na Phattalung, S., Zhang, S. B. and Limpijumnong, S. (March 2011). Modifying bandgap of  $\text{TiO}_2$  by co-doping: First principles study. In **Siam Physics Congress 2011**. Pattaya: Thai Physics Society.

Na Phattalung, S., Smith, M. F., Setwong, K., Tongpool, R., Onkaw, D., Rujirawat, S. and Limpijumnong, S. (October 2008). Identification of bulk and surface sulfur impurities in  $\text{TiO}_2$  by synchrotron X-ray absorption near edge structure & local structure around sulfur in titanium dioxide viewed by X-ray absorption spectroscopy. In **34<sup>th</sup> Congress on Science and Technology of Thailand**. Bangkok: The Science Society of Thailand.

Na Phattalung, S., Zhang, S. B. and Limpijumnong, S. (September 2007). First principles study of co-doping in  $\text{TiO}_2$ . In **4<sup>th</sup> Asian Consortium on Computational Materials Science**. Seoul, South Korea: Korea Institute of Science and Technology.

Na Phattalung, S., Smith, M. F., Setwong, K., Tongpool, R., Onkaw, D., Rujirawat, S. and Limpijumnong, S. (March 2007). Quantitative analysis of XANES on sulfur doped  $\text{TiO}_2$ : A first principles study. In **The Siam Physics Congress 2007**. Nakhon pathom: Thai Physics Society.

### **A.3 List of Presentations (poster)**

Na Phattalung, S., Zhang, S. B., Yu, J. and Limpijumnong, S. (September 2011). Modifying bandgap of  $\text{TiO}_2$  by co-doping: First Principles Study. In **6<sup>th</sup> Asian Consortium on Computational Materials Science**. Singapore: National University of Singapore.

Na Phattalung, S. and Limpijumnong, S. (March 2011). Defects in semiconductors. In **3<sup>rd</sup> HOPE Meeting**. Tokyo, Japan: Japan Society for the Promotion of Science.

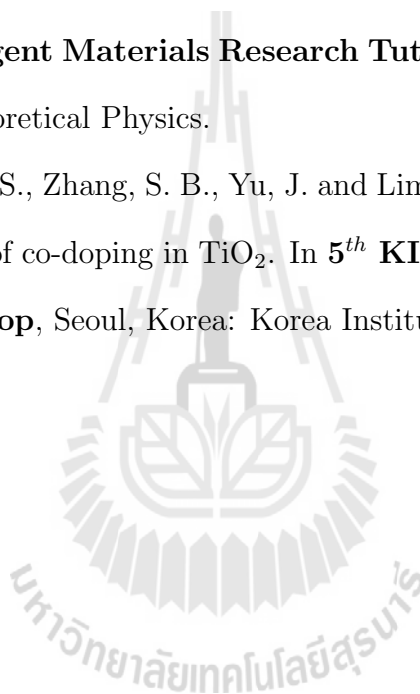
Na Phattalung, S., Zhang, S. B., Yu, J. and Limpijumnong, S. (July 2010). First Principles Study of Codoping in  $\text{TiO}_2$ . In **2<sup>nd</sup> APCTP-IACS Joint Conference International Conference on Physics of Novel Oxide Materials**. Pohang, Korea: Asia Pacific Center for Theoretical Physics.

Na Phattalung, S., Zhang, S. B., Yu, J. and Limpijumnong, S. (June 2010). Impurity pairs in  $\text{TiO}_2$ : First principles Calculations. In **Joint International Conference on the 7<sup>th</sup> Asian Meeting on Ferroelectricity and the 7<sup>th</sup> Asian Meeting on Electroceramics**. Jeju, Korea: The Korean Physical Society.

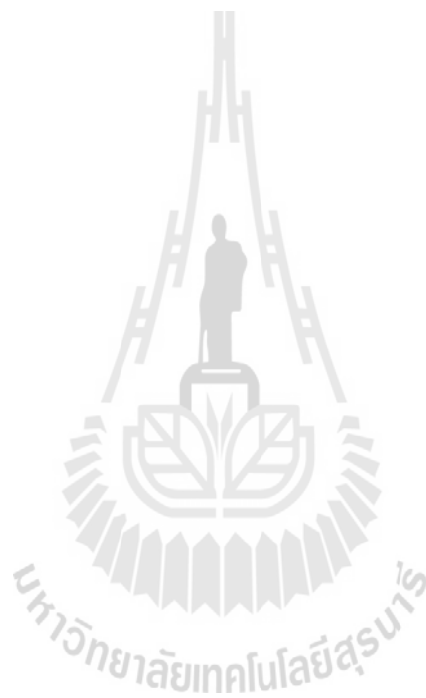
Na Phattalung, S., Yu, J. and Limpijumnong, S. (October 2009). First Principles Study of Fluorine in ZnO. In **12<sup>nd</sup> Asian Workshop on First-principles Electronic Structure Calculations**. Beijing, China: Chinese Academy of Science.

Na Phattalung, S., Yu, J. and Limpijumnong, S. (July 2009). First Principles Study of Fluorine in ZnO. In **2<sup>nd</sup> WWorkshop for Emergent Materials Research and Emergent Materials Research Tutorial**. Pohang, Korea: Asia Pacific Center for Theoretical Physics.

Na Phattalung, S., Zhang, S. B., Yu, J. and Limpijumnong, S. (June 2009). First principles study of co-doping in TiO<sub>2</sub>. In **5<sup>th</sup> KIAS Electronic Structure Calculation Workshop**, Seoul, Korea: Korea Institute for Advanced Study.



**APPENDIX B**  
**PUBLICATION PAPER**



## B.1 Manuscript Published in Applied Physics Letters

APPLIED PHYSICS LETTERS 91, 142107 (2007)

### Identification of bulk and surface sulfur impurities in TiO<sub>2</sub> by synchrotron x-ray absorption near edge structure

M. F. Smith<sup>a),b)</sup>

National Synchrotron Research Center, Nakhon Ratchasima 30000, Thailand

Kongthip Setwong and Rungnapa Tongpool

National Metal and Materials Technology Center, Pathumthani 12120, Thailand

Darin Onkaw, Sutassana Na-phattalung, Sukit Limpijumng, and Saroj Rujirawat<sup>a)</sup>

School of Physics, Suranaree University of Technology, Nakhon Ratchasima 30000, Thailand and National Synchrotron Research Center, Nakhon Ratchasima 30000, Thailand

(Received 26 July 2007; accepted 12 September 2007; published online 3 October 2007)

Synchrotron x-ray absorption near edge structure (XANES) measurements of Ti and S *K* edges, combined with first principles simulations, are used to characterize S-doped TiO<sub>2</sub> prepared by oxidative annealing of TiS<sub>2</sub> at various temperatures. Ti-edge XANES and x-ray powder diffraction data indicate that samples annealed above 300 °C have an anatase TiO<sub>2</sub> crystal structure with no trace of TiS<sub>2</sub> domains. S-edge XANES data reveal that the local structure seen by S atoms evolves gradually, from TiS<sub>2</sub> to a qualitatively different structure, as the annealing temperature is increased from 200 to 500 °C. For samples annealed at 500 °C, the spectrum appears to have features that can be assigned to S on the surface in the form of SO<sub>4</sub> and S defects in the bulk (most likely S interstitials) of TiO<sub>2</sub>. © 2007 American Institute of Physics. [DOI: 10.1063/1.2793627]

TiO<sub>2</sub> is a semiconductor photocatalyst which is used in applications such as air and water purifications.<sup>1–3</sup> Despite its advantages over other materials, such as better oxidizing power and chemical stability, its applicability is limited by a band gap (3.0–3.2 eV) that is too large to utilize effectively the spectrum of sunlight. A longstanding challenge is to lower the band gap of the material without too severely compromising properties beneficial to photocatalysis.

Sulfur-doped TiO<sub>2</sub>, prepared by oxidative annealing of TiS<sub>2</sub>, has been found to have a lower band gap than pure TiO<sub>2</sub>, giving a higher photocurrent under visible light.<sup>4,5</sup> Enhanced photocatalysis is seen when TiO<sub>2</sub> is doped with some elements, such as C, N, and F, which are claimed to substitute for O in the bulk, and S doping may have similar effects.<sup>6–11</sup> On the other hand, S impurities are known to inhibit photocatalytic reactions, so unwanted S impurities might limit photocatalytic performance.<sup>12–14</sup> To understand the role of sulfur in photocatalysis, it would be helpful to know how S is incorporated into TiO<sub>2</sub>.

Here, sulfur-doped TiO<sub>2</sub> prepared by oxidative annealing of TiS<sub>2</sub> powder<sup>4</sup> is characterized by Ti and S *K*-edge x-ray absorption near edge structure (XANES) measurements. Samples were annealed in air at 200, 300, 400, or 500 °C for 2 h. XANES measurements were made in the transmission mode at the X-ray absorption spectroscopy beamline (BL-8) of the Siam photon source (electron energy of 1.2 GeV), National Synchrotron Research Center (Thailand). Crystal monochromators [Si (111) for Ti *K* edge and InSb(111) for S *K* edge] were used with a scanning energy step of 0.25 eV. For energy calibration of Ti and S edges, we compared our XANES measurements of TiO<sub>2</sub> and TiS<sub>2</sub>, respectively, to previously published spectra.<sup>15,16</sup> X-ray powder diffraction (XRD) measurements were made for each sample to verify the crystal structure. More details of the sample preparation

and measurement will be published elsewhere.<sup>17</sup> The measured Ti and S *K*-edge XANES spectra are shown in Fig. 1 in comparison with the spectra for pure TiO<sub>2</sub> and TiS<sub>2</sub>.

The Ti *K*-edge XANES of the sample annealed at 200 °C combines features of TiS<sub>2</sub> and TiO<sub>2</sub>, indicating that oxidation is not completed and there are surviving TiS<sub>2</sub> domains at this temperature (Fig. 1, left panel). For samples annealed at 300 °C and above, the spectra are indistinguishable from that of pure TiO<sub>2</sub>, suggesting a full conversion to TiO<sub>2</sub>. Since the number of S atoms in such annealed samples is small compared to the number of O atoms, the Ti *K*-edge XANES will be little affected by the small fraction of Ti that lie close to S impurities. The XRD measurements (not shown) are consistent with these results; i.e., they indicate a small amount of TiS<sub>2</sub> in the sample annealed at 200 °C and no detectable TiS<sub>2</sub> domain for samples that are annealed at 300 °C and above. The TiO<sub>2</sub> structure is largely anatase, with a small (roughly 5%) rutile admixture.

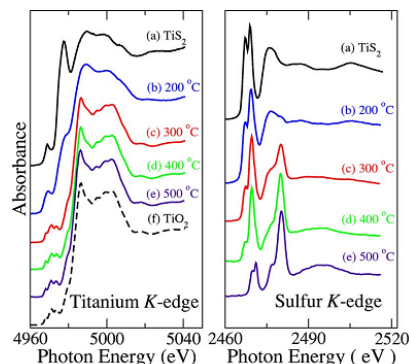


FIG. 1. (Color online) Measured Ti (left panel) and S (right panel) *K*-edge XANES. Curve (a) is for pure (unannealed) TiS<sub>2</sub> sample, while curves (b)–(e) are for TiS<sub>2</sub> that has been annealed in air for 2 h at temperatures of 200, 300, 400, and 500 °C, respectively. The spectrum of a pure TiO<sub>2</sub> is shown with a dashed curve (f).

<sup>a)</sup> Authors to whom correspondence should be addressed.

<sup>b)</sup> Current address. Department of Physics, University of Queensland, 4072 Brisbane, Australia. Electronic mail: msmith@physics.utoronto.ca

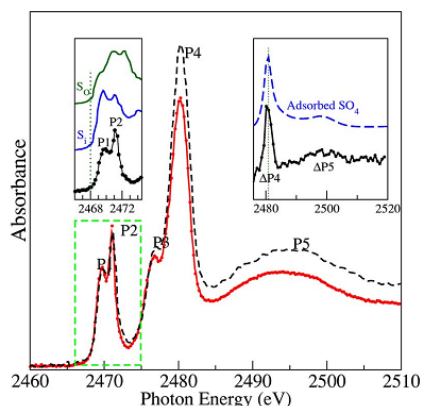


FIG. 2. (Color online) Sulfur  $K$ -edge XANES of the 500 °C annealed sample before (dashed curve) and after (solid curve) being washed with water. The lower-energy features (peaks P1 and P2), corresponds to S in the bulk, while the features in the higher-energy region (P3–P5) correspond to S at the  $\text{TiO}_2$  surface. Left inset: comparison between the measured XANES in the lower-energy region (bottom curve) with the simulation for bulk S defects (from top:  $\text{S}_0$  and  $\text{S}_i$ ) in  $\text{TiO}_2$ . The difference between the spectrum before and after washing is compared to the simulated XANES of S on  $\text{TiO}_2$  surface in the form of  $\text{SO}_4$ . The absolute photon energy of simulated spectra was slightly shifted (all shifts are smaller than 3 eV) to align a particular feature with the measured spectra.

Information on the local structure surrounding the remaining S atoms can be revealed by analyzing S  $K$ -edge XANES data (Fig. 1, right panel). At 200 °C, the XANES features remain similar to those of  $\text{TiS}_2$ , indicating that the local structure surrounding S atoms is  $\text{TiS}_2$ . With increasing temperature, new features emerge while  $\text{TiS}_2$  features are reduced such that the spectrum for samples annealed at 500 °C is qualitatively different from  $\text{TiS}_2$ . For the 500 °C annealed sample, XANES features can be divided into two regions (Fig. 2). In the lower-energy region, there are asymmetric double peaks, P1 (near 2469 eV) and P2 (2471 eV). In the higher-energy region, features are broader and include a large peak P4 (2481 eV), preceded by a small peak P3 (2477 eV), and followed by a broad hump P5 (centered on 2494 eV).

To interpret the observed XANES features, we use first principles simulations of XANES for S at various locations within anatase  $\text{TiO}_2$ , including bulk and surface sites. The simulations were performed using the FEFF 8 code<sup>18</sup> which employs a full-multiple scattering approach from self-consistent overlapping muffin-tin atomic potentials. The cluster size was increased until spectra converged (40–80 atoms, depending on the defect). From the simulations of pure systems such as  $\text{TiS}_2$  and free  $\text{SO}_4$  molecule, we found that the XANES features are in good agreement with the known spectra. However, the simulated absolute photon energies differed from the measured values by 1–2 eV (the relative energies are much more accurate).

For bulk defects, we have calculated sulfur substitute oxygen ( $\text{S}_0$ ), sulfur substitute titanium ( $\text{S}_{\text{Ti}}$ ), and sulfur interstitial ( $\text{S}_i$ ). To achieve realistic local atomic structures surrounding the S atom and to gain insight into the impurity (electronic) levels, each bulk defect was initially studied by a *first principles* total energy calculation based on the Vienna *ab initio* Simulation Package (VASP 4.6) using the supercell

approach.<sup>19</sup> The electron distributions and the position of each atom are allowed to relax to their minimum energy configurations in the calculations (all Hellman-Feynman forces in our 48-atom supercell are less than 0.05 eV/Å in the relaxed structure.) We used density functional theory within the local density approximation and ultrasoft pseudo-potentials. The cutoff energy for the plane-wave basis set is 300 eV. (The details of the computations are similar to those in Ref. 20.) All three impurities are found to produce defect levels in the  $\text{TiO}_2$  band gap. As a result, the stable charge state of the impurities changes from being positive (2+ for  $\text{S}_0$  and  $\text{S}_{\text{Ti}}$  and 4+ for  $\text{S}_i$ ) to neutral as the Fermi level is raised through the defect levels. (Note that one should not confuse “charge state” with “oxidation number.” They are different quantities.) We carried out the XANES simulations for both stable charge states for each bulk impurity configuration.

The bulk defect spectra have at least one thing in common: their main peaks are located in the photon energy range of 2465–2475 eV (i.e., within the lower-energy region of the measured spectrum). Therefore, while bulk defects may explain the lower-energy region, they cannot be responsible for features observed in the higher-energy region. We compare all the bulk defect spectra to the observed lower-energy region to identify the most likely bulk S site.

The simulated spectra of  $\text{S}_{\text{Ti}}$  (not shown) do not resemble the data and are therefore excluded. The simulations of  $\text{S}_0$  and  $\text{S}_i$  are shown in comparison with the measured XANES (Fig. 2, left inset). For ease of comparison, each simulation is shifted in energy so that its absorption threshold is aligned with the measured value (shifted down by 1.5–1.9 eV), and only the charge state most resembling the data for each defect is shown. The simulated spectrum of  $\text{S}_i$  is a closer match to the observed spectrum than that of  $\text{S}_0$ . The simulation for the neutral  $\text{S}_i$  accounts for (1) the relative position of P1 (1.6 eV above the threshold) and (2) the P2-P1 peak separation (1.4 eV). Although  $\text{S}_0$  cannot be completely ruled out, we tentatively assign the P1-P2 double peak feature observed in the lower-energy region to interstitial sulfur. This assignment is supported by the fact that the anatase phase of  $\text{TiO}_2$  has ample interstitial space and our previous total energy calculations have shown interstitial defects to be favorable for many nonmetallic species, especially in O-rich growing conditions. The local structure of neutral  $\text{S}_i$  obtained from our first principles structural relaxation is illustrated in Fig. 3. The interstitial S atom bonds strongly with one of the lattice O, forming a split-interstitial configuration with S–O bond distance of 1.8 Å. The next nearest neighbors of the S atom are an O at 2.2 Å and three Ti at 2.3–2.4 Å, arranged asymmetrically.

Since none of the bulk defects can be responsible for the high-energy peaks (P3–P5), we consider surface sulfur impurities. The center of the main peak (P4) of 2480 eV is near that identified as surface  $\text{SO}_x$ .<sup>21</sup> Surface  $\text{SO}_x$  species are thus potential candidates. (Moreover, previous measurements have indicated  $\text{SO}_x$  species, with  $x=2, 3, 4$ , on  $\text{TiO}_2$  sample surfaces.<sup>22</sup>) For simplicity, we use an ideal bulk-truncated structure of the (101) surface, which is known to be the most stable surface.<sup>2</sup>  $\text{SO}_x$  species were positioned near the surface and their absorption spectra simulated.

Surface  $\text{SO}_x$  (with  $x=2, 3, 4$ ) species are studied. (SO on the surface was also considered but found to be inconsistent with the data.) Considered arrangements included those with

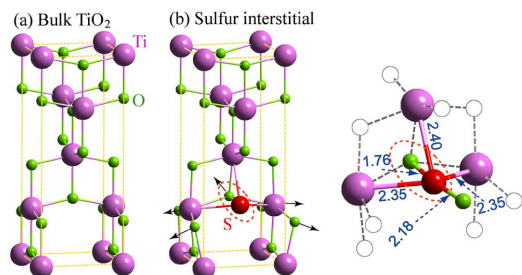


FIG. 3. (Color online) Atomic structures of (a) bulk anatase  $\text{TiO}_2$  and (b) sulfur interstitial ( $\text{S}_i$ ) with a zoom view of the latter on the far right. The large, medium, and small spheres are Ti, S, and O atoms, respectively. The dashed ellipse indicates the split-interstitial S–O pair. The arrows show the relaxation of the neighboring atoms compared to their positions in the bulk. In the zoom, the bond distances from S to its neighbors are given in angstroms and an additional O, from an adjacent unit cell, appears.

an O in the  $\text{SO}_4$  binding to a fivefold coordinated Ti atom (in the next-to-top layer) and those with a twofold coordinated O atom (surface O of  $\text{TiO}_2$ ) included in the  $\text{SO}_4$ . For the former, the displacement of the molecule from the surface was also varied (see Ref. 23). In general, the spectrum of  $\text{SO}_2$  was sensitive to such variations, while the  $\text{SO}_3$  and  $\text{SO}_4$  spectra were not. There was little qualitative surface-orientation dependence, as judged by test calculations using (101) and (001) surfaces.

The spectra of  $\text{SO}_2$  and  $\text{SO}_3$  species have strong absorption peaks located close to 2470 eV (near P1 and P2), and second peaks close to 2480 eV (near P4), whereas the spectrum of  $\text{SO}_4$  species shows only the latter. However, only  $\text{SO}_3$  and  $\text{SO}_4$  spectra show a feature that corresponds well with the position and shape of P5. This makes the latter two species of surface sulfur the most promising candidates. After considering the observed effect of washing the samples (described next), the  $\text{SO}_4$  species emerge as that most likely responsible for P4 and P5.

To test the stability of S in the sample, the (500 °C) sample was washed with distilled water. The measured XANESs before (dashed line) and after (solid line) washing are shown in Fig. 2. The spectra are normalized by matching the heights of corresponding P1. While the position and shape of features appear unchanged, there is a clear reduction of P3–P5 upon washing, which suggests that some S absorbers are washed away. These data cannot be easily explained if the  $\text{SO}_3$  species on the surface are primarily responsible for the high-energy peaks. For, if it were, then  $\text{SO}_3$  would contribute significantly to the lower-energy region as well. This would make it difficult to explain the large change in high-energy absorption relative to low-energy absorption that is produced by washing. Furthermore,  $\text{SO}_3$  is not likely to contribute much to the lower-energy region since the latter is much better described by the bulk S interstitial simulation discussed above.

To study the sulfur species that is washed away, we plot the difference between unwashed and washed XANES spectra (Fig. 2, right inset). The spectrum of this difference is dominated by peaks corresponding to P4 and P5 and is in good agreement with the simulated spectrum of the surface  $\text{SO}_4$  species considered (dashed line). Note that, for ease of

comparison, the simulation was shifted (up by about 2 eV) to align its main peak with that of the measurement. This suggests that surface S in  $\text{SO}_4$  form is largely responsible for the washing dependence of the spectra and thus for the high-energy peaks in annealed samples.

In summary, we have studied Ti and S *K*-edge XANESs of sulfur-doped  $\text{TiO}_2$  prepared by oxidative annealing of  $\text{TiS}_2$ . For annealing temperatures of 300 °C or above, the samples are converted to  $\text{TiO}_2$  with no detectable  $\text{TiS}_2$  phase, according both to XRD and Ti-edge XANES measurements. The S-edge XANES spectrum is found to gradually evolve away from that of  $\text{TiS}_2$ , developing new qualitative features, as the annealing temperature is increased from 200 to 500 °C. The XANES spectrum of the high (500 °C) annealing-temperature sample, in conjunction with first principles calculations, indicates that sulfur atoms are mainly on the  $\text{TiO}_2$  surface as  $\text{SO}_4$  and, within the sample, most likely in the form of split interstitials ( $\text{S}_i$ ). The detailed description of surface and bulk incorporation of S in  $\text{TiO}_2$  provided by XANES measurements here will be useful for disentangling various influences on photocatalysis in sulfur-doped  $\text{TiO}_2$ .

This work is partially supported by MTEC (Grant No. MT-B-49-CER-07-195-I) and Commission on Higher Education, Thailand (CHE-RES-RG “Theoretical Physics”).

- <sup>1</sup>M. R. Hoffmann, S. T. Martin, W. Choi, and D. H. Bahnemann, *Chem. Rev.* (Washington, D.C.) **95**, 69 (1995).
- <sup>2</sup>U. Diebold, *Surf. Sci. Rep.* **48**, 53 (2003).
- <sup>3</sup>K. Hashimoto, H. Irie, and A. Fujishima, *Jpn. J. Appl. Phys., Part 1* **44**, 8269 (2005).
- <sup>4</sup>T. Umehayashi, T. Yamaki, H. Itoh, and K. Asao, *Appl. Phys. Lett.* **81**, 454 (2002).
- <sup>5</sup>T. Umbeyashi, T. Yamaki, S. Yamamoto, A. Miyashita, S. Tanaka, T. Sumita, and K. Asai, *J. Appl. Phys.* **93**, 5156 (2003).
- <sup>6</sup>S. U. M. Khan, M. Al-Shahry, M. Al-Shahry, and W. B. Ingler, *Science* **297**, 2243 (2002).
- <sup>7</sup>H. Wang and J. P. Lewis, *J. Phys.: Condens. Matter* **17**, L209 (2005).
- <sup>8</sup>C. Di Valentini, G. Pacchioni, and A. Selloni, *Phys. Rev. B* **70**, 085116 (2004).
- <sup>9</sup>H. Wang and J. P. Lewis, *J. Phys.: Condens. Matter* **18**, 421 (2006).
- <sup>10</sup>R. Asahi, T. Morikawa, T. Ohwaki, A. Aoki, and Y. Taga, *Science* **293**, 269 (2001).
- <sup>11</sup>A. Hattori, M. Yamamoto, H. Tada, and S. Ito, *Chem. Lett.* **8**, 707 (1998).
- <sup>12</sup>E. L. Hebenstreit, W. Hebenstreit, and U. Diebold, *Surf. Sci.* **461**, 87 (2000).
- <sup>13</sup>J. A. Rodriguez, S. Chaturvedi, M. Kuhn, and J. Hrbek, *J. Phys. Chem. B* **102**, 5511 (1998).
- <sup>14</sup>J. A. Rodriguez and J. Hrbek, *Acc. Chem. Res.* **32**, 719 (1999).
- <sup>15</sup>F. Farges, G. E. Brown, Jr., and J. J. Rehr, *Phys. Rev. B* **56**, 1809 (1997).
- <sup>16</sup>Z. Y. Wu, F. Lemoigno, P. Gressier, G. Ouvrard, P. Moreau, J. Rouxel, and C. R. Natoli, *Phys. Rev. B* **54**, R1109 (1996).
- <sup>17</sup>D. Onkaw (unpublished).
- <sup>18</sup>A. L. Ankudinov, B. Ravel, J. J. Rehr, and S. D. Conradson, *Phys. Rev. B* **58**, 7565 (1998).
- <sup>19</sup>G. Kresse and J. Furthmüller, *Comput. Mater. Sci.* **6**, 15 (1996).
- <sup>20</sup>S. Na-Phattalung, M. F. Smith, K. Kim, M.-H. Du, S.-H. Wei, S. B. Zhang, and S. Limpitjumnong, *Phys. Rev. B* **73**, 125205 (2006).
- <sup>21</sup>J. A. Rodriguez, T. Jirsak, S. Chaturvedi, and M. Kuhn, *Surf. Sci.* **442**, 400 (1999).
- <sup>22</sup>D. I. Sayago, P. Serrano, O. Böhme, A. Goldoni, G. Paolucci, E. Román, and J. A. Martín-Gago, *Phys. Rev. B* **64**, 205402 (2001).
- <sup>23</sup>Note that first principles surface structural relaxations were not performed, so the actual local structure surrounding surface S defects was not determined. Rather, we considered several simplified surface defect configurations and simulated their XANES spectra to determine which, if any, is consistent with the high-energy features of the data.

## B.2 Manuscript Published in Current Applied Physics

Current Applied Physics 11 (2011) S279–S284



Contents lists available at ScienceDirect

Current Applied Physics

journal homepage: [www.elsevier.com/locate/cap](http://www.elsevier.com/locate/cap)



### Local structures of cobalt in Co-doped TiO<sub>2</sub> by synchrotron x-ray absorption near edge structures

J. T-Thienprasert<sup>a,b</sup>, S. Klaitong<sup>c</sup>, A. Niltharach<sup>c</sup>, A. Worayingyong<sup>c</sup>, S. Na-Phattalung<sup>d</sup>, S. Limpijumnong<sup>d,\*</sup>

<sup>a</sup> Department of Physics, Kasetsart University, Bangkok 10900, Thailand

<sup>b</sup> Thailand Center of Excellence in Physics (ThEP Center), Commission on Higher Education, Bangkok 10400, Thailand

<sup>c</sup> Department of Chemistry, Kasetsart University, Bangkok 10900, Thailand

<sup>d</sup> School of Physics, Suranaree University of Technology and Synchrotron Light Research Institute, Nakhon Ratchasima 30000, Thailand

#### ARTICLE INFO

##### Article history:

Received 26 June 2010

Received in revised form

24 October 2010

Accepted 28 December 2010

Available online 6 January 2011

##### Keywords:

X-ray absorption spectroscopy

Titanium dioxide

Cobalt oxide

First principles calculations

#### ABSTRACT

The local structures of cobalt in Co-doped TiO<sub>2</sub> were studied by combining *K*-edge x-ray absorption near edge structures (XANES) measurements with first-principles calculations. The Co/TiO<sub>2</sub> samples were prepared by (1) sol-gel and (2) co-precipitation methods. To identify the local structure around Co, the measured spectra are compared against the spectra measured from Co<sub>3</sub>O<sub>4</sub>, CoO and Co foil standard samples as well as first principles XANES based on several atomic models. For the sample prepared by the co-precipitation method, Co atoms clearly form a separated Co<sub>3</sub>O<sub>4</sub> phase because the XANES spectrum is almost identical to that of Co<sub>3</sub>O<sub>4</sub>. For the sample prepared by the sol-gel method, the spectrum does not look like a spectrum of any of the standards. The possible local structures of Co in the sol-gel prepared sample are discussed. Our work illustrated that XANES is a powerful technique that can be used to probe the local structures of minority atoms even if the standard x-ray diffraction techniques failed.

© 2010 Elsevier B.V. All rights reserved.

### 1. Introduction

The Fischer-Tropsch synthesis (FTS) is a process composed of a set of chemical reactions used to produce liquid hydrocarbons from carbon monoxide (CO) and hydrogen. Because CO is toxic and the obtained hydrocarbon can be used as petroleum substitute, the process gained world wide attentions. The most effective catalysts for FTS are cobalt (Co), iron (Fe), and ruthenium (Ru) [1,2]. It is known that Co is the most active catalyst for FTS based on natural gas, has high selectivity to linear long-chain hydrocarbons, and has low activity for the water-gas shift (WGS) reaction [1,3]. The most common catalyst supports for FTS are alumina (Al<sub>2</sub>O<sub>3</sub>), silica (SiO<sub>2</sub>), and titanium dioxide (TiO<sub>2</sub>) [3–6]. In this work, TiO<sub>2</sub> will be used as a catalyst support because of its ability to increase the reduction [6].

TiO<sub>2</sub> supported Co catalysts were prepared by sol-gel and co-precipitation methods. To characterize the samples, the x-ray diffraction (XRD) and x-ray absorption spectroscopy (XAS) techniques were used. The XRD technique is a powerful technique to identify the crystal structures, especially to gain information on the

polymorph of TiO<sub>2</sub>. XRD is also a standard technique to probe a phase separated structures. In our case here, we can try to look for other phases of Co, such as CoO and Co<sub>3</sub>O<sub>4</sub>. We will show that XRD misses the phase separated cobalt oxides in our case here where they are expected to form small-size clusters. While XRD requires a long-range ordering and is not element specific, the XAS is highly element selective and does not require a long-range ordering to probe the local structure [7]. By choosing the x-ray energy, one can probe only the interested element (in our case, Co) that has excitation energy matching with the x-ray energy. XAS can be divided into two regions: x-ray absorption near-edge spectroscopy (XANES) and extended x-ray absorption spectroscopy (EXAFS). Both XANES and EXAFS have been widely used to identify the local structures of the interested atoms. The spectra contain information of the local structure around the interested atom as well as the oxidation state of the atom. However, in many cases, especially for the XANES interpretations, it is quite complicated to extract the structural information without some prior knowledge of similar systems. For such cases, first principles calculations can be used in conjunction with the measurements to interpret the results. For the EXAFS analysis, some information on the bond distances and coordination number can be obtained readily by simple Fourier transform of the spectra and simple scattering models.

\* Corresponding author.

E-mail address: [sukit@sut.ac.th](mailto:sukit@sut.ac.th) (S. Limpijumnong).

In this work, a combination of Co *K*-edge synchrotron XANES measurements and first-principles calculations was used for identifying the local structures of Co atoms in Co-doped TiO<sub>2</sub> samples grown by two different methods: the sol-gel method and the co-precipitation method. We have successfully utilized the combined XANES measurements and first-principles calculations to identify the local structures of other systems [8–11].

## 2. Experiment

### 2.1. Sample preparation

In the sol-gel method, titanium isopropoxide (Ti[OCH(CH<sub>3</sub>)<sub>2</sub>]<sub>4</sub>, Fluka, analytical grade) in an amount of 0.01 mol was slowly dropwise into 0.33 mol isopropanol (C<sub>3</sub>H<sub>8</sub>O, QR&C, analytical grade) with stirring. Ethylene glycol (HOCH<sub>2</sub>CH<sub>2</sub>OH, Fluka, 98%) in an amount of 0.07 mol was added into the solution. After that, 0.04 mol deionized water was added and stirred until the solution was homogeneous. The sol was allowed to rest in an oven at 348 K until the gel was formed. Then, the gel was dried at 383 K for 24 h. The dried sample was further calcined at 823 K for 4 h with a ramp rate of 1.7 K/min under the flowing of N<sub>2</sub>/O<sub>2</sub> (70/30) gas with the flow rate of 100 cm<sup>3</sup>/min. The obtained sample will be referred to as TiO<sub>2</sub>-SG. For a Co-doped TiO<sub>2</sub>-SG catalyst (Co/TiO<sub>2</sub>-SG), the sample was prepared using the method described above with the addition of cobalt nitrate hexahydrate (Co(NH<sub>3</sub>)<sub>2</sub>·6H<sub>2</sub>O, Univar, analytical grade). The Co precursor in an amount of 10% w/w (dissolved in 0.04 mol deionized water) was added into the sol solution.

For the co-precipitation method, the sample was prepared from suspension of 0.038 mol titanium oxide (Aldrich, anatase ≥99%) in 10% w/w cobalt nitrate solution (cobalt nitrate hexahydrate in 20 cm<sup>3</sup> deionized water). Co(OH)<sub>2</sub> was precipitated from NH<sub>3</sub> solution at pH 7.5 ± 0.2 at 368 K under vigorous stirring. After that, the suspension was heated for a short period, and filtered off at the boiling temperature. The filtered solid was washed and dried at 383 K in an oven. The prepared catalyst was calcined at 823 K for 2 h with a ramp rate of 2.0 K/min under the flowing of argon gas with the flow rate of 40 cm<sup>3</sup>/min. The obtained sample will be referred to as Co/TiO<sub>2</sub>-CP.

### 2.2. Sample characterization

#### 2.2.1. X-ray diffraction (XRD)

X-ray diffraction is a powerful technique to determine the crystalline phases in the samples. For our study, we focus our attentions to the anatase or rutile phases of TiO<sub>2</sub>. We also tried to look for other phases of Co, such as CoO and Co<sub>3</sub>O<sub>4</sub>. The later is to see if Co forms clear phase separated structures. The measurement was conducted using a Philips X'Pert diffractometer with Cu *K*<sub>α</sub> (λ = 1.54 Å) source. The spectra were scanned with the step size of 0.01° in the scanning range 2θ = 10°–80°.

#### 2.2.2. X-ray absorption spectroscopy (XAS)

To study the local structures around the Co atom in the sample, we used the XAS technique with the Co *K*-edge photon energy. XAS measurements were performed in the transmission mode at the XAS beam line (BL-8) of Synchrotron Light Research Institute, Thailand. The electron energy was 1.2 GeV with the beam current of 150–80 mA. A double crystal monochromator Ge(220) was used to scan the photon energy. For the Co *K*-edge XANES measurements, the scanning step was set at 0.2 eV in the photon energy range of 7669–7819 eV. To process the XANES spectra, we performed a standard routine, i.e., a background subtraction and normalization of the raw data.

## 3. Computational method

### 3.1. Crystal structure and formation energy

To gain insight of the stability of Co atom at various sites in TiO<sub>2</sub> crystal, the first principles formation energy calculations were performed. The calculations were based on density functional theory within the local density approximations (LDA). For the electron–ion interactions, we used projector augmented wave potentials [12], as implemented in the VASP code [13,14], with an energy cutoff of 500 eV for the plane-wave basis set. The calculated lattice parameters of anatase TiO<sub>2</sub> are *a* = 3.767 Å, *c/a* = 2.513 Å, and *u* = 0.208 which are in good agreement with the experimental values of *a* = 3.785 Å, *c/a* = 2.513 Å, and *u* = 0.208 [15].

To study defects such as Co substitute for Ti (Co<sub>Ti</sub>) or interstitial Co (Co<sub>i</sub>), a supercell approach was used [16]. We used a 108-atom supercell, which is a 3 × 3 × 2 repetition of the conventional 8-atom TiO<sub>2</sub> unit cell. The Monkhorst-Pack scheme [17] with a sampling mesh of 2 × 2 × 2 special *k*-points is used for the *k*-space integrations. All atoms in the supercell were allowed to relax until the Hellmann-Feynman forces [18] on all atoms become less than 10<sup>−3</sup> eV/Å. The defect formation energy is defined as

$$\Delta H_f = E_{\text{tot}}(D, q) - E_{\text{tot}}(0) + \sum \Delta n_x \mu_x + q(E_f + E_V), \quad (1)$$

where  $E_{\text{tot}}(D, q)$  is the calculated total energy of a supercell with defect *D* in charge state *q*,  $E_{\text{tot}}(0)$  is the calculated total energy of a supercell without any defect.  $\Delta n_x$  is the number of atoms from species *X*, where *X* can be Ti, O, or Co, being added (removed) to (from) a supercell, from (to) its respective reservoir with chemical potential  $\mu_x$ , to form the defect cell.  $E_f$  is energy of the electron reservoir with which the electrons are exchanged. The energy level also referred to as Fermi level.  $E_V$  is the valence band maximum (VBM) which we used the average value overall sampling *k*-points following the scheme of Zhang [19,20]. To align the energy levels between the supercell containing a defect with that of the bulk, we aligned the core potential of atoms far away from the defect in the supercell containing a defect with that of the corresponding atoms in the defect-free supercell. The upper limits for  $\mu_{\text{Ti}}$  and  $\mu_{\text{O}}$  are the energies per atom of metallic Ti and gaseous O<sub>2</sub>, which are offset to zero in the present study. To grow the TiO<sub>2</sub> crystal in equilibrium, it is required that  $\mu_{\text{TiO}_2} = \mu_{\text{Ti}} + 2\mu_{\text{O}}$ , where  $\mu_{\text{TiO}_2}$  is the formation energy per molecular formula of anatase TiO<sub>2</sub> (calculated value:  $\mu_{\text{TiO}_2} = -9.98$ ) [20]. For the chemical potential of cobalt ( $\mu_{\text{Co}}$ ) we used the energy per Co atom of metallic Co and Co<sub>2</sub>O<sub>3</sub> for Ti-rich and O-rich growth condition, respectively.

### 3.2. X-ray absorption spectroscopy

In order to calculate the Co *K*-edge XAS spectra in the XANES region of Co-doped TiO<sub>2</sub> from the model structures, FEFF8.2 codes were used [21,22]. The codes utilize the full multiple scattering approach based on *ab initio* overlapping muffin-tin potentials. These potentials were obtained using self-consistent calculations with Hedin-Lundqvist exchange-correlation function [23]. The self-consistent calculations were performed in the sphere with a radius of 5.5 Å (containing approximately 70 atoms) around the selected absorber (in this case, Co) atom. The full multiple scattering calculations, which include all possible paths within a larger cluster radius of 8.4 Å (containing approximately 240 atoms), were used. The core-hole correction was also applied. The results presented in this work are presented *without* shifting any of the simulated spectra to align with those of the experiment.

#### 4. Results and discussions

The XRD patterns of TiO<sub>2</sub>-SG, Co/TiO<sub>2</sub>-SG, Co/TiO<sub>2</sub>-CP and pure-anatase TiO<sub>2</sub> were shown in Fig. 1. Comparing with the XRD patterns of pure-anatase TiO<sub>2</sub>, we found that the crystal structure of Co/TiO<sub>2</sub>-SG sample (grown by sol-gel method) is mainly anatase with a small amount of rutile. However, the Co/TiO<sub>2</sub>-CP sample (grown by co-precipitation method) exhibits only the anatase phase. In addition, the XRD patterns of Co/TiO<sub>2</sub>-SG and Co/TiO<sub>2</sub>-CP did not show the peaks associated with metallic Co, CoO or Co<sub>3</sub>O<sub>4</sub>. This indicates that XRD does not detect separated cobalt oxide phases. Note that, for the Co/TiO<sub>2</sub>-SG sample, there is an unidentified peak at  $2\theta \approx 33^\circ$  which is about one degree below the main peak of CoO at  $2\theta \approx 34.1^\circ$ . Although, it is tempting<sup>1</sup> to associate this peak to CoO, the high angle peaks are missing from the XRD pattern. It is possible that the unidentified peak might come from highly defective or small crystal of CoO such that only the main peak is observed (at shifted angle) and higher angle peaks are suppressed. From the XRD results, it is clear that the preparation methods have the effect on the phase of resulting TiO<sub>2</sub>. However, the XRD results cannot be used to resolve the local structures of Co atoms in the samples. This is because the technique is sensitive to a long-range ordering and is not elemental selective. To identify the local structures of Co atoms in these samples, a combination of XAS measurements and first-principles calculations was used.

Using first-principles calculations, we calculated the formation energies of various Co configurations in TiO<sub>2</sub>. In addition, we also calculated the formation energies of various native defects in TiO<sub>2</sub>. The formation energy indicates how easy to create each defect (we use the term “defect” to refer to both native TiO<sub>2</sub> defects and Co impurity in TiO<sub>2</sub>). The defects with low formation energy are more likely form during growth. As defined in Eq. (1), if one or more host atoms (Ti or O) have to be exchanged with the reservoir to create the defect from a defect free cell, the formation energy of the defect will depend on the growth conditions (varied between Ti-rich and O-rich). Here we showed both extreme cases, so that to compare with experiment, one can choose the appropriated case (or interpolate between the two cases). Note that because we choose the Co reservoir (Co chemical potential,  $\mu_{\text{Co}}$ ) to be the energy per atom of Co atom in Co metal for Ti-rich case and Co atom in Co<sub>2</sub>O<sub>3</sub> for O-rich case, the formation energies of defects containing a Co atom will also depend on the growth conditions. In addition, for charged defects, the formation energies are also depended on the electron reservoir (known as Fermi energy) which can be varied between the valence band maximum and the conduction band minimum for semiconductors. The calculated defect formation energies as a function of Fermi energy (varied from 0 which is the VBM to 2.53 eV which is the CBM) are shown in Fig. 2. Here, we obtained the calculated bandgap of 2.53 eV by calculating the averaged band edge at the special *k*-points [19,20]. First, we studied some important native defects in TiO<sub>2</sub> and compared with the previous work [20]. As can be seen in Fig. 2, the low energy native defects are titanium interstitial (Ti<sup>4+</sup>), oxygen vacancy (V<sub>O</sub><sup>2+</sup>), and titanium vacancy (V<sub>Ti</sub><sup>4+</sup>). Our calculated results are in good agreement with the previous work [20]. Next, we studied Co defects in TiO<sub>2</sub>. Based on the formation energy, we identified two most probable forms of Co atoms incorporated in TiO<sub>2</sub>: Co substitution for Ti (Co<sub>Ti</sub>) and interstitial Co (Co<sub>i</sub>). The relaxed local structures of these defects are illustrated in Fig. 4. Co<sub>Ti</sub> is amphoteric, i.e. acting as a donor when the sample is p-type and as an acceptor when the sample is n-type,

with calculated transition energies at  $\epsilon(2+/1+) = 0.65$  eV,  $\epsilon(1+/0) = 0.87$  eV, and  $\epsilon(0/1-) = 1.37$  eV. On the other hand, Co<sub>i</sub> is always a donor with the calculated transition energies at  $\epsilon(4+/3+) = 1.11$  eV,  $\epsilon(3+/2+) = 1.69$  eV, and  $\epsilon(2+/1+) = 2.25$  eV. Under Ti-rich growth condition (Fig. 2, left panel), we found that the formation energy of Co<sub>i</sub> is very low and is lower than Co<sub>Ti</sub> at any Fermi energy (within the calculated bandgap of  $\sim 2.53$  eV). This means that Co atom prefers to be an interstitial under Ti-rich growth conditions regardless of the sample's type (p-type/n-type). However, under O-rich growth condition (Fig. 2, right panel), the formation energy of Co<sub>i</sub> is lower than that of Co<sub>Ti</sub> only when the Fermi level of the system is within  $\sim 1$  eV above the VBM, i.e. under p-type conditions. For higher Fermi energy, especially for n-type conditions, the Co<sub>Ti</sub> is easier to form. Therefore, under O-rich growth conditions, the Co atom can be at substitution and/or interstitial sites depending on the Fermi level.

To investigate the actual local structures of Co atoms in Co-doped TiO<sub>2</sub> samples, Co *K*-edge XANES measurements were performed. The measured Co *K*-edge XANES spectra of Co/TiO<sub>2</sub>-SG and Co/TiO<sub>2</sub>-CP as well as Co-metal, CoO, and Co<sub>3</sub>O<sub>4</sub> are shown in the left panel of Fig. 3. In order to test the reliability of our calculations, we used first-principles method to determine the optimized crystal structures of Co-metal, CoO, and Co<sub>3</sub>O<sub>4</sub> and generated the XANES spectra. The optimized local structures of these compounds are illustrated in Fig. 4. For Co<sub>3</sub>O<sub>4</sub> compound, there are two inequivalent Co species denoted as Co1 and Co2 in the ratio of Co1:Co2 = 2:1. The calculated Co *K*-edge XANES spectra of Co-metal, CoO, and Co<sub>3</sub>O<sub>4</sub> are shown in the right panel of Fig. 3. Note that for Co<sub>3</sub>O<sub>4</sub> the simulated spectra shown are the average of the spectra obtained from Co1 and Co2 with the weight ratio of 2:1. When comparing the left panel plots to the right panel plots, we found that, beside an overall shift of about 5 eV, the measured and simulated XANES spectra of Co-metal, CoO, and Co<sub>3</sub>O<sub>4</sub> are all in good agreement. However, the features in the simulated spectra are clearly sharper compared to the measurements. This can be attributed partly to the limited resolution of the measurement that results in the broadening of the spectra and partly to the imperfection of the real samples. For CoO, due to the high symmetry of the rocksalt structure, the ideal spectrum would be very sharp as can be seen from the simulation. However, since CoO is not the most stable phase of cobalt oxide, the crystal quality is quite poor and the measured spectrum appeared much broader (even broader than that of Co<sub>3</sub>O<sub>4</sub>). Because the simulated XANES of these known samples give features that are in agreement with the corresponding real measurements, we gained confidence in the reliability of our calculations. Next, we used the optimized structures of Co<sub>i</sub> and Co<sub>Ti</sub> in TiO<sub>2</sub>, obtained from first principles calculations as explained in the previous section, to simulate the XANES spectra. The optimized local structures of Co<sub>i</sub> and Co<sub>Ti</sub> (in charge states 2+ and 1-, respectively) in anatase TiO<sub>2</sub> are shown in Fig. 4. Note that for n-type TiO<sub>2</sub>, the formation energy calculations indicated that the probable charge states are 2+ and 3+ for Co<sub>i</sub> and 0 or 1- for Co<sub>Ti</sub>. We found that the local structures of Co<sub>i</sub><sup>2+</sup> and Co<sub>Ti</sub><sup>0</sup> are similar to that of Co<sub>i</sub><sup>2+</sup> and Co<sub>Ti</sub><sup>1-</sup>, respectively. Therefore, we showed only the results of Co<sub>i</sub><sup>2+</sup> and Co<sub>Ti</sub><sup>1-</sup>. Because we know that the Co/TiO<sub>2</sub>-SG sample contains both the anatase and rutile phase (Fig. 1), we simulated the XANES spectra of Co<sub>i</sub> and Co<sub>Ti</sub> in both phases of TiO<sub>2</sub>. The simulated XANES of Co<sub>i</sub><sup>2+</sup> and Co<sub>Ti</sub><sup>1-</sup> in both anatase and rutile TiO<sub>2</sub> are shown in Fig. 3.

Let us turn to the measured XANES spectra of Co/TiO<sub>2</sub>-SG and Co/TiO<sub>2</sub>-CP samples in Fig. 3. The spectra from both samples are clearly different. This means that the local structures of Co atoms in these two samples are also different. Upon a close inspection of the Co/TiO<sub>2</sub>-CP spectrum, it is clear that the spectrum is almost identical to that of Co<sub>3</sub>O<sub>4</sub>. To illustrate this, the measured spectrum of Co<sub>3</sub>O<sub>4</sub> (dashed curve) is shown superimposed on top of the Co/

<sup>1</sup> Especially, the later discussion on XAS results will show that there may be Co in CoO form scattered in the Co/TiO<sub>2</sub>-SG sample.

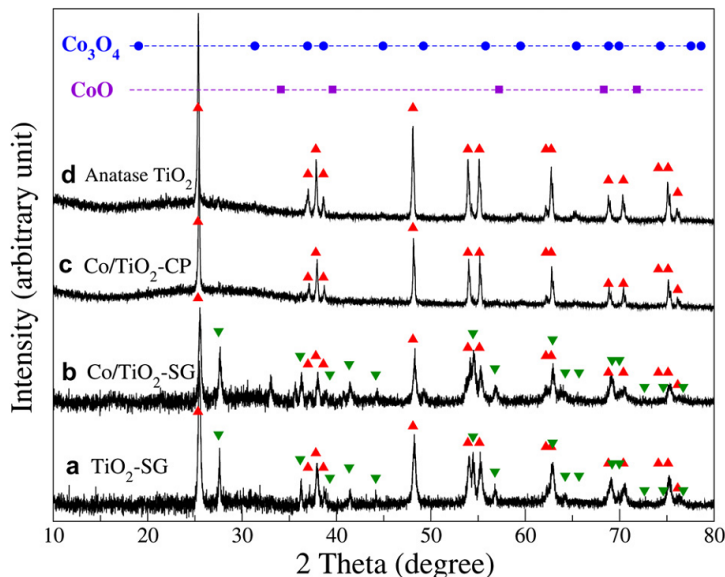


**Fig. 1.** The XRD patterns of (a) TiO<sub>2</sub>-SG, (b) Co/TiO<sub>2</sub>-SG, (c) Co/TiO<sub>2</sub>-CP, and (d) pure-anatase TiO<sub>2</sub> samples. The triangles indicate the peak positions for the anatase (pointing up) and rutile (pointing down) phases. The peak positions of Co<sub>3</sub>O<sub>4</sub> and CoO, if formed, are indicated by circles and squares, respectively.

TiO<sub>2</sub>-CP spectrum. This is strong evidence that the co-precipitate method is not an effective way to incorporate Co into TiO<sub>2</sub> matrix.

Unlike the case of Co/TiO<sub>2</sub>-CP, XANES spectrum of the Co/TiO<sub>2</sub>-SG sample does not look like any of the spectra from the standard samples. The spectrum is very broad and is likely to be the superposition of the spectra of Co in many forms. For instance, the main broad peak (at 7720–7735 eV) can be the superposition of the narrow main peaks of CoO (center at 7725 eV) and Co<sub>3</sub>O<sub>4</sub> (center at 7730 eV) that are Co<sub>Ti</sub> or Co<sub>i</sub> in TiO<sub>2</sub>. In addition, at the higher energy

(7775 eV) there is a hump that is quite similar to the hump in the CoO spectrum except that the amplitude is slightly reduced. However, the direct linear combination fit using the spectra of Co<sub>3</sub>O<sub>4</sub> and CoO as the bases does not yield a convincingly good result. The best fit was obtained by mixing 76% of CoO spectrum with 24% of Co<sub>3</sub>O<sub>4</sub> spectrum and shown as a dashed curve superimposed on top of the measured

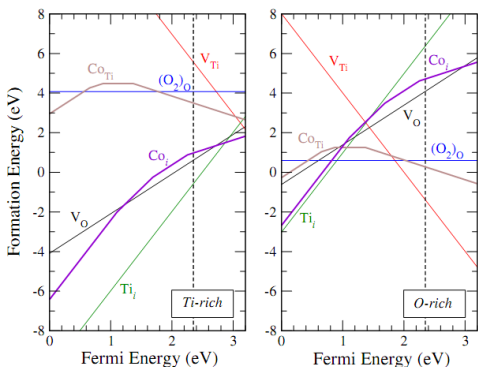


**Fig. 2.** The calculated formation energies of native and extrinsic defects in TiO<sub>2</sub> (anatase) as a function of Fermi level calculated under Ti-rich and O-rich growth conditions, respectively. The slope of each line indicates the charge state of the defect. The Fermi-energy, referenced to the valence band maximum, is extended to the experimental gap of 3.2 eV. The vertical dashed line is the calculated band gap at the special *k*-point.

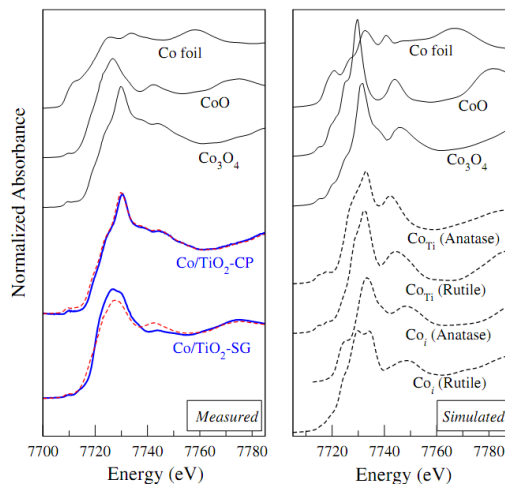


**Fig. 3.** (Left panel) The measured Co *K*-edge XANES spectra of Co foil, CoO, Co<sub>3</sub>O<sub>4</sub>, Co/TiO<sub>2</sub>-CP, and Co/TiO<sub>2</sub>-SG samples. The dash curves are the proposed explanation of the Co structure as described in text. (Right panel) The simulated Co *K*-edge XANES spectra of Co foil (CPP), CoO, Co<sub>3</sub>O<sub>4</sub> as well as Co<sub>Ti</sub> and Co<sub>i</sub> in anatase and rutile TiO<sub>2</sub>.

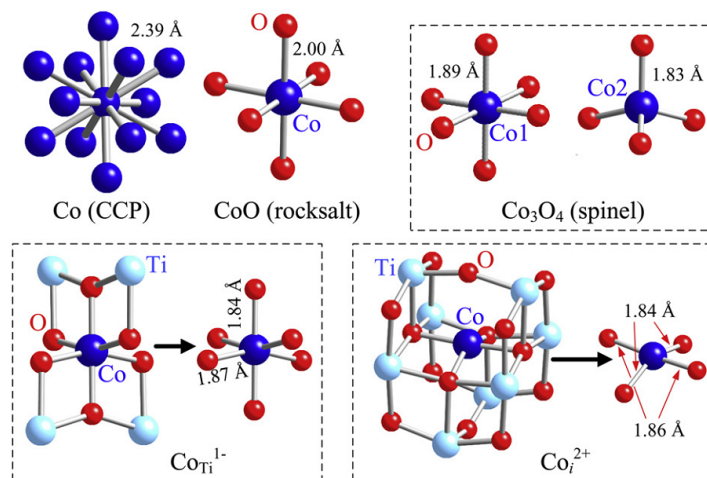


Fig. 4. The local structures of Co atoms in Co foil (metal-CCP), CoO (rocksalt), Co<sub>3</sub>O<sub>4</sub> (spinel), Co<sub>Ti</sub><sup>1-</sup> and Co<sub>Ti</sub><sup>2+</sup> in anatase TiO<sub>2</sub>.

spectrum of Co/TiO<sub>2</sub>-SG in Fig. 3. The large disagreement between the fit and the measured spectrum suggests that there are other forms of Co unaccounted for in the fit. We can give a rough estimation that about 30% of Co atoms are in other forms. One of the candidates for the unaccounted Co form is Co<sub>Ti</sub> which has the local structure similar to that of Co<sub>1</sub> in Co<sub>3</sub>O<sub>4</sub>, as shown in Fig. 4. In addition, the simulation shows that the simulated XANES spectrum of Co<sub>Ti</sub> in both rutile and anatase TiO<sub>2</sub> are quite similar (see right panel of Fig. 3). The features at low energy of Co<sub>Ti</sub> spectra are quite similar to that of Co<sub>3</sub>O<sub>4</sub> except the Co<sub>Ti</sub> spectra are broader. For the high energy region, the Co<sub>Ti</sub> spectra have humps at around the same energy as that of CoO. Although Co<sub>Ti</sub> is a strong candidate for the unaccounted Co, the simulated XANES spectra of Co<sub>i</sub> in both anatase and rutile TiO<sub>2</sub> also show broad first peak that could help to improve the fit and should not be completely ruled out.

One might wonder why the separated Co<sub>3</sub>O<sub>4</sub> phase in the Co/TiO<sub>2</sub>-CP sample and CoO (as well as Co<sub>3</sub>O<sub>4</sub>) in Co/TiO<sub>2</sub>-SG sample were not observed by the standard XRD measurement (Fig. 1). First, there is only ~10 at% of Co in the sample; making the XRD characteristics associated with Co<sub>3</sub>O<sub>4</sub> overshadowed by those of TiO<sub>2</sub> matrix. Second, the phase separated Co<sub>3</sub>O<sub>4</sub> are likely to form in small (or even in nanoscale) clusters that are too small to have sufficient long range ordering for XRD measurement. Our results showed that one should not rely too much on the standard XRD technique to pick up the phase separation of the minority elements, especially when they are expected to form in small cluster forms. XAS is a much more powerful technique to probe in such cases.

## 5. Conclusion

Using a combination of cobalt *K*-edge x-ray absorption near edge structures (XANES) and first-principles calculations, the local structures of Co atoms in Co-doped TiO<sub>2</sub> grown by sol-gel and coprecipitation methods were studied. We found that, while a conventional x-ray diffraction (XRD) technique failed to detect phase separated cobalt oxides in Co/TiO<sub>2</sub> samples, the XANES can clearly probe them. For the Co/TiO<sub>2</sub> sample prepared by the coprecipitate method, XANES signature clearly shows that most (if not all) of Co atoms form phase-separated Co<sub>3</sub>O<sub>4</sub>. For the sample

prepared by the sol-gel method, XANES signature indicates that as much as 70 at% of Co atoms might form cobalt oxide (mixed between CoO and Co<sub>3</sub>O<sub>4</sub>) and there are other forms of Co atoms. First principles calculations show that, in TiO<sub>2</sub>, Co atoms can substitute for Ti atoms (Co<sub>Ti</sub>) or exist as interstitial atoms (Co<sub>i</sub>) with reasonably low formation energies. The simulated XANES of Co<sub>Ti</sub> and Co<sub>i</sub> contain features that make them the likely candidates for unaccounted Co in the sample prepared by the sol-gel method. Our work showed that XRD cannot be reliably used to probe phase separation of minority elements, especially when the separated phase is expected to be in the form of small clusters with short range ordering. X-ray absorption spectroscopy is a powerful technique for such cases.

## Acknowledgment

This work is supported by Thailand Research Fund (Grant No.RTA5280009) and NANOTEC (NN-B-22-D12-20-51-09). One of the authors (SK) acknowledges the scholarship from Synchrotron Light Research Institute.

## References

- [1] H. Schulz, Applied Catalysis A: General 186 (1999) 3.
- [2] M.D. Shroff, D.S. Kalakkad, K.E. Coulter, S.D. Kohler, M.S. Harrington, N.B. Jackson, A.G. Sault, A.K. Datye, Journal of Catalysis 156 (1995) 185.
- [3] B. Jongsomjit, T. Wongsalee, P. Praserttham, Catalysis Communications 6 (Nov 2005) 705.
- [4] G. Jacobs, Y.Y. Ji, B.H. Davis, D. Cronauer, A.J. Kropf, C.L. Marshall, Applied Catalysis A-General 333 (Dec 15 2007) 177.
- [5] B. Jongsomjit, J. Panpranot, J.G. Goodwin, Journal of Catalysis 215 (Apr 1 2003) 66.
- [6] S. Storsaeter, B. Totdal, J.C. Walmsley, B.S. Tanem, A. Holmen, Journal of Catalysis 236 (Nov 15 2005) 139.
- [7] M.F. Smith, W. Klysubun, S. Kityakarn, A. Worayingyong, S.B. Zhang, S.H. Wei, D. Onkaw, P. Songsiriritthigul, S. Rujirawat, S. Limpjumnong, Journal of Applied Physics 105 (2009) 024308.
- [8] S. Limpjumnong, S. Rujirawat, A. Boonchun, M.F. Smith, B. Cherdhirunkorn, Applied Physics Letters 90 (2007) 103113.
- [9] S. Limpjumnong, M.F. Smith, S.B. Zhang, Applied Physics Letters 89 (2006) 222113.
- [10] J. T-Thienprasert, J. Nukeaw, A. Sungthong, S. Porntheeraphat, S. Singkarat, D. Onkaw, S. Rujirawat, S. Limpjumnong, Applied Physics Letters 93 (2008) 051903.
- [11] J. T-Thienprasert, S. Rujirawat, J. Nukeaw, S. Limpjumnong, Computational Materials Science 49 (2010) S37.

- [12] G. Kresse, D. Joubert, *Physical Review B* 59 (1999) 1758.
- [13] G. Kresse, J. Furthmüller, *Computational Materials Science* 6 (1996) 15.
- [14] G. Kresse, J. Hafner, *Journal of Physics Condensed Matter* 6 (1994) 8245.
- [15] C.J. Howard, T.M. Sabine, F. Dickson, *Acta Crystallographica Section B* 47 (1991) 462.
- [16] C.G. Van de Walle, J. Neugebauer, *Journal of Applied Physics* 95 (2004) 3851.
- [17] H.J. Monkhorst, J.D. Pack, *Physical Review B* 13 (1976) 5188.
- [18] R.P. Feynman, *Physical Review* 56 (1939) 340.
- [19] S.B. Zhang, *Journal of Physics: Condensed Matter* 14 (2002) R881.
- [20] S. Na-Phattalung, M.F. Smith, K. Kim, M.-H. Du, S.-H. Wei, S.B. Zhang, S. Limpijumnong, *Physical Review B* 73 (2006) 125205.
- [21] A.L. Ankudinov, C.E. Bouldin, J.J. Rehr, J. Sims, H. Hung, *Physical Review B* 65 (2002) 104107.
- [22] A.L. Ankudinov, B. Ravel, J.J. Rehr, S.D. Conradson, *Physical Review B* 58 (1998) 7565.
- [23] L. Hedin, S. Lundqvist, *Solid State Physics* 23 (1969) 1.



# CURRICULUM VITAE

**NAME** Miss Sutassana Na Phattalung

**DATE OF BIRTH** September 12, 1981

**PLACE OF BIRTH** Mukdahan, Thailand

**E-MAIL** sutassana@gmail.com

## EDUCATION

Master of Science (2003 - 2006)

School of Physics, Institute of Science, Suranaree University of Technology,  
Nakhon Ratchasima, Thailand

Supervisors: Prof. Dr. Sukit Limpijumnong

Bachelor of Science (1999 - 2003)

Department of Physics, Faculty of Science, Khon Kaen University, Thailand